UNIVERSITÀ
DEGLI STUDI
DI PADOVA

UNIVERSITA' DEGLI STUDI DI PADOVA

Dipartimento di Ingegneria Industriale DII

Corso di Laurea Magistrale in Ingegneria Meccanica

Numerical approach for simulating the dynamics of partial cavitation by Large Eddy Simulation turbulence model

Relatore: Prof.ssa Giovanna Cavazzini

Correlatore: Prof. Jens Honoré Walther

Laureando: Francesco Nascimben 1167080

Anno Accademico 2019/2020

Abstract

Nowadays, cavitation is still affecting the performance of several engineering devices such propellers, injectors, hydraulic pumps and turbines. However, the numerical prediction of the cavitation onset and development in fluids still remains a big challenge and there is a clear need of defining highly accurate approaches to use during the design phase.

This Master Thesis will focus on the unsteady cavitation in internal ducts, whose complexity is increased by the need of properly simulating the interaction of the cavity interface and flow with fluid-dynamic phenomena, such the so-called "re-entrant jet mechanism" (caused by adverse pressure gradients) and bubbly shock mechanism, induced by the collapse of previously shedded vapour cavities.

In literature, both homogeneous mixture models and multi-phase models were tested with the aim of proposing solid methods to simulate cavitation and it is a matter of fact that the choice of the turbulence model is one of the most critical point in simulating this phenomenon. Several studies were able to capture the two mechanisms responsible for unsteady cavitation phenomena, but not the corresponding shedding processes in terms of frequencies and characteristic length.

In this work, a two-phase Schnerr-Sauer cavitation model adopting the Large Eddy Simulation (LES) turbulence model was developed by means of the commercial CFD software *STAR CCM+* and validated by comparison with experimental data available in literature.

The model was tested on the full 3D Venturi geometry in condition of re-entrant jet cavitating regime. Water and vapor were treated both as incompressible fluids, while the VOF (Volume of Fluid) model was used to solve the multi-phase mixture behaviour. Particular attention was paid to the initialization strategy and to the velocity and turbulence fields to fix at the inlet boundary conditions.

Concerning the LES turbulence model, both WALE (Wall Adaptive Local Eddy Viscosity) and Dynamic Smagorinsky's Sub-Grid Scaling models were tested and both models were able to simulate the re-entrant jet phenomenon. After an in-depth analysis of the simulations results, both models were also found to be able to detect shedding frequencies of the order of the experimental ones. Additional investigation should be conducted further refining the mesh.

Abstract (Italian)

Al giorno d’oggi, il fenomeno della cavitazione coinvolge ancora diverse applicazioni di interesse ingegneristico, come ad esempio le eliche nautiche, gli iniettori dei motori a combustione interna, le pompe e le turbine idrauliche. Nonostante tale fenomeno fluidodinamico sia ormai noto da più di un secolo, gli studiosi sono tuttora ancora molto impegnati nella ricerca di metodi ed approcci numerici efficaci per prevedere con accuratezza sempre maggiore l’insorgenza e lo sviluppo di bolle di cavitazione già durante la fase di progettazione.

La presente Tesi Magistrale si concentra sullo studio del fenomeno della cavitazione all’interno di condotti, la cui complessità è ulteriormente accresciuta dalla necessità di simulare in modo opportuno l’interazione tra le cavità di vapore e alcuni fenomeni fluidodinamici tipici della cavitazione all’interno di condotti: il meccanismo del getto rientrante (*re-entrant jet mechanism*, causato dalla presenza di gradienti di pressione avversi rispetto al flusso principale) e il meccanismo *bubbly shock* (*bubbly shock mechanism*, indotto dal collasso delle cavità di vapore precedentemente createsi e trasportate dal flusso verso valle).

In letteratura, nel tempo, sono stati presentati diversi test numerici condotti utilizzando sia modelli di miscela omogenea che modelli multifase con l’obiettivo di proporre metodi robusti per simulare la cavitazione ed è stato più volte confermato come la scelta del modello di turbolenza eserciti una grandissima influenza sui risultati delle simulazioni. Tale scelta risulta quindi essere uno dei punti più critici nella simulazione di tale fenomeno. Diversi studi sono riusciti a sviluppare e validare modelli numerici capaci di riprodurre entrambi i meccanismi responsabili dell’insorgenza di fenomeni di cavitazione non stazionaria, ma raramente tali metodi sono riusciti a riprodurre il processo periodico di formazione e sviluppo delle cavità di vapore con frequenze e lunghezze caratteristiche in accordo con i dati sperimentali.

Nel presente elaborato, la simulazione del fenomeno di cavitazione parziale all’interno di un condotto convergente-divergente è stata condotta considerando un flusso bi-fase semplicemente costituito da acqua e vapore. Come modello di cavitazione è stato selezionato il modello Schnerr-Sauer, mentre per riprodurre gli effetti della turbolenza si è deciso di applicare l’approccio LES. Tutte le simulazioni sono state condotte utilizzando il software commerciale *STAR CCM+* e i risultati ottenuti sono poi stati validati facendo riferimento ai dati sperimentali disponibili in letteratura.

Come già accennato in precedenza, il modello di cavitazione proposto è stato testato numericamente simulando, in condizioni di cavitazione e in presenza del fenomeno del getto rientrante, il flusso 3-D interno ad un condotto assialsimmetrico convergente-divergente. Per entrambi i fluidi (acqua e vapore) è stata fatta l'ipotesi di fluido incomprimibile, mentre il metodo del Volume di Fluido (*Volume of Fluid*, *VOF*) è stato preso in considerazione per chiudere il problema e risolvere quindi le equazioni che governano matematicamente il comportamento della miscela multifase. Particolare attenzione è stata riservata all'implementazione della procedura di inizializzazione e delle condizioni al contorno in ingresso al Venturi. In particolare, per risolvere quest'ultimo problema, i profili medi di velocità e di alcune proprietà della turbolenza sono stati ottenuti e applicati come condizioni di ingresso al condotto convergente-divergente, riproducendo (attraverso l'utilizzo del metodo SEM) un campo di moto realisticamente turbolento.

Per quanto riguarda il modello di turbolenza LES, sono stati testati i modelli WALE (Wall Adaptive Local Eddy Viscosity) e Dynamic Smagorinsky, ottenendo in entrambi i casi buoni risultati. Ambedue i modelli, infatti, sono stati in grado di riprodurre efficacemente la fisica del problema, replicando il fenomeno del getto rientrante. Dopo un'approfondita analisi dei risultati ottenuti, tutti e due i modelli testati si sono rivelati attendibili, riuscendo ad individuare valori di frequenza compatibili con i dati sperimentali per il fenomeno di cavitazione parziale considerato. Per validare definitivamente l'approccio, ulteriori indagini dovrebbero essere condotte raffinando la mesh.

Preface

This Master Thesis was prepared at the department of Mechanical Engineering at the Padua University (UniPD), from the September 2019 to October 2020. The work fulfils the requirements for acquiring a Master degree in Mechanical Engineering at the Università degli Studi di Padova. The work has been carried out under the supervision of Professors Jens Honorè Walther (DTU) and Giovanna Cavazzini (UniPD).

Padova, October 15, 2020

Francesco Nascimben

Acknowledgements

I would like to express my gratitude to my supervisors Professors Jens Honoré Walther and Giovanna Cavazzini for their support and guidance: thank you for having shared with me your valuable knowledge and time.

I also want to thank all the friends I met attending the University: Giuseppe, Giacomo, Federico, Enrico, Denis. Of course, Mechanical Engineering is not the simplest course to attend, but you helped me in facing it. It was a pleasure to share this experience with all of you.

I am also grateful to my dearest friends Antonio and Gabriele: you have always been by my side in good and bad moments. I hope you’ll be able to realize all your dreams!

My gratitude goes also to all the people I encountered on my way attending the Scout’s activities: you taught me that doing good to other people for free is one of the most beautiful things in the world, but it is also necessary to be always prepared to do your best in all situations.

Last, but definitely not least, I am greatly indebted to my family: my father Leonildo, my mother Bertilla and my sister Alice. You have always provided me all your support, encouragements and love. I dedicate this goal to all of you.

Contents

List of Tables

List of Figures

Nomenclature

Abbreviations

Acronym	**Meaning**
1-D	One-dimensional problem
3-D	Three-dimensional problem
ALF	Anisotropic Linear Forcing method
BCs	Boundary Conditions
CD	Central Differencing interpolation
CFD	Computational Fluid Dynamics
CM	Control Mass
CV	Control Volume
DNS	Direct Numerical Simulations
FFT	Fast Fourier Transform
FOU	First-order upwind interpolation
HEM	Homogeneous Equilibrium Model
ILES	Implicit Large Eddy Simulations
LES	Large Eddy Simulations
NVD	Normalized-Variable Diagram
PISO	Pressure-Implicit with Splitting of Operators
PMMA	Poly-Methyl-Methacrylate
RANS	Reynolds Averaged Navier-Stokes equations
SEM	Synthetic Eddy Method
SGS	Sub-Grid Scale model

SIMPLE	Semi-Implicit Method for Pressure Linked Equations
SOU	Second-order upwind interpolation
UBF	Upwind blending factor
URF	Under-Relaxation factor
VOF	Volume of Fluid model
WALE	Wall-Adaptive Local-Eddy Viscosity model

Greek Symbols

Symbol	**Description**	**Dimensions**	**Units**
α	Volume fraction	--	--
δ	Kronecker delta	--	--
Δp	Pressure difference	$M\ L^{-1}\ T^{-2}$	Pa
Δt	Time-step	T	s
Δx	Grid size	L	m
μ	Dynamic viscosity	$M\ L^{-1}\ T^{-1}$	Pa s
μ_{SGS}	Sub-grid scale dynamic viscosity	$M\ L^{-1}\ T^{-1}$	Pa s
ν	Cinematic viscosity	$L^{2}\ T^{-1}$	$m^{2}\ s^{-1}$
ν^{r}	Residual cinematic viscosity	$L^{2}\ T^{-1}$	$m^{2}\ s^{-1}$
ρ	Density	$M\ L^{-3}$	$kg\ m^{-3}$
ψ	Generic intensive property	--	--
Δ	Filtering size	L	m
τ	Turbulent time scale	T	s
τ_{ij}	Deviatoric stress tensor	$M\ L^{-1}\ T^{-2}$	Pa
τ_{0}	Wall shear stress	$M\ L^{-1}\ T^{-2}$	Pa

κ	Von Karman constant	--	--
ε	Turbulent energy flux	L^2 T^{-3}	m^2 s^{-3}
ϕ	Convective flux of a generic quantity	--	--
ξ	Normalized-Variable Diagram value	--	--
γ	Surface tension	M T^{-2}	N m^{-1}
λ	Taylor micro-scale	L	m
η	Kolmogorov length scale	L	m
ϑ_{conv}	Venturi convergence angle	--	°
ϑ_{div}	Venturi divergence angle	--	°

Roman Symbols

Symbol	**Description**	**Dimensions**	**Units**
$\boldsymbol{b}$	Body forces	L T^{-2}	N kg^{-1}
$\boldsymbol{n}$	Normal vector	--	--
$\boldsymbol{u}$	Velocity vector	L T^{-1}	m s^{-1}
$\boldsymbol{x}$	Position vector	L	m
A	Area	L^2	m^2
$\dot{m}$	Mass flow	M T^{-1}	kg s^{-1}
d	Diameter	L	m
d_0	Seed diameter	L	m
f	frequency	T^{-1}	Hz
g	Gravity	L^1 T^{-2}	m s^{-2}
k	Turbulent kinetic energy	L^2 T^{-2}	m^2 s^{-2}
I	Turbulence intensity	--	--

l_t	Turbulent length scale	L	m
L	Characteristic length scale	L	m
L_{cav}	Cavity length at time of detachment	L	m
n_0	Seed density	L^{-3}	m^{-3}
N	Number of seeds	--	--
p	Pressure	$M\ L^{-1}\ T^{-2}$	Pa
p_{sat}	Saturation pressure	$M\ L^{-1}\ T^{-2}$	Pa
p_v	Vapor pressure	$M\ L^{-1}\ T^{-2}$	Pa
R	Bubble radius	L	m
S	Surface	L^2	m^2
S_{α_i}	Source term of the i-th phase	--	--
T	Period	T	s
t	Time	T	s
V	Volume	L^3	m^3
u, v, w	Velocity components	$L\ T^{-1}$	$m\ s^{-1}$
x, y, z	Position coordinates	L	m
y^+	Non-dimensional wall distance	--	--

Other Symbols

Symbol	**Description**	**Dimensions**	**Units**
$\boldsymbol{\mathcal{T}}$	Stress tensor	$M\ L^{-1}\ T^{-2}$	Pa
$\mathbb{I}$	Identity tensor	--	--
$\boldsymbol{\mathcal{E}}$	Viscous stress tensor	$M\ L^{-1}\ T^{-2}$	Pa
ℓ	Eddy size	L	m

Non-dimensional numbers

Symbol	Description	Definition
σ	Cavitation number	$\sigma = \frac{p-p_v}{\frac{1}{2}\rho u^2}$
C	Courant number	$C = u\frac{\Delta t}{\Delta x}$
Re	Reynolds number	$Re = \frac{\rho u L}{\mu}$
St	Strouhal number	$St = \frac{fL}{u}$
K	Pressure loss coefficient	$K = \frac{\Delta p}{\frac{1}{2}\rho u^2}$

Subscripts

Symbol	Meaning
∞	Infinitely far
B	Bubble
L	Liquid
V	Vapor

Superscripts

Symbol	Meaning
$\sim$	Filtered quantity
$-$	Averaged quantity
$*$	Guessed quantity
$'$	Residual component
$\cdot$	Time derivative
$\cdot\cdot$	Second Time derivative

Chapter 1

Introduction

In fluid dynamics, when the pressure of a liquid falls below the vapor tension of the fluid, the formation of small cavities filled with vapor can be observed.

This phenomenon, called *cavitation*, is quite common in fluid machinery, where working fluids experience large increase in velocity (and consequently large pressure drops) that can lead pressure to fall below the vapor tension of the liquid.

This particular cavitation phenomenon, known among scientists and engineers as *hydrodynamic cavitation*, occurs in devices like nozzles, fuel injectors (as you can observe in Figure 1.1), pumps, propellers and hydraulic turbines and must be taken into account during the design of machinery because, if not kept under control, it can lead to surface fatigue, wear, loss in performances, noise and machine damage (see Figure 1.2).

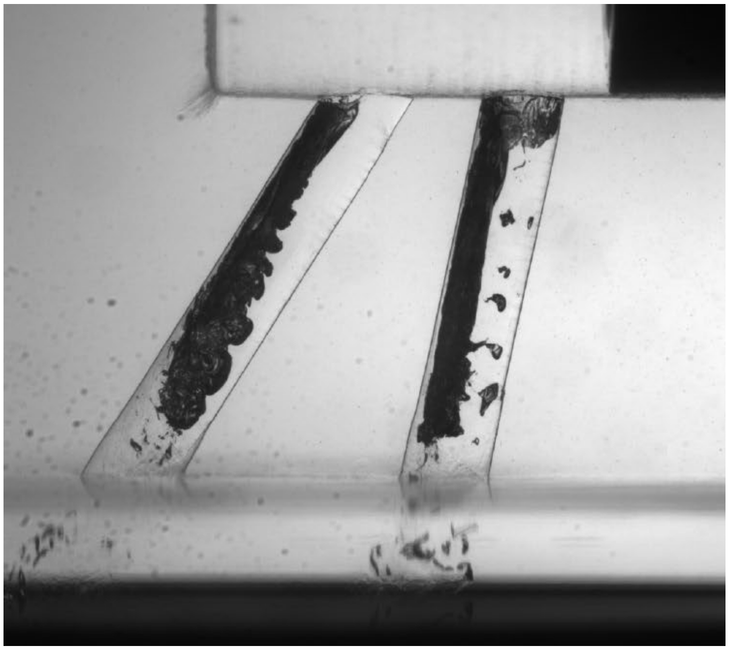

Figure 1.1 Hydraulic cavitation occurring in a fuel injector model. Picture from Hult et al. [47]

(a) Damages produced by cavitation erosion on discharge section of a Francis turbine. Picture from Gohil et al. [48]

(b) Photograph of typical cavitation damage on the blade of a mixed flow pump. Picture from Brennen [10]

Figure 1.2 Pictures of damages caused by cavitation in hydraulic machines

In fact, after a cavity has formed, it is normally advected by the fluid. When the "bubble" passes through areas with pressure higher than the vapor tension, it collapses, producing shock waves that propagate away from the bubble generating (in most cases) undesired vibrations and stresses on solid walls (if the collapse happens near the metal surface).

So, starting from the second half of the 20th century, scientists and engineers concentrate their efforts to understand in a better way cavitation, with the aim to gain knowledges useful to avoid, limit or to take advantage of this phenomenon.

Though cavitation could appear similar to boiling (which is the other phenomenon that involves the formation of vapor bubbles), the driving mechanisms of these two phenomena are completely different. In fact, the cavitation transformation path can be displayed in the pressure-temperature phase diagram of any liquid fluid as a nearly isothermal transformation that involves a pressure drop below the liquid-vapor equilibrium curve, while the boiling transformation path can be visualized in the same diagram as an isobaric transformation which involves a temperature increase beyond the liquid-vapor equilibrium curve (see Figure 1.3).

Nowadays, cavitation is still one of the most popular research fields and involves scientists and engineers both on the experimental and the numerical modeling sides. Cavitation experiments are useful to understand all the mechanisms that characterize this phenomenon, but they can be conducted only using simple devices, while applications of engineering interest usually show more complex geometries.

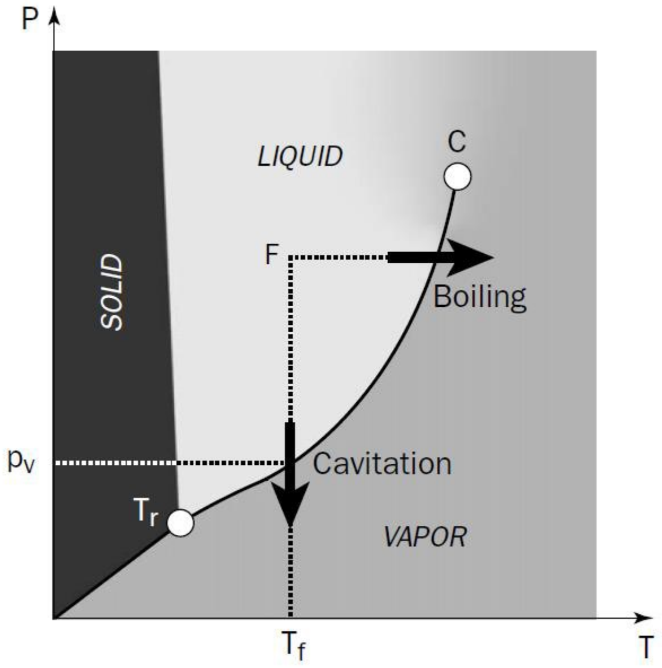

Figure 1.3 Pressure-Temperature phase diagram of water. Picture from Franc et al. [11]

Therefore, most of researchers' efforts are increasingly focusing on numerical modelling thanks to the growth of computational power. In fact, the introduction of CFD allowed the development of more sophisticated and accurate models that can be applied to study more complex problems after being validated on experimental data.

This approach is the basis of modern CFD techniques and potentially allows to save a lot of costs and time.

1.1 Cavitation patterns

In general, cavitation can appear in many different ways, depending on the geometry, on the liquid quality and on the operating conditions. According to their physical appearance, several types of cavitation patterns have been identified:

- **Travelling bubbles cavitation**: in this cavitation pattern, shown in Figure 1.4a, the cavities are formed by isolated bubbles which are convected downstream by the main flow. The isolated bubbles generate from weak point of the liquid, called *cavitation nuclei*, and the intensity of cavitation, in this case, mainly depends on the liquid quality, i.e. on the concentration of nuclei: the higher the nuclei concentration, the more intense will be the travelling bubbles cavitation phenomena.

- **Vortex cavitation:** this type of cavitation develops in the vortex cores where the pressure goes below the vapor pressure. It is quite common to see this cavitation pattern forming at the tip of the hub of rotating ship propellers blade, as it can be observed in Figure 1.4b.
- **Attached cavities / sheet cavitation:** cavitation develops onto a low pressure surface (such as suction sides of foils) and remain attached to it. When the cavity covers the whole surface, the phenomenon is called *supercavitation*, otherwise it is named *partial cavitation* (see Figure 1.4c).
- **Cloud cavitation:** it can be observed when unsteady attached/sheet cavities suffer detachment. This phenomenon can be affected by several mechanisms that develop in different regions of the flow. As shown by Figure 1.4d, the main feature of this cavitation pattern is the formation of clouds of many small vapor bubbles which shed downstream the detachment location.

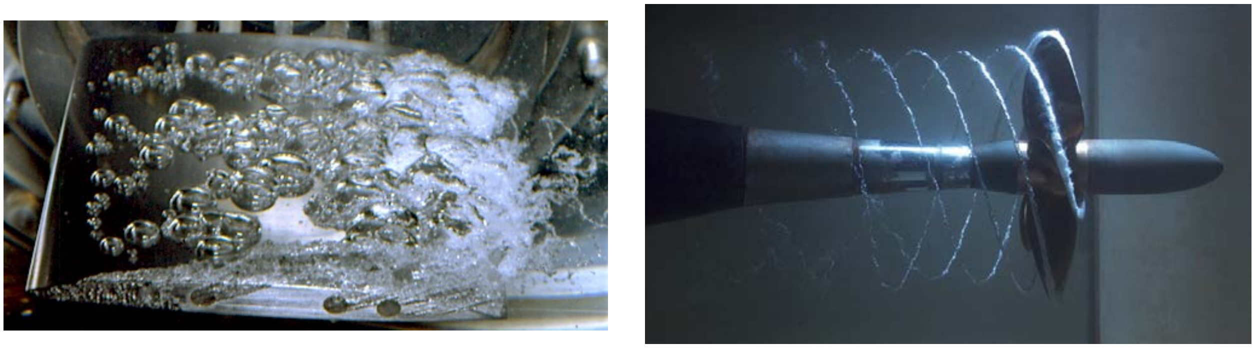

(a) Travelling bubble cavitation. Picture from Michel et al. [50]

(b) Vortex cavitation. Picture from Bosschers [49]

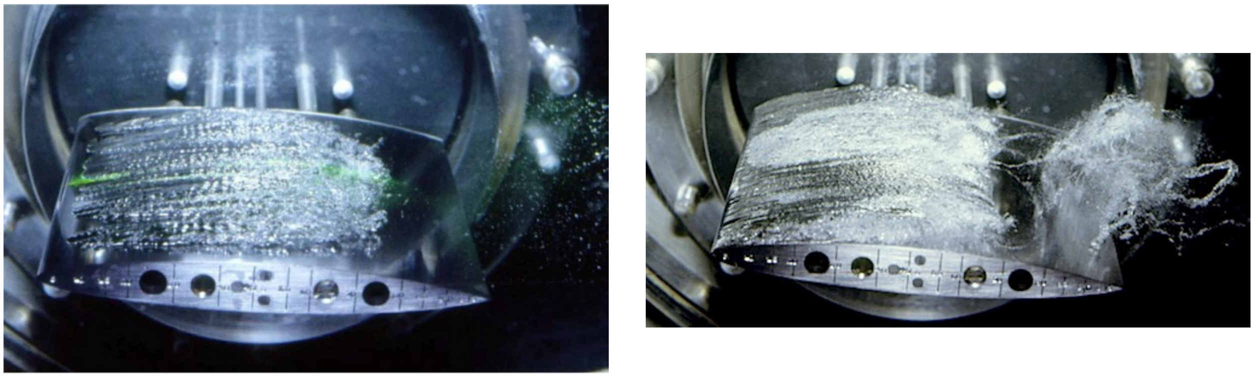

(c) Sheet partial cavitation. Picture from Cointe [15]

(d) Cloud cavitation mixed to sheet cavitation. Picture from Michel et al. [50]

Figure 1.4: Pictures showing examples of the four possible cavitation patterns

In the present graduation project, only the partial and cloud cavitation will be considered as they are the only two cavitation patterns that were observed by Hogendoorn [22] and Jahangir et al. [46] in their experiments. It must be underlined that works done by both Hogendoorn [22] and Jahangir et al. [46] represent the main references for the next validation case study.

1.2 State of Art

Cavitation literature, both from experimental and numerical modelling point of view, is basically focused on *unsteady cavitation*, that is one of the most common type of cavitation and consists in the periodic shedding of vapor clouds.

Both on the experimental and numerical sides, many publications made through the years have tried to explain what are the main physical phenomena and parameters that cause and influence the discontinuous formation of bubbles. Classical devices used for conducting cavitation testing and validation studies are nozzles (such Venturi's one) and hydrofoils.

In this section, the state of art of unsteady cavitation in Venturi nozzles is briefly described. In the first paragraph, the attention will be focused on cavitation experiments concerning Venturis, while the second paragraph concentrates more on the validation cases that involved such geometry.

In the following lines, the reader will not find references about experiments or numerical methods concerning hydrofoils (or concerning external flows in general) because the author, in the present case, is more interested in internal flows. However, in literature, a lot of studies on cavitating hydrofoils are available: for example, the works done by Dular et al. [1], Wei et al. [2], Hu et al. [3] and Michel et al. [50].

1.2.1 Unsteady cavitation in Venturi nozzles: experimental studies

For cavitation in internal ducts, one of the most important experimental studies on unsteady cavitation was made by Stutz et al. [25] using a classical video set in combination with stroboscopic light sheet to capture the cavitation cloud shedding phenomenon occurring into a cavitation tunnel (the experimental rig and the cavitation tunnel geometry are reported in Figure 1.5).

The authors observed the presence of an extended reversed flow occurring near the solid surface, responsible for the development of a break-off cycle and also conducted some measurements of void fraction evolution and local velocity within the cavities during the whole shedding process.

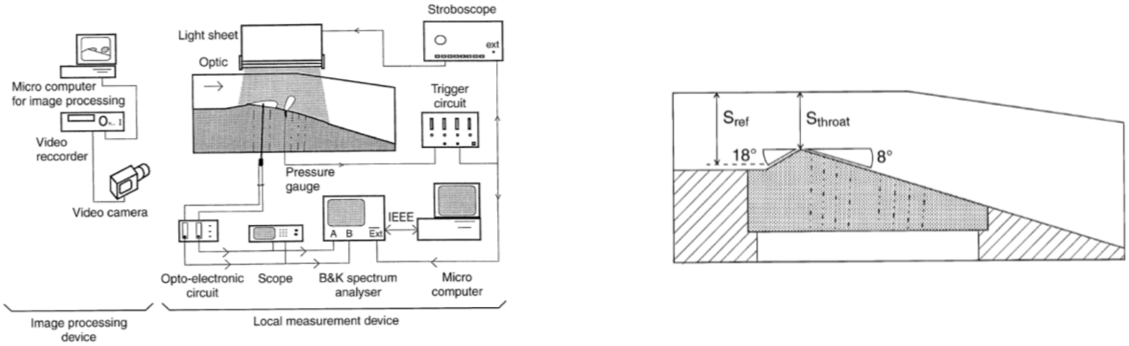

(a) Schematic representation of the test rig used by Stutz. Picture from Stutz et al. [25]

(b) Geometry of Stutz’s experiment cavitation tunnel. Picture from Stutz et al. [25]

Figure 1.5 Experimental set-up of Stutz’s experimental investigation on cavitation

To investigate the parameters that influence unsteady cavitation, Callenaere et al. [23] conducted experiments on a particular diverging step, analysing the re-entrant jet instability. The diverging step used by the authors (also provided with a mobile upper plate) allowed them both to vary the divergence angle and the width of the part of the channel interested by cavitation phenomena. In this work, it has been observed that the occurrence of cloud cavitation instability phenomenon depends on two main parameters: the adverse pressure gradient at the cavity closure and the cavity thickness. The influence of this second parameter on unsteady cavitation is not of easy perception at first sight, but the authors explained it referring to the interaction between the cavity interface and the re-entrant jet.

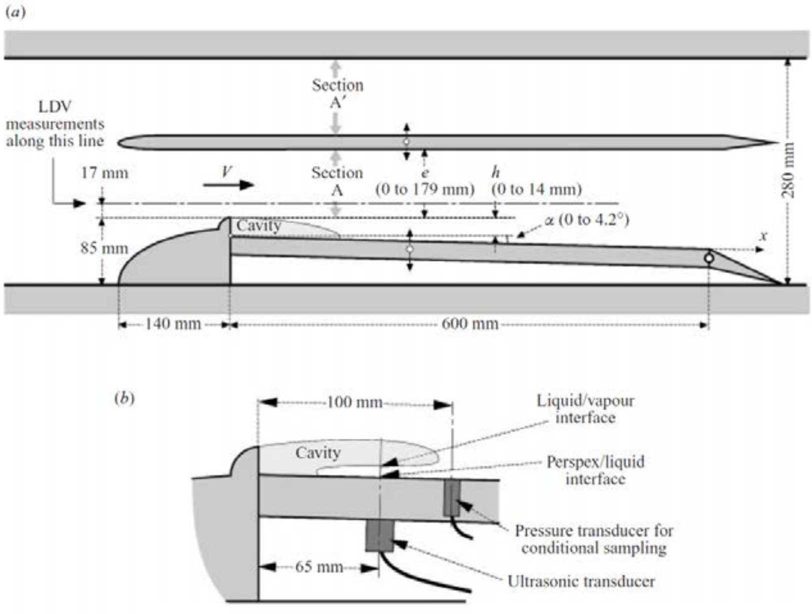

Figure 1.6 Schematic representation of the diverging step used by Callenaere. Picture from Callenaere et al. [23]

The dynamics of partial cavitation was also investigated experimentally by Hogendoorn [22] and Jahangir et al. [46]. The authors conducted their tests on an axisymmetric converging-diverging nozzle through the use of shadowgraphy technique and they observed that the vapor cloud shedding (that originates from the throat of the Venturi) is caused by two different mechanisms, called "re-entrant jet mechanism" (phenomenon driven by adverse pressure gradient) and "bubbly shock mechanism" (mechanism induced by the collapse of previously shedded vapor cavities). The occurrence of one mechanism instead of the other depends on the cavitation number. The authors also investigated the influence of the cavitation number on some other parameters, as flow blockage, shedding frequency and cavity length.

Experimental studies on unsteady cavitation in Venturi tube were also performed by Rudolf et al. [24] and highlighted the existence of three different cavitation regimes: *partial cavitation, fully developed cavitation* and *supercavitation regimes*. The occurrence of one of this three regimes depends, once again, on the cavitation number.

1.2.2 Unsteady cavitation in Venturi nozzles: CFD modelling

All the experimental studies made in the field of unsteady cavitation played a crucial role for numerical modelling of cavitation phenomena research, because they provide the experimental data on which validation cases could rely on.

In literature, a lot of different validated models have been reported, showing many different ways to proceed. The main differences, emerged from the consultation of these studies, are in the choice of the type of flow (single phase or multi-phase flow), in the selection of the cavitation model and in the choice of the turbulence model, as well as the geometry of the systems.

Reboud et al. [21] and Coutier-Delgosha et al. [19] [20] successfully applied a two-phase homogeneous flow model with barotropic law for modelling cavitation on two Venturi type test sections, assuming no-slip condition between the two phases. k-ε turbulence model was also used by the authors with an empirical reduction of the turbulent viscosity (using a coefficient called, in literature, *Reboud correction*).

Both these two authors, with their studies, highlighted the importance of the choice of turbulence model in cavitation problems: indeed, classical turbulence model without modifications aren't able to properly simulate the cavitating flows because the assumption of no-slip condition between the phases behaves like an artificial increase of dissipation, brings to overestimation of turbulent viscosity and to the formation of nearly-stable cavities. The introduction of a reduction factor is necessary to obtain results in good agreement with the experimental ones.

Usage of Reboud's correction coefficient, also with different cavitation and turbulence models, can be found in many other publications: for example, Coutier-Delgosha et al. [18] applied the same barotropic cavitation model to a Venturi section to test four different turbulence models: the standard k-ε model, the modified k-ε model with Reboud correction, the standard k-ω model and the k-ω model including compressibility effects. The authors found again that standard models are not able to simulate the cavitation physics properly, while the modified turbulence models work fine: indeed, these models introduce reduction in turbulent viscosity, accounting also for slip between the two phases and for compressibility effects.

Also Koukouvinis et al. [16] tested the performance of different turbulence models (standard and modified k-ε and k-ω, Large Eddy Simulation with WALE sub-grid model), even examining different cavitation models, as single-phase barotropic Homogeneous Equilibrium Model (HEM) and two-phase Schnerr-Sauer and Zwart-Gerber-Belamri models. All the combinations were applied for validating the Diesel cavitating flow through a square throttle and best agreement with experimental data was found for all the cavitation models using LES turbulence model. Then, the authors used validated models to simulate the internal flow of a Diesel injector.

Finally, in his Master Thesis, Zambon [13] conducted a validation case based on the experimental results obtained by Jahangir. The Venturi nozzle cavitating flow was simulated as axisymmetric, using both full Rayleigh-Plesset and Schnerr-Sauer cavitation models with Volume of Fluid (VOF) multi-phase method. Both classical and modified k-ε and k-ω turbulence models were applied considering both phases as incompressible. This validation test confirmed classical turbulence models unsuitability for cavitating flows, while the other models were able to simulate properly vapor shedding. The best results were obtained by the modified (with Reboud correction) k-ω Schnerr-Sauer model, demonstrating that, for this kind of cavitating flows, vapor tension and bubble acceleration growth contributions of Rayleigh-Plesset equation are negligible. This model was then applied for simulating the internal flow of large two-stroke Diesel engine injectors.

Other authors, as Cointe [15] and Gorkh et al. [14], carried on validations of unsteady cavitating flows considering Jahangir's geometry and results and treated the flow as inviscid. Their choice was, at first sight, justified by the high Reynolds number values occurring, allowing them to assume viscosity as negligible.

Cointe [15], in his study, treated the two-phase flow as a single pseudo fluid, assuming Homogeneous Mixture model and considering Merkle as cavitation model. Otherwise Gorkh et al. [14], applying Homogeneous Mixture Model too, assumed a barotropic state law for liquid-vapor mixture to reproduce cavitation. To simulate in a proper way the effect of shock waves given by the bubble collapse (specific of bubbly shock mechanism) he also relied on Euler compressible equation.

Both these validation cases were able to capture the two mechanisms responsible for unsteady cavitation phenomena (re-entrant jet and bubbly shock mechanism), but corresponding shedding processes were not reproduced with proper frequencies and characteristic length.

In the last decade, improvements in computational power and methods made possible to study cavitation phenomena with turbulence models different from RANS models, as LES models.

Large Eddy Simulations are scale resolving turbulence models: this means that they resolve the largest turbulent scales of flows, while the smallest scales (that are also more expensive to solve from the computational point of view) are low-pass filtered and modelled through the usage of a sub-grid scale (SGS) model.

Large Eddy Simulations are certainly more expensive than RANS, but in general return finer results with much lower computational costs than DNS (Direct Numerical Simulations), that resolve turbulence up to the smallest scales, defined by Kolmogorv's length and time scales.

The possibility to simulate cavitating flows with more accurate LES turbulence models was exploited by Dittakavi et al. [17], who studied the interactions between turbulent flow and cavitation in a Venturi nozzle applying LES Dynamic Smagorinsky Sub-**G**rid Scaling model to fully compressible Navier-Stokes equations coupled with Homogeneous Equilibrium cavitation model.

Tomov et al. [51] used fully compressible Navier-Stokes equations coupled with Homogeneous Equilibrium Mixture model to validate the cavitating flow in a Venturi type nozzle. As turbulence model, the authors chose to use an ILES model (Implicit LES). The obtained results were in good agreement with the experimental ones and also helped in detecting a new symmetric cavity dynamics mechanism, called *side-entrant jet*, responsible for partial cut of cavities near Venturi walls.

The most recent publication found is by Wang et al. [33]. The authors of this article described their using of LES WALE (Wall Adaptive Local Eddy Viscosity) Sub-Grid Scaling model with Homogeneous Equilibrium flow model and Zwart-Gerber-Belamri cavitation model to simulate the internal flow of an axisymmetric Venturi tube. The validation results were then used to improve a pre-existing 1-D model able to predict pressure fluctuations caused by cavitation.

1.3 Thesis Project and its Objective

The aim of this graduation project is to provide a solid numerical approach to simulate partial cavitation in internal flows when turbulence phenomena are modelled by the usage of Large Eddy Simulation turbulence model. To achieve this objective, two different validation cases are carried on with the purpose of testing how the choice of the sub-grid scaling model influences the results of LES cavitation simulations.

The project was conducted in collaboration with the *Technical University of Denmark - DTU*, which provided all the computational resources necessary to perform all the simulations of the present validation case.

The project developed according to the following steps:

- Literature review and critical analysis of papers on partial cavitation occurring in Venturi nozzles and how this cavitation phenomena have been modelled so far in Computational Fluid Dynamics. Particular attention was also given to the influence of the turbulence model on cavitation simulation, focusing on Large Eddy Simulation methodology.
- Study of the most appropriate method for the assignment of realistic inflow conditions. The simulation of the fully developed turbulent flow in a periodic pipe is performed to extract the turbulence and velocity mean profiles from one of the two periodic interfaces of the pipe.
- Validation of unsteady cavitation applying (as Venturi nozzle inflow conditions) the turbulence and velocity profiles previously obtained. The simulation of the periodical shedding of vapor bubbles in a converging-diverging nozzle is performed and the results are compared with the experimental data obtained by Hogendoorn [22] and Jahangir [46].

Since the characteristic Reynolds number of the system is really high, it took a very long time to complete all the simulations. This fact confirms that, in general, Large Eddy Simulations are still very expensive in terms of computational costs, but they also give more accurate results compared to unsteady RANS simulations.

1.4 Report structure

The outline of the report is next described. Chapter 1 (the current one) briefly introduces the problem and describes the theory behind the project and the general objective of the Thesis.

Chapter 2 is the *Theory* chapter: in this Thesis part all the theoretical aspects are elaborated with the aim of gaining more confidence in cavitation topics and understanding which are the major mechanisms responsible for unsteady cavitation in Venturi nozzles. The equations that rule the dynamics of vapor bubbles are also described. Finally, a general and brief presentation of the theory of turbulence is proposed.

Chapter 3 analyse and explains in detail the different mathematical models which will be used in the simulations, from the governing equations to the adopted cavitation models and the turbulence models.

Chapter 4 will present the computational set-up, based on the experiments made for the study of the different cavitation regime by Hogendoorn [22] and Jahangir et al. [46]. Due to the importance of the mesh settings for scale-resolving turbulence models, more attention will be given to the mesh characteristics, also explaining why such settings were adopted.

Chapter 4 also reports how information about the inflow boundary conditions were obtained, starting from the LES simulation of the fully developed turbulent flow of a periodic pipe. Finally, the initialization strategy and the implementation of the two models in STAR CCM+ are described too.

In Chapter 5, the results of the two simulations will be shown, discussed and compared to the experimental data provided by Hogendoorn [22] and Jahangir [46].

At last, in Chapter 6 the conclusions of this study will be presented. Future prospects will also be discussed in the final paragraph.

Chapter 2

Theory

This chapter has the aim of providing the reader with the basic notions concerning cavitation in nozzles. In the first part of this section, a brief explanation of the 1-D theory concerning cavitation in Venturi nozzles is given, also defining several useful non-dimensional parameters.

In the second part, the three principal mechanisms responsible for the occurrence of cloud cavitation phenomena in Venturi nozzles (which are the *re-entrant jet mechanism*, the *bubbly shock mechanism* and the *side-entrant jet mechanism*) are introduced, giving particular attention to the first two mechanisms.

Then, the focus shifts on the experimental studies conducted by Hogendoorn [22] and Jahangir et al. [46] on the development of partial cavitation phenomena in Venturi nozzles. In the third part, a short description of the nozzle geometry and of the experimental set-up is provided, also reporting the obtained results with a brief discussion on how the cavitation number affects the cavitation dynamics in nozzles.

The full derivation of the *Rayleigh-Plesset* equation is then presented inside the fourth part of this chapter, describing the main assumptions that were made in 1917 by Lord Rayleigh to obtain such bubble dynamics model.

Finally, the general theory of turbulence is provided in the last part of this *Theory* section, also reporting and explaining the three Kolmogorov's hypothesis that rule the *energy cascade* concept first described by Richardson in 1922.

2.1 Venturi cavitation background

As previously described in the *Introduction* part, *hydrodynamic cavitation* can occur in Venturi nozzles due to the flowing conditions, in particular when the liquid experiences large pressure decreases in its flow. Before analysing the reasons that underlie the *hydrodynamic cavitation* occurrence in a Venturi nozzle, let us first define which are the most important parameters of the Venturi geometry.

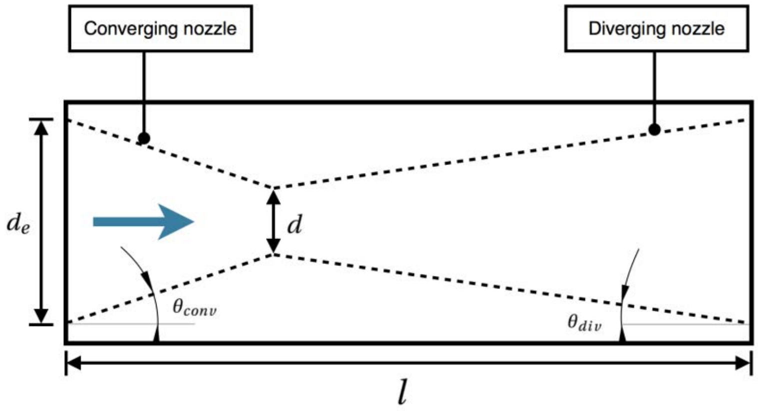

Figure 2.1 Schematic overview of an axisymmetric converging-diverging nozzle and its parameters. The blue arrow shows the direction of the flow. Picture from Cointe [15]

The classic geometry of a Venturi nozzle is reported in Figure 2.1, which also shows the major parameters used for its description.

Basically, an axisymmetric Venturi nozzle is composed of two parts. In the first part, the flow enters in a converging nozzle where the cross-sectional area decreases until the Venturi throat is reached. Knowing the throat diameter d, the geometry of this part can be totally defined by the use of the following two parameters:

- Area ratio of the converging nozzle, that is the ratio between throat and inlet cross sectional areas
- The convergence angle $2\theta_{conv}$

The second part, which starts from the throat, is a diverging nozzle: this means that, in this section of the Venturi, the cross-sectional area progressively increases. Once the throat diameter d is known, the geometry of the second part can be totally defined by the use of the following two parameters:

- Area ratio of the diverging nozzle, that is the ratio between throat and outlet cross sectional areas
- The divergence angle $2\theta_{div}$

The total length l of the Venturi nozzle can be easily computed once all the previous parameters are available.

A simplified explanation of how *hydrodynamic cavitation* generates in Venturi nozzle making the following assumptions:

- Steady 1-D flow
- Incompressible flow

- Inviscid flow
- Irrotational flow
- Eventual quota differences are neglected

Following the previous hypothesis, the 1-D velocity can be computed considering the volumetric flow rate conservation equation:

$$u\,A = \text{constant} \tag{2.1}$$

Where A is the area of a generic cross sectional surface and u is the magnitude of the velocity vector normal to the respective surface.

From equation (2.1) we can say that, given the volumetric flow rate, velocities and cross sectional areas follow an inverse proportionality law: this means that when the cross sectional area decreases (as in the case of the converging part of a Venturi nozzle) the velocity raises and when the cross sectional area increases (as in the case of the diverging part of a Venturi nozzle) the velocity decreases.

Considering the assumptions previously made, also the *Bernoulli equation* is valid and can be used to provide a simplified link between the pressure field and the velocity field:

$$p + \rho\frac{u^2}{2} = \text{constant} \tag{2.2}$$

Where p is the static pressure and ρ is the fluid density.

As you can see analysing equation (2.2), if the velocity increases along the flow (as occurs in a converging nozzle), the fluid experiences a decrease in pressure, while, on the other hand, if the velocity decreases (as in a diverging nozzle), the fluid pressure increases.

Combining the effects of equations (2.1) and (2.2), we can state that in the Venturi converging section pressure progressively lowers, while in the diverging one a pressure recovery occurs.

Following the previous reasoning, the section which can experience the lowest pressure is the throat section. In fact, this is the smallest among all the Venturi sections: consequently, the surface average velocity will reach its maximum value at this location and pressure its minimum.

Therefore, the cavitation onset and the growth of cavitation nucleus are expected to occur at the Venturi throat as shown in Figure 2.2. This fact is also confirmed by several experimental studies [22] [46].

To be more precise, the cavitation inception is not expected to occur in the whole throat section, but only close to the walls. This aspect can be easily explained observing the streamlines distribution of a generic converging-diverging nozzle shown in Figure 2.3.

As you can notice, the streamlines density close to the wall of the throat section is higher than the streamlines density at the core of the flow. Higher local densities of streamlines mean larger local velocities and consequently lower local pressure values. This implies that, at the throat, the near-wall local velocities are larger than the core velocity.

Thus, a pressure drop below the vapor pressure (and so cavitation) is more likely to occur at the neck of the Venturi than at the core. This also means that it is not necessary to have the whole throat at a pressure lower than the vapor pressure to develop cavitation: indeed, cavitation begins when the local pressure falls below the critical value, regardless of the position in which this occurs.

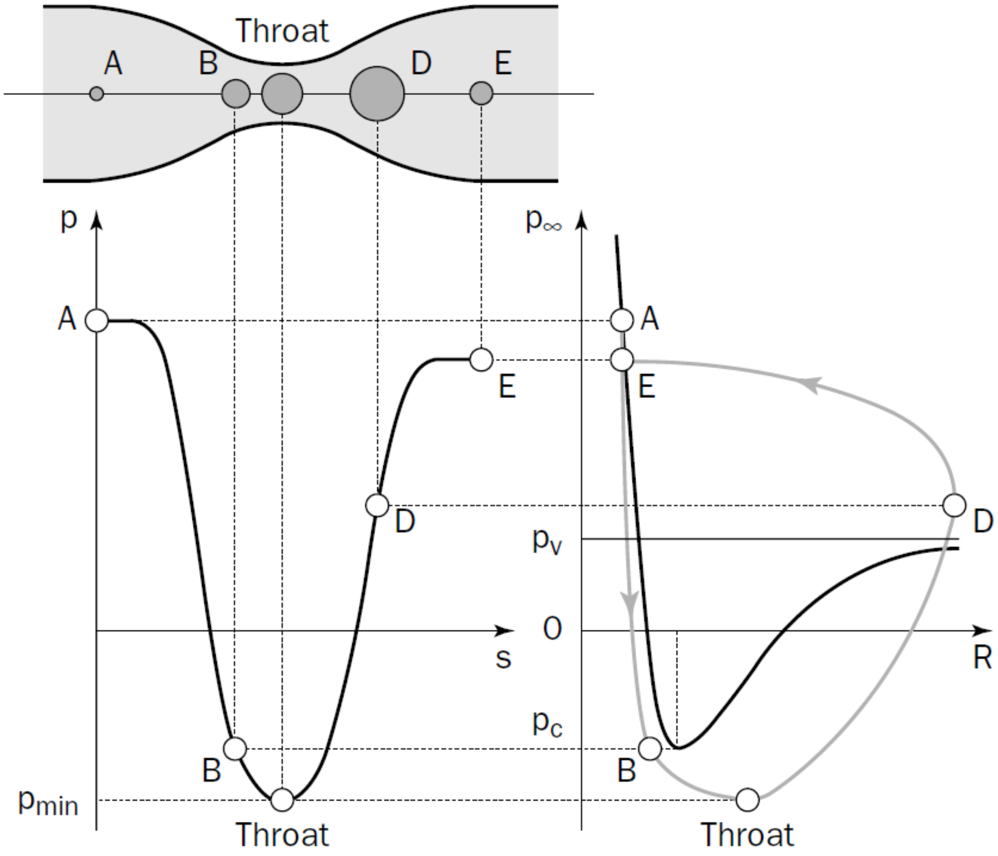

Figure 2.2 Typical evolution of cavitation nucleus in a converging-diverging nozzle. Picture from Franc et al. [11]

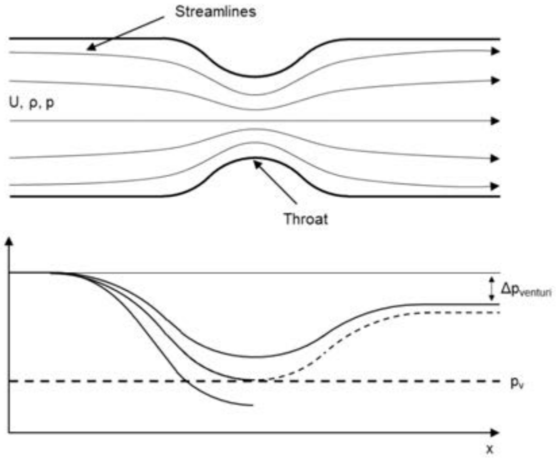

Figure 2.3 Streamlines (above) and pressure (below) distribution along a one-dimensional converging-diverging nozzle. The dotted line shows the onset of a multi-phase flow. Once the cavitation inception has occurred, it is not possible to describe precisely the pressure distribution far from the Venturi throat. Picture from Hogendoorn's Master Thesis [22]

2.1.1 Relevant Non-Dimensional Numbers

Cavitation Number

It is the first and most important non-dimensional parameter used to describe the intensity of a cavitating flow. Generally, the *cavitation number* is defined as:

$$\sigma = \frac{p_{ref} - p_v}{\frac{1}{2}\rho u_{ref}^2} \tag{2.3}$$

Its definition is based on the reference conditions of the flow, which depend on the application and on the choice of the locations where to compute quantities of interest. Hogendoorn [22] and Jahangir et al. [46] define the cavitation number taking the outlet static pressure as reference pressure and considering the free stream throat velocity as reference velocity. Following these assumptions, the cavitation number is then defined as:

$$\sigma = \frac{p_{out} - p_v}{\frac{1}{2}\rho u_0^2} \tag{2.4}$$

In general, lower values of the cavitation number mean higher intensity of cavitation phenomena. This trend is confirmed by equation (2.4).

In fact, with the same outlet pressure, an increase in the free stream throat velocity u_0 (that implies lower throat pressure and consequently higher intensity of cavitation) brings to lower values of cavitation number.

Also a decrease in the outlet static pressure value brings to lower cavitation numbers and consequently to more intense cavitation phenomena. To explain this fact, let us consider a case in which the inlet static pressure is fixed.

High values of the outlet static pressure (but of course still lower than the inlet static pressure) imply low pressure jumps Δp between inlet and outlet and, according to Bernoulli equation (2.2), also low throat velocities. For these conditions, which correspond to high values of the cavitation number, cavitation is not likely to occur.

On the contrary, low outlet static pressure values lead to large pressure jumps and consequently to high velocity flows through the Venturi neck. This type of flow, for which the cavitation onset is more likely to happen, are described by small values of the cavitation number.

Strouhal Number

The *Strouhal number* is a very important parameter used to describe systems where periodic phenomena occur. It is used by Hogendoorn [22] and Jahangir et al. [46] to describe the characteristic frequencies of the cloud shedding process as the cavitation number varies.Generally, this adimensional parameter is defined as follows:

$$St_L = \frac{fL}{u_{ref}} \tag{2.5}$$

Where f is the characteristic frequency of the process, L is the referece length and u_{ref} is the reference velocity. In our case, the frequency f is the shedding frequency of the partial cavities observed in the Venturi nozzle, while the free stream throat velocity u_0 is taken as reference velocity.

In literature many different definitions of the Strouhal number are available, depending on the choice of the reference length L. In this Thesis work, two different length (throat diameter d and cavity length at time of detachment L_{cav}) have been identified as reference length, so two different definitions of the Strouhal number were adopted:

$$St_d = \frac{fd}{u_0} \quad \text{using } d \text{ as reference length} \tag{2.6}$$

$$St_l = \frac{fL_{cav}}{u_0} \quad \text{using } L_{cav} \text{ as reference length} \tag{2.7}$$

Pressure Loss Coefficient

The presence of a partial cavity developing from the Venturi throat brings to pressure losses Δp along the nozzle due to the sudden flow expansion and the wall friction. So, in general, the *Pressure Loss Coefficient* can be defined as follows:

$$K = \frac{\Delta p}{\frac{1}{2}\rho {u_{ref}}^2} \tag{2.8}$$

Hogendoorn [22] and Jahangir et al. [46] in their works compute the pressure losses as the pressure jump between the nozzle inlet and the nozzle outlet, while as reference velocity the free stream throat velocity u_0 is considered. Consequently, the pressure loss coefficient definition used in this project is described below:

$$K = \frac{p_{in} - p_{out}}{\frac{1}{2}\rho {u_0}^2} \tag{2.9}$$

Reynolds Number

The *Reynolds number* describes the degree of turbulence of the flow and it is defined as the ratio between the inertial forces and the viscous forces. In general, it can be computed as follows:

$$Re_L = \frac{\rho u_{ref} L}{\mu} \tag{2.10}$$

Where u_{ref} is the reference velocity, L is the reference length, while ρ and μ are respectively the density and the dynamic viscosity of the fluid. In this project, the characteristic Reynolds number of the system is computed considering the throat diameter d and the free stream throat velocity u_0.

$$Re_d = \frac{\rho u_0 d}{\mu} \tag{2.11}$$

Considering flow in pipes, laminar flow occurs when $Re_d < 2000$. Otherwise, the flow is considered as turbulent.

2.2 Cloud shedding mechanisms in converging-diverging nozzles

In literature, depending on the cavitation number, three main cavitation cloud shedding mechanisms have been identified in Venturi nozzle through experimental studies: they are the *re-entrant jet mechanism*, the *side-entrant jet mechanism* and the *bubbly shock mechanism*.

In this section, the focus will be given mostly to the theory that underlies the re-entrant jet mechanism, which is the only responsible mechanism for the unsteady cloud shedding process in this project.

Also a brief description of the bubbly shock mechanism will be given, despite this mechanism does not occur for the set of boundary conditions chosen for the validation test.

The author also underlines that, in this work, the reader will not find references about the side-entrant jet mechanism, because this mechanism does not occur in axisymmetric geometries, but only in square section channels. For further explanation about this shedding mechanism, the reader can refer to the work done by Tomov [51].

2.2.1 Re-entrant jet mechanism

The re-entrant jet mechanism is the first and most studied cavitation shedding mechanism and, in most cases, is the main responsible for the cloud cavitation phenomena occurring in devices of engineering interest such as nozzles and injectors. Identified for the first time in 1955 by Knapp [52], it was also observed by many other researchers in their experiments, as Callenaere et al. [23], Stanley et al. [35], Hogendoorn [22] and Jahangir et al. [46] and all these authors agree on the defining this phenomenon as driven by an adverse pressure gradient. The whole shedding cycle specific for this mechanism can be generally explained by the following steps (see Figure 2.4a):

1. After being advected downstream by the flow, the cloud (B), that has formed during the previous cycle, brakes-up. The shocks generated by the cloud brake-up propagate towards the new fully developed cavity (A) of length L_{cav}, and develops the re-entrant jet (C).

2. The re-entrant jet (C) further develops and continues to travel towards the attachment point of the cavity (A).
3. The re-entrant jet reaches the attachment point of the cavity (A) and disconnects the cavity from the nozzle walls, forming the new cloud (B).
4. The new cloud (B) is advected downstream by the flow. In the meantime, a new cavity (A) forms again starting from the nozzle throat.
5. The cloud (B) continues to shed downstream the flow until it brakes-up. A new re-entrant jet (C) forms at the fully developed cavity apex.
6. The shedding cycle repeats following the previous steps.

All the steps previously described are schematically drawn in Figure 2.4a, that reproduces the conditions of the cavitation test made by Stanley et al. [35] using a cylindrical orifice.

Figure 2.4b, instead, shows the re-entrant jet mechanism shedding cycles detected by Hogendoorn during its experiments: it refers to a cavitation number equal to one ($\sigma = 1$).

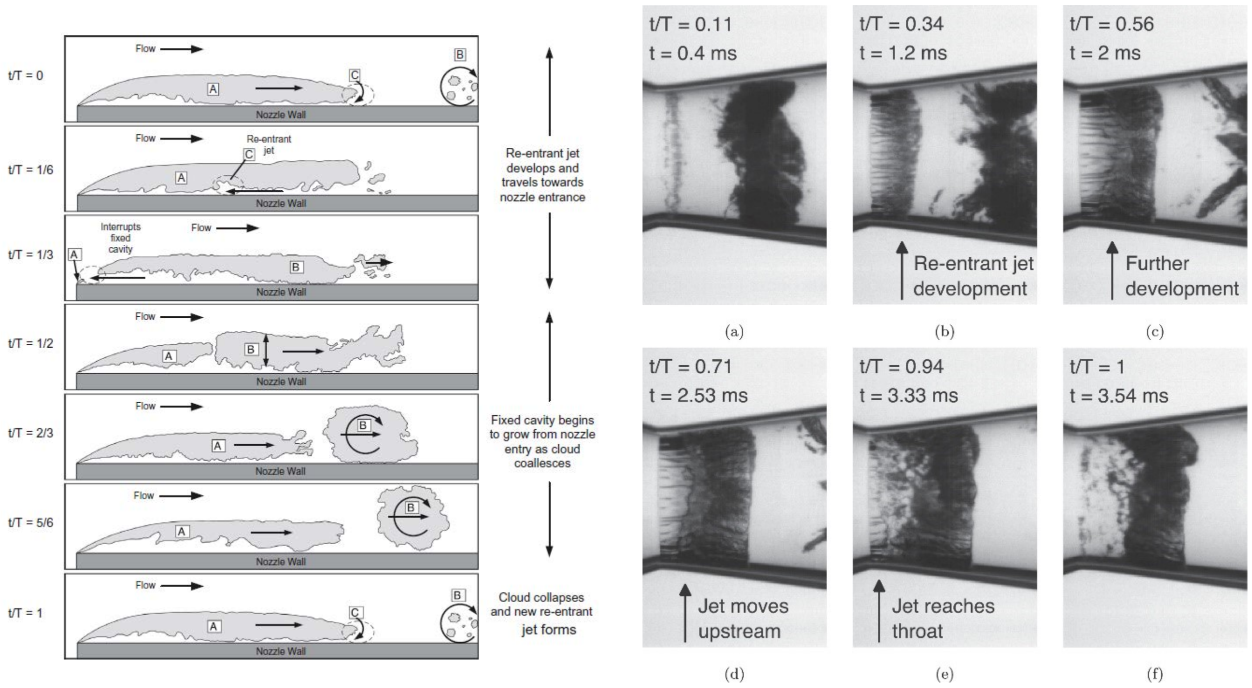

(a) Schematic illustration of the re-entrant jet mechanism that develops inside a cylindrical orifice according to Stanley et al. [35]

(b) Video frames of a cavitation shedding cycle caused by the development of the re-entrant jet. This mechanism was observed by Jahangir et al. [46] for $\sigma = 1$ while conducting cavitation experiments on a axisymmetric Venturi nozzle

Figure 2.4 Pictures showing the specific steps which the re-entrant jet mechanism follows in its development.

2.2.2 Bubbly shock mechanism

The bubbly shock mechanism is a cloud shedding mechanism driven by the shockwaves generated by the collapse of previously shedded bubble clouds.First identified in 2015 by Ganesh et al. [53], it was also detected by Hogendoorn [22] and Jahangir et al. [46]. All the experimental investigations concerning the bubbly shock mechanism report that this phenomenon occurs only for very low cavitation number, i.e. when cavitation phenomena are expected to be intense.

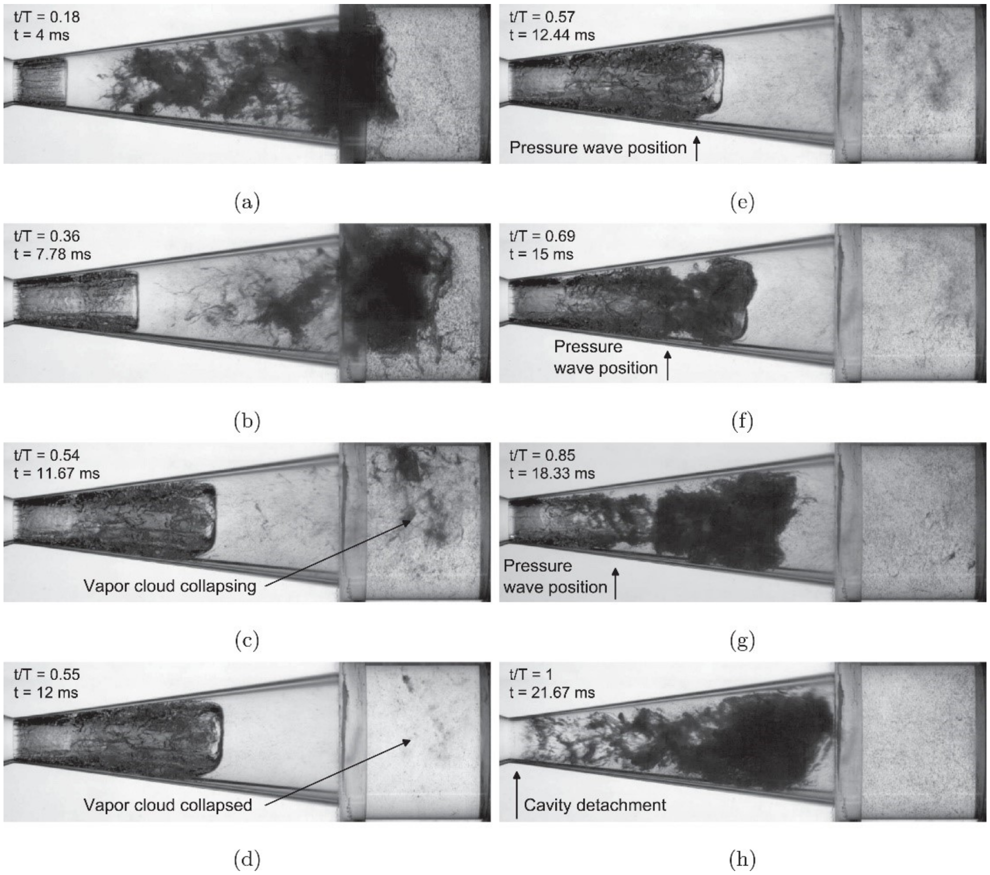

(a) (e)

(b) (f)

(c) (g)

(d) (h)

Figure 2.5 Video frames showing the development steps specific for the bubbly shock mechanism occurring in an axisymmetric Venturi nozzle for $\sigma = 0.4$. Pictures from Jahangir et al. [46]

In general, the shedding cycle specific for this type of cloud cavitation mechanism can be described following the next steps:

1. A vapor cloud formed in the previous cycle sheds downstream the diverging nozzle, while another cavity grows starting from the throat (Figure 2.5a)
2. The vapor cloud reaches the pressure recovery section of the Venturi while the new cavity continues to develop in the flow direction (Figure 2.5b)

3. The vapor cloud collapses generating a shock wave. This shock wave starts to propagate towards the Venturi throat, influencing the development of the new cavity (Figure 2.5c – 2.5g)
4. The shock wave reaches the throat and cuts-off the cavity from the walls. A new vapor cloud has formed and is advected downstream by the flow (Figure 2.5d)
5. The shedding cycle restarts: the cloud continues in its shedding while a new cavity forms and grows.

The steps that have been just described refer to Hogendoorn [22] and Jahangir et al. [46] works. The bubbly shock mechanism is shown in Figure 2.5.

2.3 Hogendoorn’s investigation overview

In this section, the experimental investigation conducted by Hogendoorn [22] is briefly described. The reason why an entire section of this Thesis is dedicated to the description of the work done by Hogendoorn is simple: all the experimental data on which our validation study relies were taken from Hogendoorn Master Thesis [22]. This experimental study has the aim of investigating the two principal shedding mechanisms which were treated in the previous paragraph: the *re-entrant jet mechanism* and the *bubbly shock mechanism.* First, the experimental rig and the Venturi geometry are introduced, also shortly explaining the techniques that were adopted to capture the dynamics of the vapor cavities. The experimental results are then reported and summarized.

2.3.1 Venturi geometry

The converging-diverging nozzle is made from polymethylmethacrylate (PMMA), which presents a very high value for the light transmission (1.49, close to that of the water).

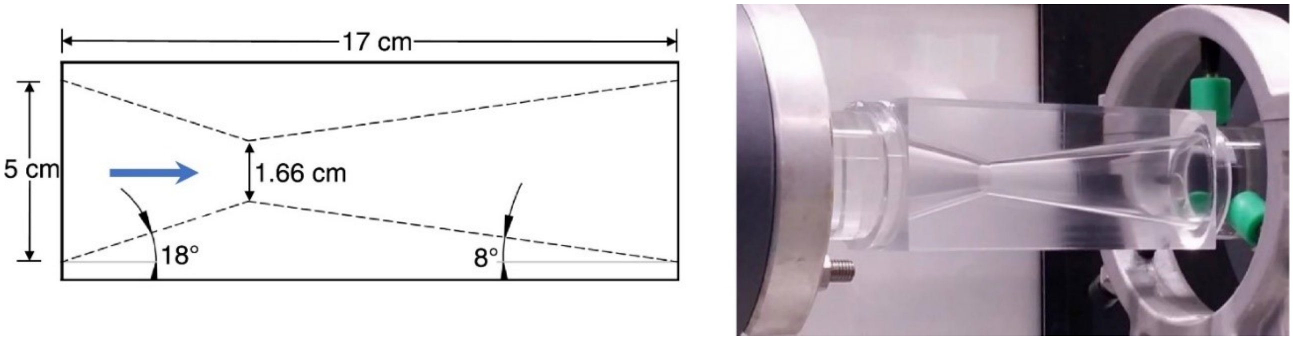

Figure 2.6 (*Left*) Main geometric parameters of the Venturi nozzle. (*Right*) Photograph of the converging-diverging nozzle in the experimental set-up. Picture from Jahangir et al. [46]

This property allows to achieve a good optical access to the cavitation dynamics inside the nozzle. The main Venturi geometric parameters are shown in Figure 2.6, as the flow direction (which goes from left to right).

A total divergence angle of 16° was chosen by the authors to avoid flow separation phenomena in the diverging section while maintaining a fairly rapid pressure recovery. Furthermore, an area ratio equal to 1:9 was adopted for both Venturi entrance and exit sections, while the converging section had a total angle of 36°.

2.3.2 Experimental apparatus

A schematic overview of the experimental set-up used by Hogendoorn during his experimental investigation is given in Figure 2.7. The flow is driven through the closed loop system by a centrifugal pump (10), which installation conditions were studied in order to avoid pump inside cavitation.

The length of the inlet-pipe (12) is set equal to 40D (D stands for the inlet-pipe diameter) in order to provide enough space to the flow to develop into fully developed turbulent flow before reaching the test section. Upstream and downstream pressure trasducers (1) and (3) are located respectively 0.31 m before the Venturi throat and 0.73 m after the Venturi throat. The outlet tube is 1.4 m long. After the outlet tube, there is a gradual transition to the 1.92 m long pressure recovery section (4): a transition angle of 5.7° is chosen to avoid flow separation and reduce flow losses.

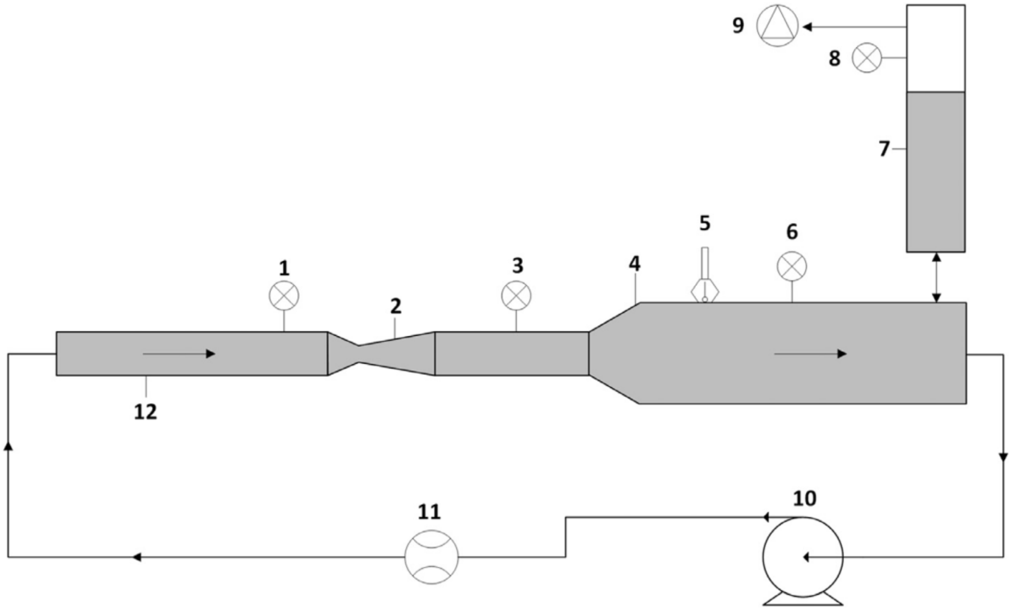

Figure 2.7 Schematic representation of the experimental rig. Picture from Jahangir et al. [46]

At the end of the pressure recovery section there is a vertical water column (7) which has the purposes of allowing the control of the global static pressure of the system and of collecting air bubbles entrained in the flow. The vacuum pump (9) located at the top of the water column can be used to further control the global static pressure of the system and allows to lower it up to a 20 kPa absolute pressure.

Being the flow converged before reaching the throat, an almost smooth velocity profile is expected at the Venturi throat. This implies that the influence of the boundary layer on flow separation is almost negligible [22]. However, turbulence plays a crucial role in determining the flow conditions inside the nozzle and the flow separation is enhanced for increasing Reynolds number values.

The cavity dynamics are captured through the use of shadowgraphy technique, which is presented as a scheme in Figure 2.8. In this method, the measurement target is place between the camera and a light source. The light source illuminates the nozzle from the back side in the direction of the camera.

Every object which passes in front of the light source (as a group of vapor bubbles) prevents the light to reach the camera and this results in dark spots in the camera images.

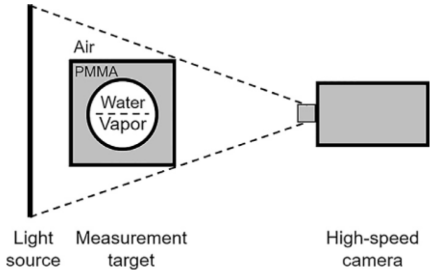

Figure 2.8 Schematic representation showing how image capturing shadowgraphy technique works. Picture from Jahangir et al. [46]

2.3.3 Results and conclusions

Hogendoorn, during his experiments, conducted tests varying the cavitation number: this was made possible by controlling and changing the pressure of outlet pipe. Two main shedding mechanisms were identified (the re-entrant jet mechanism and the bubbly shock mechanism) and it was observed that the occurrance of one mechanism instead of the other depends on the cavitation number.

Next, the influence of the cavitation number on the characteristics of the cavity dynamics observed by Hogendoorn is reported. To compare results that correspond to different conditions, Hogendoorn resorted to the use of several non-dimensional number, which were previously described.

Cavity length

As seen previously, the symbol L_{cav} indicates the cavity length at the time of detachment. This parameter was found by Hogendoorn to be function of the cavitation number. The link between these two parameters is shown in Figure 2.9, where the adimensional ratio beetween the cavity length and the Venturi throat diameter is plotted against the cavitation number for different outlet pressures. Observing Figure 2.10, we can state that, for decreasing cavitation numbers, the cavity length increases: this fact can be explained considering that, for lower cavitation numbers, the cavitation phenomena are expected to be more intense. This results in the development of longer cavities.

Flow blockage

There is no doubt on the fact that the presence of a cavity developing from the Venturi throat affects the flow: in particular, it tends to narrow the throat diameter of the flow (which no longer matches with the Venturi throat diameter) and restricts the minimum flowing cross sectional area.

The flow blockage effect (that is portrayed in the scheme of Figure 2.11) is more evident as the cavity length and thickness at the time of detachment grow. Since cavity length L_{cav} is function of the cavitation number, it is reasonable to think that also the flow blockage effect depends on such parameter.

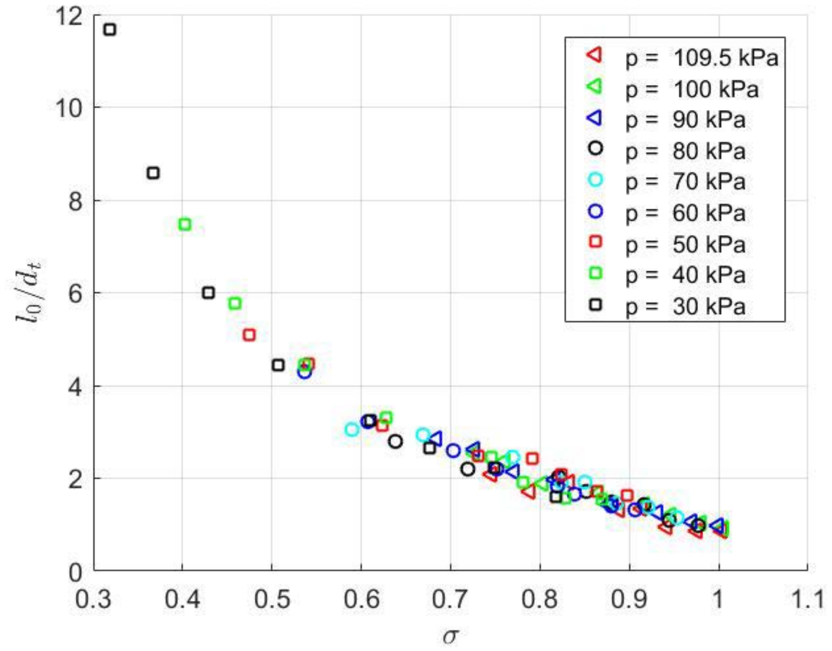

Figure 2.9 Picture showing the dependence of the average cavity length detected at time of detachment (scaled with the throat diameter) on the cavitation number σ. Picture from Hogendoorn [22]

A good indicator of flow blockage is the pressure loss coefficient K: in fact, as the flow throat narrows, the pressure losses raise and so does the pressure loss coefficient.

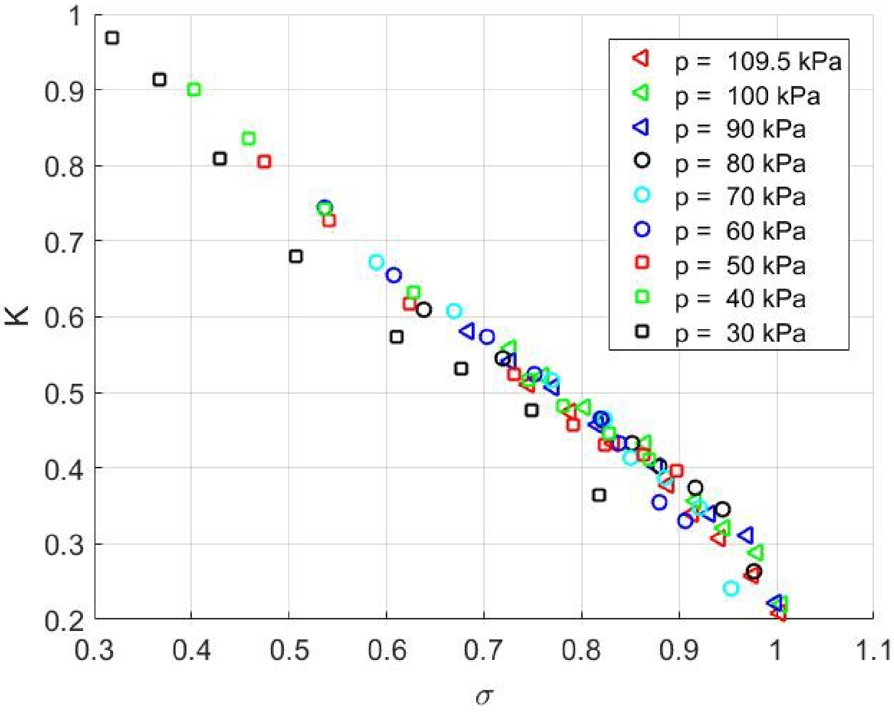

Figure 2.10 Picture showing the dependence of the pressure loss coefficient K on the cavitation number σ. All the experimental points seem to collapse in one straight line, showing that K is not function of the outlet pressure. Picture from Hogendoorn [22]

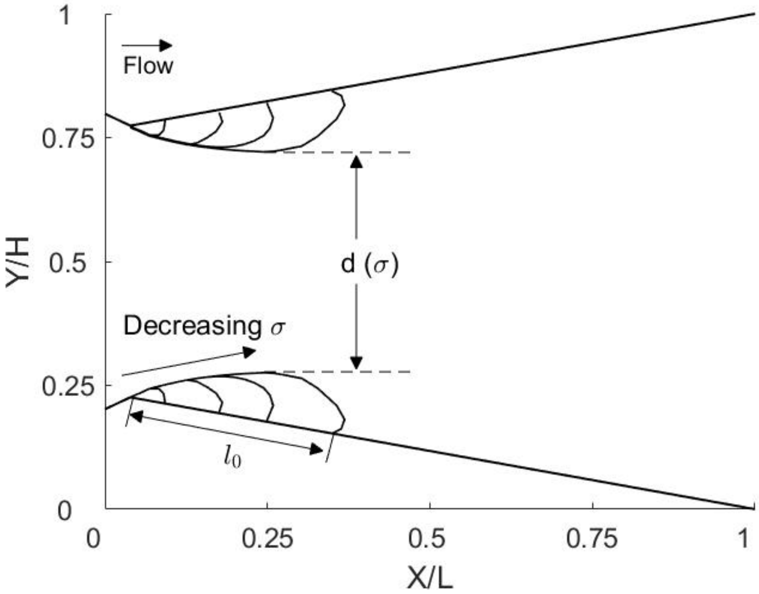

Figure 2.11 Sketch of the flow blockage phenomenon occurring at the throat of the Venturi as the cavity length increases. Picture from Hogendoorn [22]

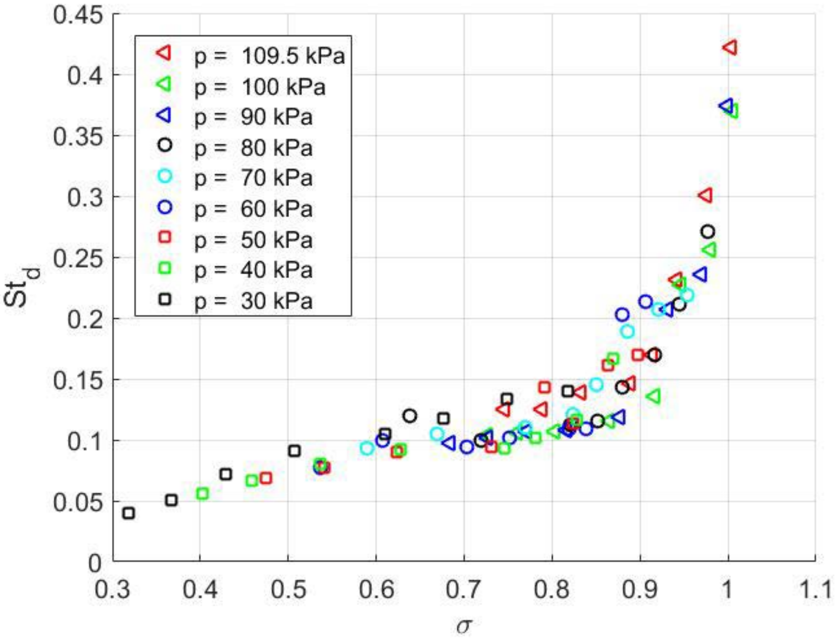

(a) Plot showing the dependence of the Strouhal Number St_d on the cavitation number σ

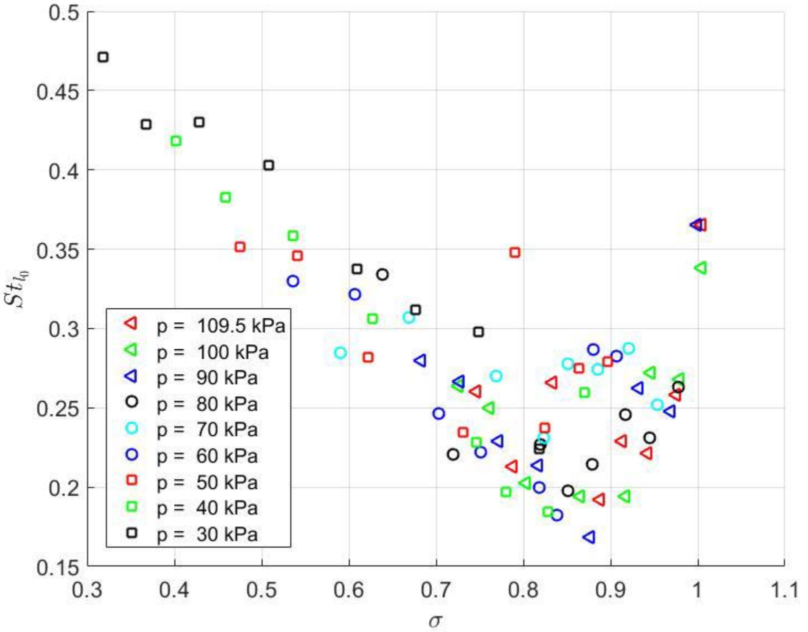

(b) Plot showing the dependence of the Strouhal Number St_l on the cavitation number σ

Figure 2.12 Picture showing the dependence of dimensionless frequency on the cavitation number. In the first picture, the Strouhal number is defined using the throat diameter as reference length, while in the second picture the cavity length at time of detachment is used. Pictures from Hogendoorn [22]

In his Master Thesis, Hogendoorn plotted K for different pressures as a function of the cavitation number and obtained the results shown in Figure 2.10.

Observing figure 2.10, all the results seem to collapse on a single line. This fact implies that flow blockage depends only on the cavitation number, and not on the outlet pressure of the system.

Characteristic shedding frequencies

Also the shedding frequency was found to be function of the cavitation number, so Hogendoorn plotted the dimensionless frequency (represented by the Strouhal number) against the cavitation number, and obtained two different charts, shown in Figure 2.12.

The plot in Figure 2.12a was obtained computing the Strouhal number with equation (2.6), i.e. considering the Venturi throat diameter as reference length, while, for computing the Strouhal number in the second plot (Figure 2.12b), the cavity length L_{cav} was taken into account.

Depending on the cavitation number, both plots shows three different trends that correspond to three different cloud shedding mechanisms:

- For low values of the cavitation number ($\sigma < 0.8$), the bubbly shock mechanism occurs
- For high values of the cavitation number ($\sigma > 0.95$), the re-entrant jet mechanism occurs
- For intermediate values of the cavitation number ($0.8 < \sigma < 0.95$), a transition regime is observed, where both mechanisms co-exist and can be observed.

2.4 Bubble dynamics: the Rayleigh – Plesset Equation

The *Rayleigh-Plesset equation* is an ordinary differential equation that rules the radial growth of a singular spherical bubble in an infinite domain of incompressible Newtonian liquid.

First stated by Lord Rayleigh in 1917 [39] and then applied for the first time to real cavitation problems by Plesset in 1949 [40], this model also makes the assumption of negligible mass exchange at the interface beetween vapour and liquid.

At first sight, this approach could seem very theorical and not appropriate for studying problems that involve real cavitation phenomena, but it allows to understand which are the most important parameters that really affect the physics of the growth and collapse of vapour bubbles.

In the following section, the theorical derivation of the *Rayleigh – Plesset equation* will be explained step by step. For further and more exhaustive explanation, the author suggests to refer to the works made by Brennen [10] and Franc et al. [11], on which the following exposition is based.

Let us consider a spherical bubble of radius $R(t)$ (where t indicates the variable of time) completely sorrounded by liquid. The next mathematical steps will rely on the following assumptions:

- The liquid is incompressible and Newtonian or inviscid. Both liquid density ρ_L and liquid dynamic viscosity μ_L are constant and uniform. Compressibility effects of the liquid are neglected;
- The liquid domain is infinite and, at its boundaries, both liquid temperature T_∞ and liquid pressure $p_\infty(t)$ are known. The pressure boundary condition is assumed as time dependant because, for example, it could be set as an input control during an experiment, while the temperature boundary conditions is assumed constant;
- The effects of gravity are considered as negligible;
- The bubble is filled homogeneously with vapor. All the properties of the vapor of the bubble are uniform, including bubble temperature $T_B(t)$ and bubble pressure $p_B(t)$. In particular, the bubble pressure is equal to the vapor pressure at the liquid bulk temperature $T_B(t)$;
- All the heat exchanges are neglected. The entire process is treated as adiabatic (this assumption is acceptable in case of large bubbles);
- No mass exchange occurs at the interface of the bubble.

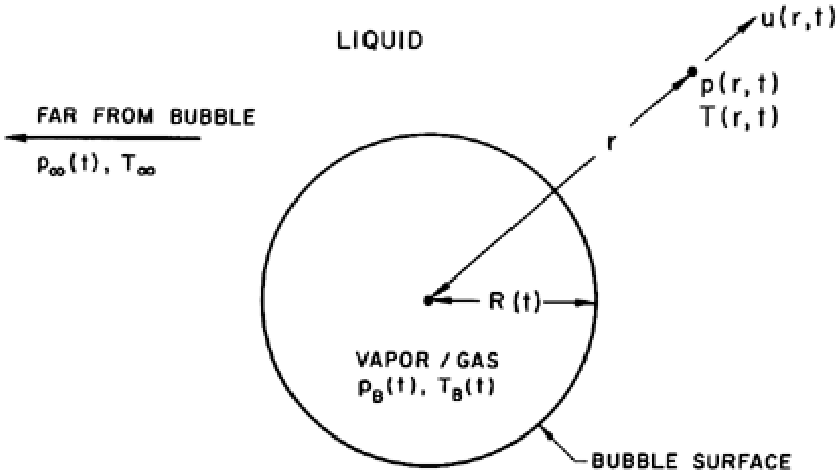

Figure 2.13 Schematic representation of the main parameters used to describe the geometry and the boundary conditions of the Rayleigh-Plesset problem. Picture from Brennen [10]

Assuming the center of the spherical bubble as the origin of our spherical coordinate system, we will indicate the distance between the bubble center and an arbitrary point of the liquid with the variable r. Consequently, the radial velocity referring to an arbitrary point of the liquid in an arbitrary time t will be indicated with the variable $u(r,t)$.

The functions to be determined for every point in the liquid domain (for which stand the condition $r \geq R(t)$) are the velocity $u(r,t)$ and the pressure $p(r,t)$. Their changes are induced by the evolution of the bubble. From the hypothesis of absence of mass transfer at the interface follows that the liquid velocity at the interface $u(R,t)$ is equal to the interface velocity $\dot{R} = \frac{dR}{dt}$, so:

$$u(R,t) = \frac{dR}{dt} \tag{2.12}$$

Considering the mass conservation for an incompressible fluid ($\nabla \cdot \vec{v} = 0$) and proceeding with its integration, the following relation can be obtained:

$$u(r,t) = \dot{R}\ \frac{R(t)^2}{r(t)^2} \tag{2.13}$$

The momentum equation along the radial direction is then taken into account without considering the viscous term of the Navier – Stokes equation (by initial hypothesis, the fluid is treated as inviscid):

$$\frac{\partial u}{\partial t} + u\frac{\partial u}{\partial r} = -\frac{1}{\rho_L}\frac{\partial p}{\partial r} \tag{2.14}$$

Substituting relation (2.13) into the equation (2.14), we obtain:

$$\ddot{R}\frac{R^2}{r^2} + 2\dot{R}^2\left[\frac{R}{r^2} - \frac{R^4}{r^5}\right] = -\frac{1}{\rho_L}\frac{\partial p}{\partial r} \tag{2.15}$$

Integrating with respect to r and considering the boundary conditions, one can achieve the following equation:

$$\frac{p(r,t) - p_\infty(t)}{\rho_L} = \ddot{R}\frac{R^2}{r} + 2\dot{R}^2\left[\frac{R}{r} - \frac{R^4}{4r^4}\right] \tag{2.16}$$

At the interface, for $r = R$, the previous equation becomes:

$$\frac{p(R,t) - p_\infty(t)}{\rho_L} = R\ddot{R} + \frac{3}{2}\dot{R}^2 \tag{2.17}$$

Pressure at the interface is unknown, so another relation must be taken into account to solve the equation (2.17). We can obtain this relation by imposing the equilibrium of forces in the normal direction with respect to the interface (this is made possible by the assumption of absence of mass exchange at the interface, so no condensation or evaporation occur).

Let us consider a control volume consisting in a small, infinitely thin lamina containing a short segment of the bubble interface: computing the radially outward normal stress in case of viscous fluid (kinematic viscosity ν_L), it results equal to:

$$t_{rr}(R,t) = -p(R,t) + 2\nu_L \left.\frac{\partial u}{\partial r}\right|_{r=R} \tag{2.18}$$

The balance of normal forces in the radially inward direction gives the following relation (the symbol γ indicates the surface tension of the liquid at the liquid temperature):

$$-t_{rr}(R,t) = p_B(t) - \frac{2\gamma}{R} \tag{2.19}$$

Combining equations (2.18) and (2.19), the pressure on the cavity interface is then given by:

$$p(R,t) = p_B(t) - \frac{2\gamma}{R} + 2\nu_L \left.\frac{\partial u}{\partial r}\right|_{r=R} \tag{2.20}$$

Far from the bubble (for $r \to \infty$), the liquid is assumed to be at rest, so that $u(\infty,t) \to 0$ and also the time evolution of pressure at the boundary is given ($p(\infty,t) = p_\infty(t)$). Finally, substituting relation (2.20) into equation (2.17) and observing that:

$$\left.\frac{\partial u}{\partial r}\right|_{r=R} = -\frac{2\dot{R}}{R} \tag{2.21}$$

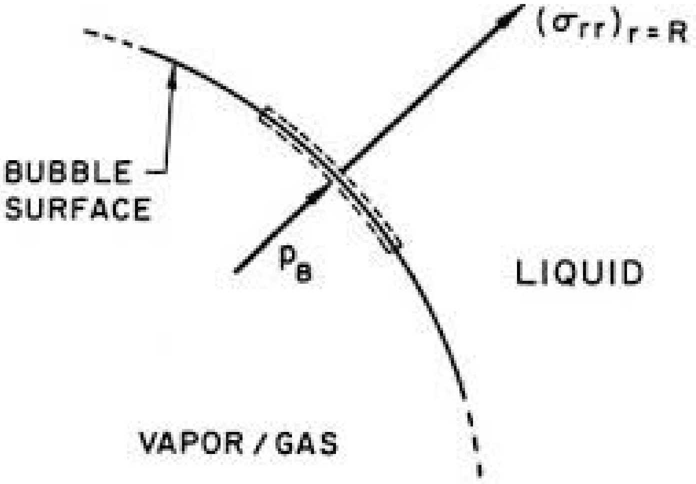

Figure 2.14 Picture showing the control volume taken into account to define the balance of the normal forces. Picture from Brennen [10]

We obtain the Rayleigh – Plesset equation in its classical form:

$$\frac{p_B(t) - p_\infty(t)}{\rho_L} = R\ddot{R} + \frac{3}{2}\dot{R}^2 + 4\nu_L\frac{\dot{R}}{R} + \frac{2}{\rho_L}\frac{\gamma}{R} \tag{2.22}$$

This equation allows to determine the temporal evolution of the bubble radius R and, consequently, the pressure field in all the liquid domain once the pressure boundary condition is given.

In case of inviscid fluid, the viscous term (that derives from boundary conditions introduced in equation (2.18)) vanishes, and a new equation, known simply as Rayleigh equation, remains.

2.5 Turbulence and the scales of turbulent motion

In fluid dynamics, *turbulence* or *turbulent flow* is a fluid motion phenomenon characterized by chaotic changes in pressure and velocity. This type of flow is specific for high velocity flows, which are very common in everyday engineering applications (two examples are shown in Figure 2.15a and 2.15b) and sets in opposition to *laminar flow*, which occurs when the fluid flows in well-ordered and parallel layers.

Another important aspect, which must be underlined concerning turbulence, is the fact that this phenomenon involves a wide range of scales: in fact, in turbulent flows, it is always possible to locate flow regions of different size where the fluid moves in a coherent way. These regions, called *eddies*, are characterized by a size ℓ (which also defines the scale of the single turbulent structure), a characteristic velocity $u(\ell)$ and a characteristic timescale $\tau(\ell) = \ell/u(\ell)$.

(a) Turbulence phenomena generated in the atmosphere by the wake of a Boeing 767. Picture from Cengel et al. [30]

(b) Two-dimensional image of an axisymmetric water jet obtained by the laser-induced fluorescence technique. Picture from Prasad et al. [54]

Figure 2.15 Examples of turbulent flows.

Despite the influence they have always exerted on many fields of application, turbulence phenomena are still a “young” and interesting field of research for scientists and engineers: indeed, the first theories and studies on turbulent flows appeared in 1922, when Richardson described the idea of *energy cascade* for the very first time. He introduced this principle through the use of the following short poetry:

“Big whorls have little whorls,
Which feed on their velocity;
And little whorls have lesser whorls,
And so on to viscosity”

Assumed that the kinetic energy enters the turbulence (through the production mechanism) at the largest scales of motion, Richardson’s concept of energy cascade implies that the large eddies, due to their instability, break up transferring their energy to eddies of smaller scales.

These smaller eddies are also unstable, so they follow a breakup process (similar to that occurred to the previous larger scales) which brings to a new transfer of energy from smaller eddies to even smaller ones. This mechanism, which really seems to work as a cascade, well explains how energy is transferred from larger to smaller scales of motion.

This process of inviscid energy transfer to successively smaller eddies, according to Richardson, lasts until smallest scales of motion have not been reached: once the energy coming from the largest scales of motion have entered the smallest ones, the eddy motion has stabilized and molecular viscosity effectively dissipates the kinetic energy.

The overall picture of the situation portrayed by Richardson is of great importance because he places dissipation at the end of a sequence of processes. Further investigations on Richardson's theory of energy cascade were conducted by Kolmogorov, who also proposed a way to estimate the size of the smallest scales of motion in 1941.

In the following section, Kolmogorov's theory and its hypothesis are explained in detail. Then, the Taylor microscales are briefly introduced as they play a crucial role in scale-resolving turbulence models such as Large Eddy Simulations. The author suggests referring to Pope [6] whether the reader was interested in deepening the arguments treated in this section.

2.5.1 Kolmogorov's Theory

Let us consider a fully developed turbulent flow at high Reynolds number characterized by the velocity $\mathcal{U}$ and lengthscale $\mathcal{L}$. The *rate of dissipation* ε is determined by the first transfer of the energy cascade, which occurs at the larger scales of the motion. These eddies are described by their length scale ℓ_0 (that is comparable to the flow caracteristic lengthscale $\mathcal{L}$) and by their characteristic velocity $u_0 = u(\ell_0)$ (which is on the same order of the turbulence intensity $u' = \sqrt{2/3k}$ and so comparable to the flow characteristic velocity $\mathcal{U}$). The Reynolds number associated to these scales $Re_0 = u_0\ell_0/\nu$ is comparable to the flow characteristic Reynolds number $Re_{\mathcal{L}} = \mathcal{U}\mathcal{L}/\nu$ (i.e. it is very large). So, the viscous effects on larger scales can be neglected.

These eddies have a kinetic energy of the order of u_0^2 and a timescale equal to $\tau_0 = \ell_0/u_0$, so the rate of transfer of energy can be assumed to scale as $u_0^2/\tau_0 = u_0^3/\ell_0$. This means that, for high Reynolds number values and intense turbulent flows, the *rate of dissipation* ε only scales as u_0^3/ℓ_0, independent of the viscosity. As said previously, in 1941 Kolmogorov presented his theory on turbulent flows and on energy cascades with the aim of also quantifying the characteristic scales of the smallest eddies responsible for the dissipation of energy. This theory bases on the fact that both the characteristic velocity $u(\ell)$ and the characteristic timescale $\tau(\ell)$ decrease if the lengthscale ℓ decreases and is defined bu the following three hypothesis:

a) Kolmogorov's hypothesis of local isotropy
b) Kolmogorov's first similarity hypothesis
c) Kolmogorov's second similarity hypothesis

In the next three paragraphs all the three Kolmogorov's hypothesis will be analysed in detail, one by one.

Kolmogorov’s hypothesis of local isotropy

At sufficiently high Reynolds number, the small-scale turbulent motions are statistically isotropic.

The first hypothesis made by Kolmogorov is about the isotropy of the smallest scales of the motion. Generally, the larger scales of the flow are anisotropic and influenced by the boundary conditions. According to Kolmogorov’s theory, the anisotropy of such scales finish to be lost in the chaotic scale-reduction specific of the energy cascade.

At this point, the introduction of a new length scale ℓ_{EI} (with $\ell_{EI} \sim 1/6\ell$) is necessary to set a demarcation between the anisotropic large turbulent structures ($\ell > \ell_{EI}$) and the isotropic small scales ($\ell < \ell_{EI}$).

Kolmogorov’s first similarity hypothesis

In every turbulent flow at sufficiently high Reynolds number, the statistics of the small-scale motions ($\ell < \ell_{EI}$) have a universal form that is uniquely determined by ν and ε.

After having made the assumption of local isotropy, Kolmogorov continued in the formulation of his theory stating that also all the information about the large eddies geometries (which depend once again on the mean flow and on the boundary conditions) are lost in the energy transfer to successively smaller and smaller eddies. Consequently, the statistics of the small-scale motions can be retained universal and similar in every high-Reynold-number turbulent flow.

To identify the parameters on which this universal state depends, we must think to the fact that inside the energy cascade, thus for $\ell < \ell_{EI}$, the main phenomena that occur are energy transfer and viscous dissipation. These two processes can be then well described assuming the rate at which the small scales receive energy from the large scales $\mathcal{T}_{EI}$ and the kinematic viscosity ν as the main parameters.

The range of sizes in which the energy cascade occurs following the first two Kolmogorov’s hypothesis, i.e. $\ell < \ell_{EI}$, from now on will be called *universal equilibrium range*. This definition is due to the fact that, in this range, the timescales $\tau(\ell) = \ell/u(\ell)$ are small compared to the timescale of the larger scales $\tau_0 = \ell_0/u_0$: so the small eddies with a size included in the range can quickly adapt to the possible changes in $\mathcal{T}_{EI}$, establishing a regime of dynamic equilibrium.

Given the two parameters ε and ν and assuming $\mathcal{T}_{EI} \sim \varepsilon$ (the energy-transfer rate nearly equals the dissipation rate at every scale within the universal equilibrium range), the Kolmogorov scales can be obtained as follows proceeding through dimensional analysis:

$$\eta = \left(\frac{\nu^3}{\varepsilon}\right)^{\frac{1}{4}} \tag{2.23}$$

$$u_\eta = (\varepsilon\nu)^{\frac{1}{4}} \tag{2.24}$$

$$\tau_\eta = \left(\frac{\nu}{\varepsilon}\right)^{\frac{1}{2}} \tag{2.25}$$

The fact that these three scales characterize the very smallest, dissipative eddies can be established through the following two quick demonstration:

- The Reynolds number based on the Kolmogorov scales is equal to unity. In fact:

$$Re_\eta = \frac{\eta u_\eta}{\nu} = 1 \tag{2.26}$$

Reynolds number equal to unity means that inertial forces are balanced by viscous forces, i.e. the energy that arrives to the eddies of scale η is suddenly and fully dissipated. This demonstrates that the process of energy transfer (which derives from the energy cascade assumption) continues until the scales of viscosity are reached.

- Combining all the three equations (2.23) (2.24) (2.25), the dissipation rate can be expressed as:

$$\varepsilon = \frac{\nu}{\tau_\eta^2} = \nu\left(\frac{u_\eta}{\eta}\right)^2 \tag{2.27}$$

From equation (2.27) the following relation can be derived:

$$\frac{u_\eta}{\eta} = \frac{1}{\tau_\eta} \tag{2.28}$$

Equation (2.28) provides a consistent characterization of the velocity gradients of the dissipative eddies [6].

The following ratios between the largest scales and Kolmogorov scales can be suddenly obtained considering equations (2.23 – 2.25) and assuming $\varepsilon \sim u_0^3/\ell_0$:

$$\frac{\eta}{\ell_0} \sim Re^{-3/4} \tag{2.29}$$

$$\frac{u_\eta}{u_0} \sim Re^{-1/4} \tag{2.30}$$

$$\frac{\tau_\eta}{\tau_0} \sim Re^{-1/2} \tag{2.31}$$

Kolmogorov's second similarity hypothesis

In every turbulent flow at sufficiently high Reynolds number, the statistics of the motions of scale ℓ *in the range* $\eta \ll \ell \ll \ell_0$ *have a universal form that is uniquely determined by* ε*, independent of* ν*.*

It is evident from equations (2.29), (2.30), and (2.31) that, for high values of the Reynolds number, the length scales, velocity scales and timescales associated to the dissipative eddies will be very small compared to those of the largest scales. Consequently, for high turbulence flows, there will be a wide range of nightscapes ℓ between the largest and the smallest scales (i.e. $\eta \ll \ell \ll \ell_0$) which can be considered at the same time as:

- much smaller than the largest scales ℓ_0
- much larger than the Kolmogorov scales η

Since eddies in this range are much bigger than the dissipative eddies, we can assume that their Reynolds number $\ell u(\ell)/\nu$ is large and so the effect of the viscosity on such scales is nearly negligible.

The new length scale ℓ_{DI} (with $\ell_{DI} \sim 60\eta$) is introduced, so that the range of lengthscales which was defined in the previous hypothesis can be written as $\ell_{EI} > \ell > \ell_{DI}$. This new lengthscale ℓ_{DI} splits the universal equilibrium range into two subranges: the *inertial subrange* ($\ell_{EI} > \ell > \ell_{DI}$) and the *dissipation range* ($\ell < \ell_{DI}$).

Inside the *inertial subrange,* the viscous effects are still negligible, so motions are still determined only by inertial effects. Inside the *dissipation range,* instead, the viscosity affects significantly the motions and induces energy dissipation phenomena.

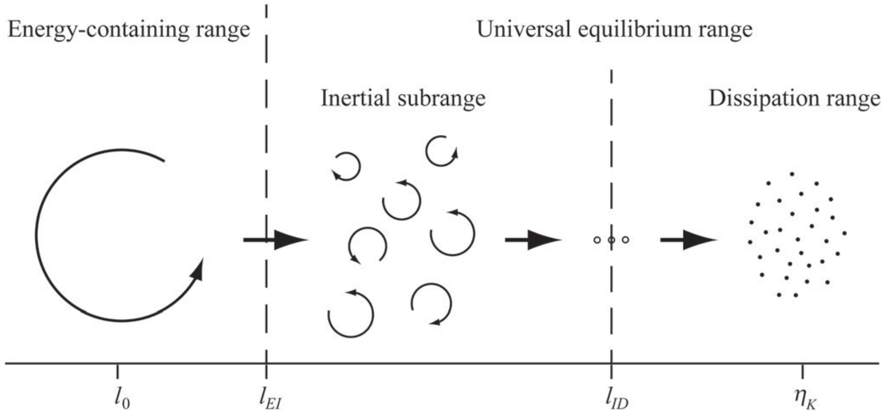

Figure 2.16 Schematic representation of the energy cascade turbulence model. Picture from Pope [6]

For $\ell > \ell_{EI}$, we have the *energy-containing range*, that is the range which includes the largest scales responsible for the transport of most of the flow energy. A scheme of all the ranges that take part to the turbulence energy cascade is shown in Figure 2.16.

Given the definition of the inertial subrange and of the dissipation range, it is now possible to better explain the meaning of the length scales ℓ_{DI} and ℓ_{EI}. In fact, the subscript EI indicates that ℓ_{EI} is the demarcation line between energy (E) and inertial (I) ranges, while the subscripts DI of ℓ_{DI} denotes the separation limit between the inertial subrange (I) and dissipation range (D).

Since no length scale, velocity scale or timescale can be obtained from ε alone, also the lengthscale ℓ of the eddies is taken into account. So, the velocity scale and timescale relative to eddies of size ℓ are determined as follows:

$$u(\ell) = (\varepsilon \ell)^{1/3} = u_\eta \left(\frac{\ell}{\eta}\right)^{1/3} \sim u_0 \left(\frac{\ell}{l_0}\right)^{1/3} \tag{2.32}$$

$$\tau(\ell) = \left(\frac{\ell^2}{\varepsilon}\right)^{1/3} = \tau_\eta \left(\frac{\ell}{\eta}\right)^{2/3} \sim \tau_0 \left(\frac{\ell}{l_0}\right)^{2/3} \tag{2.33}$$

From (2.32) and (2.33) derives that, due to their dependence on length scale ℓ, both velocity scale $u(\ell)$ and timescale $\tau(\ell)$ decrease as ℓ decreases. At this point, given the definitions of the scales associated to the eddies of size ℓ, another important step must be done to fully understand how the energy cascade works.

Let us consider $\mathcal{T}(\ell)$, which denotes the rate at which the energy is transferred from scales of size ℓ to smaller ones. If this transfer occurs for scales ℓ internal to the inertial subrange, $\mathcal{T}(\ell)$ is expected to be of the same order of $u(\ell)^2/\tau(\ell)$. Considering equations (2.32) and (2.33), the following identity can be obtained:

$$\frac{u(\ell)^2}{\tau(\ell)} = \varepsilon \tag{2.34}$$

Equation (2.34) demonstrates that inside the inertial range (i.e. for $\ell_{EI} > \ell > \ell_{DI}$) the rate of energy transfer $\mathcal{T}(\ell)$ does not depend on the eddy scale ℓ and, furthermore, it is equal to ε. Therefore, within the inertial subrange we have:

$$\mathcal{T}_{EI} \equiv \mathcal{T}(\ell_{EI}) = \mathcal{T}(\ell) = \mathcal{T}_{DI} \equiv \mathcal{T}(\ell_{DI}) = \varepsilon \tag{2.35}$$

The equality chain stated by relation (2.35) is explicative of the mechanism of energy transfer from the largest to the dissipative scales: the rate of energy transfer from the large scales $\mathcal{T}_{EI}$ sets the constant rate at which the energy transfer $\mathcal{T}(\ell)$ occurs inside the inertial range. When the lower limit of the inertial subrange is reached, energy leaves this range at the same rate $\mathcal{T}_{DI}$ and enters the dissipation range. Here, the rate of energy transfer equals the rate of dissipation ε.

A schematic picture of the energy cascade phenomenon occurring in turbulent flows is shown in Figure 2.17.

2.5.2 The Taylor microscale

The Taylor microscale, usually denoted with the symbol λ, is another important lengthscale often used in fluid dynamics and CFD simulations to characterize turbulent flows. Introduced for the first time by Taylor in 1935, it has the paramount characteristic of being intermediate in size between the Kolmogorov length scale η and the characteristic scale of the flow $\mathcal{L}$, laying inside the inertial subrange.

In general, the Taylor microscale has not a precise physical meaning, but the most popular interpretation states that, for high Reynolds number flows, it can be defined as the largest scale at which the viscosity begins to affect the motions. Hence, following this definition, Taylor microscale could also be considered as the lower limit of the inertial range or the largest of the dissipative scales too. Large Eddy Simulations (and scale-resolving turbulence models in general) require severe mesh conditions in order to apply their models, which relies on the hypothesis of universality and isotropy of turbulent small scales.

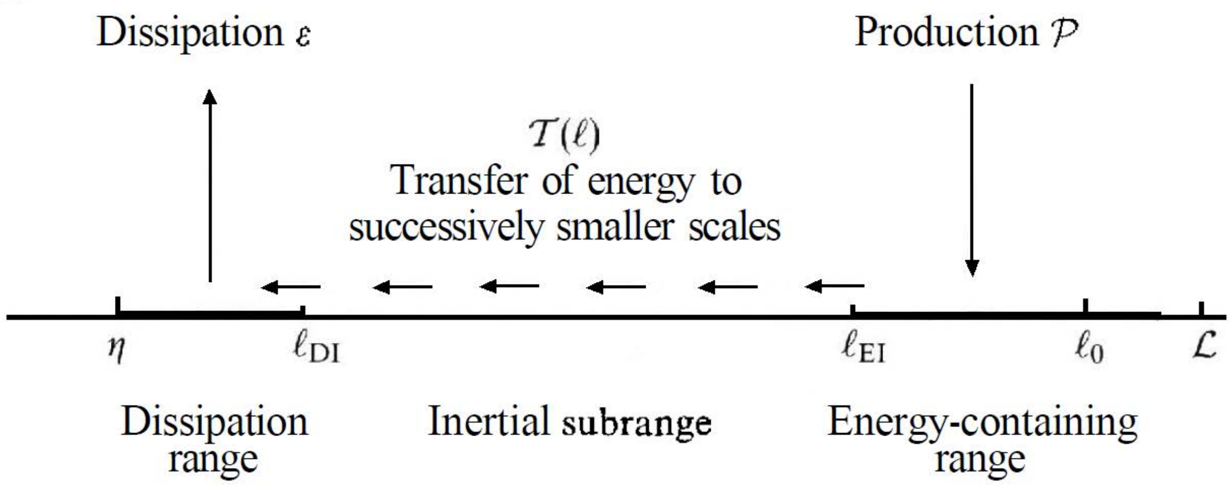

Figure 2.17 Picture of the energy cascade turbulence model. The energy transfer from energy-containing range to the dissipation range is shown. Picture from Pope [6]

These hypotheses, according to the Kolmogorov theory, are valid only inside the inertial subrange: therefore, implicit LES meshes must be set-up so that in every grid cell the size is included in the inertial range.

So, due to the fact that the Taylor microscale effectively describes a scale internal to the inertial subrange, this scale results to be a very useful reference when there is the necessity of estimate the grid-cell size for a LES.

In literature, several possible useful formulations to evaluate the Taylor microscale λ are available. Next, the simple formulation by Pope [6] is taken into account:

$$\frac{\lambda}{\mathcal{L}} = \sqrt{10} {Re_{\mathcal{L}}}^{-1/2} \tag{2.36}$$

Where $\mathcal{L}$ is the characteristic size associated to the flow and $Re_{\mathcal{L}}$ is the caracteristic Reynolds number of the flow.Furthermore, combining equations (2.29) (that derives from the Kolmogorov theory by considering $\mathcal{L}$ instead of ℓ_0) and (2.36), it is also possible to describe the Taylor microscale as a function of the smallest dissipative scale η:

$$\lambda = \sqrt{10}\eta^{2/3}\mathcal{L}^{1/3} \tag{2.37}$$

Equations (2.36) and (2.37) also confirm the fact that the Taylor microscale is an intermediate size between the largest scale of the flow (which are of the order of $\mathcal{L}$) and the dissipative scale (identified by the Kolmogorov lengthscale η).

Chapter 3

Model and Implementation

This chapter has the aim of describing the models and solvers applied in this Master Thesis. All the simulations were run using *STAR CCM+*, which is one of the most popular CFD software. Initially developed by *CD-Adapco*, nowadays its property belongs to *Siemens*.

STAR CCM+, which is the acronym of ***S**imulation of **T**urbulent flow in **A**rbitrary **R**egions – **C**omputational **C**ontinuum **M**echanics*, is a CFD software based on the *Finite Volume Method* for the solution of the Navier-Stokes equations.

This presentation, after a brief description of the governing equations, follows the workflow expected by *STAR CCM+* when a new simulation is set up.

3.1 The governing equations

In fluid mechanics, the physics is, in general, ruled by governing equations based on mass and momentum conservation principles. In this paragraph they are briefly presented and described omitting their full theorical derivation. The reader can find solid references examining works made by Kundu et al. [29], Cengel et al. [30], Perić et al. [31], and Moukalled et al. [32].

All these authors obtained the general equations of the fluid dynamics starting from the Reynolds' transport theorem, that provides a link between control mass systems (CM) and control volume systems (CV). Indicating with ψ any intensive property (that could be density, velocity, energy…), the general form of the Reynolds' transport theorem is:

$$\frac{d}{dt}\int_{\mathrm{V}_{CM}} \rho\psi \, dV = \frac{d}{dt}\int_{V_{CV}} \rho\psi \, d\mathrm{V} + \int_{\mathrm{S}_{CV}} \rho\psi(\boldsymbol{u} - \boldsymbol{u_b}) \cdot \boldsymbol{n} \, dS \tag{3.1}$$

where V_{CM} is the volume of the mass control system, V_{CV} and S_{CV} are respectively the volume and the surface of the control volume system, $\boldsymbol{n}$ is the outpointing normal vector, $\boldsymbol{u}$ is the fluid velocity vector and $\boldsymbol{u_b}$ is the velocity of the control volume.

Considering a static control volume system ($\boldsymbol{u_b} = \boldsymbol{0}$) and imposing $\psi = 1$ in equation (3.1), it is possible to obtain the continuity equation (also called mass conservation equation) in its integral form:

$$\frac{d}{dt}\int_V \rho d\mathrm{V} + \int_S \rho \boldsymbol{u} \cdot \boldsymbol{n}\, dS = 0 \tag{3.2}$$

Using the Gauss' theorem with the assumption of infinitely small control volume, the differential form for the continuity equation can be derived:

$$\frac{\partial \rho}{\partial t} + \nabla \cdot (\rho \boldsymbol{u}) = 0 \tag{3.3}$$

Also the momentum conservation equation is derived using the Reynolds' transport theorem (imposing $\psi = u$ into equation (3.1)**)** starting from Newton's second law. With the aim of taking into account the shear stresses which act on the control volume surface, the assumption of Newtonian fluid is usually made, and the following integral form of the momentum conservation equation is achieved:

$$\frac{d}{dt}\int_V \rho \boldsymbol{u}\, d\mathrm{V} + \int_S \rho \boldsymbol{u}\boldsymbol{u} \cdot \boldsymbol{n}\, dS = \int_S \boldsymbol{\mathcal{T}} \cdot \boldsymbol{n} dS + \int_V \rho \boldsymbol{b}\, dV \tag{3.4}$$

Where $\boldsymbol{b}$ is the vector of the body forces (such as gravity force) and $\boldsymbol{\mathcal{T}}$ is the stress tensor. With the assumption of Newtonian fluid, this tensor takes the following form:

$$\boldsymbol{\mathcal{T}} = -\left(p + \frac{2}{3}\mu \nabla \cdot \boldsymbol{u}\right)\mathbb{I} + 2\mu\left(\frac{1}{2}[\nabla \boldsymbol{u} + (\nabla \boldsymbol{u})^T]\right) = -p\mathbb{I} + \boldsymbol{\mathcal{E}} \tag{3.5}$$

Where $\mathbb{I}$ is the identity tensor, while $\boldsymbol{\mathcal{E}}$ is the viscous tensor:

$$\boldsymbol{\mathcal{E}} = -\left(\frac{2}{3}\mu \nabla \cdot \boldsymbol{u}\right)\mathbb{I} + 2\mu\left(\frac{1}{2}[\nabla \boldsymbol{u} + (\nabla \boldsymbol{u})^T]\right) \tag{3.6}$$

Again, applying the Gauss' theorem to the surface integrals of the equation (3.4), we can obtain the momentum conservation in its differential form:

$$\frac{\partial(\rho\boldsymbol{u})}{\partial t} + \nabla\cdot(\rho\boldsymbol{u}\boldsymbol{u}) = -\nabla\mathrm{p} + \nabla\cdot\boldsymbol{\mathcal{E}} + \rho\boldsymbol{b} \tag{3.7}$$

Assuming gravity as only body force, equations (3.3) and (3.7) can be written using Einstein's notation as follows:

$$\frac{\partial\rho}{\partial t} + \frac{\partial(\rho u_i)}{\partial x_i} = 0 \tag{3.8}$$

$$\frac{\partial(\rho u_i)}{\partial t} + \frac{\partial\left(\rho u_i u_j\right)}{\partial x_j} = -\frac{\partial p}{\partial x_i} + \frac{\partial e_{ij}}{\partial x_j} + \rho g_i \tag{3.9}$$

Equations (3.2) and (3.4) are usually discretized and solved by CFD software (as *STAR CCM+*) using the *Finite Volume method*. This method operates dividing the domain in smaller control volumes through the creation of a suitable grid, also called *mesh*.

For every small control volume, the centroid is the computational node, namely the point where all the cell properties and physical quantities are defined.

The conservation equations must be valid not only for the whole domain, but also for every single small cell.

For the *Finite Volume method*, one of the most important critical points is the determination of the fluxes through the surfaces of each small element.

The net flux through the entire surface of an arbitrary small element is equal to the sum of the fluxes through every single face that forms the cell surface:

$$\int_S f\,dS = \sum_k \int_{S_k} f\,dS \tag{3.10}$$

where f is the component of convective or diffusive flux normal to the reference face. Unfortunately, this quantity f is unknown for every single face S_k of an element.

In fact, for every cell, properties and physical quantities are defined only at the centroid, while, for computing surface integrals, these should be defined at each surface of every cell.

Thus, there is the need to approximate or interpolate the solution between two consecutive cells. Only in this way it is possible to compute fluxes later on and solve conservation equations.

Luckily, literature provides various method to approximate and compute the value of f for each face and, as always, each one of these solutions is more appropriate than others according to computational costs, solidity of the algorithm and degree of approximation.

In this work, the *bounded-central differencing convection scheme* is adopted since its usage is recommended by the User Guide [28] of Star CCM+ for Large Eddy Simulations (LES) of complex turbulent flows. In fact, as we will appreciate following this explanation, this scheme seems to be a mixture of other schemes and aims to take advantage of their strengths.

Convective flux in bounded-central differencing is computed following the next scheme:

$$(\dot{m}\phi)_f = \begin{cases} \dot{m}\phi_{FOU} & \text{for } \xi < 0 \ or \ \xi > 1 \\ \dot{m}(\sigma\phi_{CD} + (1-\sigma)\phi_{SOU} & \text{for } 0 \le \xi \le 1 \end{cases} \tag{3.11}$$

where:

ϕ_{FOU}: Cell-face center value obtained through first-order upwind interpolation

ϕ_{SOU}: Cell-face center value obtained through second-order upwind interpolation

ϕ_{CD}: Cell-face center value obtained through central-differencing interpolation

ξ: Normalized-Variable Diagram (NVD) value that is computed based on local conditions

The variable σ is function of ξ ($\sigma = \sigma(\xi)$) and satisfies the following two conditions:

$$\begin{cases} \sigma(0) = 0 \\ \sigma(\xi) = 1 \quad \text{for } \xi \ge \xi_{ubf} \end{cases} \tag{3.12}$$

where ξ_{ubf} is called *upwind blending factor*. Its value ensures a proper balance between accuracy (given by a formally second-order accurate scheme when the boundedness criterion is satisfied) and robustness (given by the first order-upwind scheme).

In general, setting higher values of the upwind blending factor helps in obtaining more stable solutions. It is also worth mentioned that, in certain cases (for example, when the mesh is coarse), this scheme could be more dissipative than the simple central-differencing one.

In the end, this scheme provides a good compromise between solidity and accuracy, and this property is very useful when the user has to simulate complex turbulent flows.

As regards the integration over a volume, given a generic function q, the simplest second-order accurate approximation consists in replacing the volume integral with the product of the mean value of the integrand function with the volume of the Control Volume element, approximating the former with the value at the Control Volume center q_P:

$$Q_P = \int_V qdV = \bar{q}V \sim q_P V \tag{3.13}$$

This solution is really simple: indeed, no interpolation is needed because the information is already available at the central node.

Since the *Finite Volume Method* and CFD implementation of fluid dynamics equation are not central topics for the present work, the author suggests to refer to Perić et al. [31], Moukalled et al. [32] and to the User Guide [29] to deepen the topics explained in this paragraph.

3.2 The Segregated Flow Solver

In *STAR CCM+* the VOF model is available only when the *Segregated Flow solver* is selected, so in this paragraph, the attention will be focused on this method, leaving aside the other approach provided by the software, i.e. the *Coupled Flow solver*.

The *Segregated Flow solver* is a computational approach that solves the equations of fluid dynamics in a sequential manner, one after the other. It employs a pressure-velocity coupling algorithm where the continuity equation is treated as a velocity field constraint and fulfilled after having solved a pressure-correction equation. This technique of solving conservation equations is suitable for incompressible flows, though it can also handle mildly compressible flows.

In *STAR CCM+*, when the *Segregated Flow solver* is selected, the user can then choose between two algorithms: SIMPLE (***S**emi-**I**mplicit **M**ethod for **P**ressure **L**inked **E**quations*) and PISO (***P**ressure-**I**mplicit with **S**plitting of **O**perators*). Since the SIMPLE algorithm is the only algorithm that is compatible with VOF model use, this algorithm was used in all the simulations of this project.

It is worth mentioned that Perić [31], in his book, underlines how complex is solving the Navier-Stokes equations and computing the three velocity components and the pressure field. This complexity is due to the lack of an independent equation for the pressure: in fact, in the momentum conservation equation (3.7), pressure appears only in form of pressure gradient.

Instead, the continuity equation (3.3) works more like a velocity field constraint than a dynamic equation. With the purpose of overcome these issues, a lot of modern algorithms were studied: the most popular approaches work with the idea of constructing the pressure field to guarantee satisfaction of the continuity equation.

In this kind of algorithms, both velocity and pressure are modelled as the sum of a guessed term and a correction term, as follows:

$$\mathbf{v} = \mathbf{v}^* + \mathbf{v}' \tag{3.14}$$

$$p = p^* + p' \tag{3.15}$$

where $\mathbf{v}^*$ and p^* are respectively the velocity and pressure guessed terms and $\mathbf{v}'$ and p' are the corrections. To reach convergence, all this procedure must produce velocity and pressure fields in agreement with equations (3.2) and (3.4).

The pressure-velocity coupling equation is obtained from the discretized continuity equation, that is also re-written in terms of mass flux considering guessed and correction terms:

$$\sum_f \dot{m}_f = \sum_f \left(\dot{m}_f{}^* + \dot{m}_f{}'\right) = 0 \tag{3.16}$$

The uncorrected face mass flux is computed after the discrete momentum equations have been solved. These equations are solved counting on a guessed pressure field p^* that could also not satisfy continuity equation initially. Mass flux correction $\dot{m}_f{}'$ is necessary to fullfill mass conservation.

The uncorrected mass flux at the interior face between two cells can be computed as follows:

$$\dot{m}_f{}^* = \rho_f \left(\frac{\mathbf{v}_0{}^* + \mathbf{v}_1{}^*}{2}\right) \cdot \boldsymbol{n} S_f - \mathcal{Y}_f \tag{3.17}$$

Where $\mathbf{v}_0{}^*$ and $\mathbf{v}_1{}^*$ are cell-0 and cell-1 velocities after the discrete momentum equations have been solved. The linear interpolation between two adjacent cells is not the best method to approximate the face physical quantities and could bring to unphysical values for pressure. To prevent this problem, the *Rhie-and-Chow dissipation* $\mathcal{Y}_f$ is introduced:

$$\mathcal{Y}_f = Q_f\left(p_1 - p_0 - \overline{\nabla p_f^*} \cdot \boldsymbol{n} dS\right) \tag{3.18}$$

With the coefficient of dissipation Q_f defined as follows:

$$Q_f = \rho_f \left(\frac{V_0 + V_1}{\bar{a}_0 + \bar{a}_1}\right) \boldsymbol{\alpha} \cdot \boldsymbol{n} S_f \tag{3.19}$$

Where:

- V_0 and V_1 are the volume of cell-0 and cell-1 respectively
- $\bar{a}_0$ and $\bar{a}_1$ are the average of momentum coefficients for all components of momentum for cell-0 and cell-1
- p_1 and p_0 are the cell center pressure value of the two involved cells, computed at the end of the previous iteration
- $\overline{\nabla p_f^*}$ is the volume-weighted average of the cell gradients of pressure, computed using a volume-based interpolation between the gradient values of the two cells

It must be underlined the fact that, if the flow is compressible, also a density correction is needed. Therefore, for the general case of compressible flow, the following expression is valid:

$$\dot{m}_f = (\rho + \rho')_f\left(\mathrm{v}_{fn}{}^* + \mathrm{v}_{fn}{}'\right) S_f = \left(\rho_f \mathrm{v}_{fn}{}^* + \rho_f{}' \mathrm{v}_{fn}{}^* + \rho_f \mathrm{v}_{fn}{}' + \rho_f{}' \mathrm{v}_{fn}{}'\right) S_f \tag{3.19}$$

Where the subscript “fn” stands for “face-normal” component. The third term of expression (3.19) can then be computed with the following relation:

$$\rho_f \mathrm{v}_{fn}{}' S_f = -Q_f(p_1{}' - p_0{}') \tag{3.20}$$

Where $p_1{}'$ and $p_0{}'$ are the cell pressure corrections. Instead, the second term of expression (3.19) can be derived with the following relation:

$$\rho_f{}' \mathrm{v}_{fn}{}^* S_f = \frac{\dot{m}_f{}^*}{\rho_f}\left(\frac{\partial \rho}{\partial p}\right)_T p'_{upwind} \tag{3.21}$$

Where p'_{upwind} can be found using a standard first-order upwind interpolation:

$$p'_{upwind} = \begin{cases} {p_0}' & \text{for } {\dot{m}_f}^* > 0 \\ \\ {p_1}' & \text{for } {\dot{m}_f}^* < 0 \end{cases} \tag{3.22}$$

The face mass flux correction is then found by combining the terms of equations (3.20) and (3.21):

$${\dot{m}_f}' = Q_f({p_0}' - {p_1}') + \frac{{\dot{m}_f}^*}{\rho_f}\left(\frac{\partial \rho}{\partial p}\right)_T p'_{upwind} \tag{3.23}$$

The discrete pressure correction equation is obtained from equation (3.16) and (3.23) and could be written in coefficient form as:

$$p'_p + \sum_n a_n p'_n = r \tag{3.24}$$

Where r represents the net mass flow into the cell:

$$r = \sum_f {\dot{m}_f}^* \tag{3.25}$$

The result of equation (3.25) is equivalent to the continuity residual and this value is shown by *STAR CCM+* with the other residuals monitors and it is very useful in checking continuity convergence.

3.2.1 The SIMPLE Algorithm

In the following paragraph, a brief explanation of the SIMPLE algorithm is given, based on the work done by Peric et al. [31] and on the User Guide [29].

The SIMPLE algorithm, that belongs to the Implicit Pressure-Correction algorithms family, was formulated for the first time by Spalding and Patankar [41] in 1972.

A simplified flowchart (extract from the User Guide) is next reported to get a better idea of how this algorithm works in case of incompressible flows (density correction is not treated in the following flowchart):

1. Guess an initial pressure field p^*

2. Solve the momentum equation (3.4) using the guessed pressure field to compute the intermediate velocity field $\mathbf{v}^*$
3. Compute the uncorrected face mass fluxes $\dot{m}_f{}^*$ (3.17)
4. Solve the equation (3.24) to obtain the pressure correction values p'
5. Update the pressure field considering the under-relaxation factor for pressure ω:

$$p^{m+1} = p^m + \omega p' \tag{3.26}$$

6. Correct the face mass fluxes:

$$\dot{m}_f{}^{m+1} = \dot{m}_f{}^* + \dot{m}_f{}' \tag{3.27}$$

7. Correct the cell velocities with the velocity correction equation:

$$\mathbf{v}^{m+1} = \mathbf{v}^* - \frac{V \nabla p'}{\mathbf{a}'^{\mathbf{v}}_p} \tag{3.28}$$

   Where $\nabla p'$ is the gradient of the pressure corrections, $\mathbf{a}'^{\mathbf{v}}_p$ is the vector of central coefficients for the discretized velocity equation and V is the cell volume.
8. Repeat step 2 – 7 until convergence.

3.3 The Volume of Fluid (VOF) Method

The *Volume of Fluid* (*VOF*) *model* is a multi-phase interface-capturing method suitable for predicting the distribution and movement of the interface between two or more immiscible fluids.

This model is based on the hypothesis that all the immiscible fluids present in the same control volume share the same physical quantities (velocity, pressure, temperature).

Following this assumption, the same set of basic governing equations (mass, momentum and, if necessary, energy conservation) valid for a single-phase flow is solved for an equivalent fluid whose properties are computed as weighted averages of the properties of every single phase involved.

The function which acts as weight is the *Volume of Fraction*, that can be computed for every single phase as follows:

$$\alpha_i = \frac{V_i}{V} \tag{3.29}$$

Where α_i is the volume fraction of the i-th phase, V_i is the volume of the control volume occupied by the i-th phase and V is the total volume of the control volume element.

It is clear that, for every single control volume element, it must be:

$$\sum_{i=1}^{N} \alpha_i = 1 \tag{3.30}$$

Where N is the number of phases involved in the multi-phase flow.

Once all volume fractions are known, the properties of the equivalent single-phase fluid (such as density and dynamic viscosity) can be computed as follows:

$$\rho = \sum_{i=1}^{N} \alpha_i \, \rho_i \tag{3.31}$$

$$\mu = \sum_{i=1}^{N} \alpha_i \, \mu_i \tag{3.32}$$

Where ρ_i and μ_i are respectively density and dynamic viscosity of the i-th phase.

Being the volume fractions unknown, it is necessary to find one additional equation for each phase (in addition to the continuity and momentum equations) to close the problem. This equation is the *Volume Fraction Transport Equation*, that rules the distribution of the i-th phase and has the following form:

$$\begin{aligned} &\frac{\partial}{\partial t}\int_V \alpha_i dV + \oint_S \alpha_i \, \boldsymbol{u} \cdot \boldsymbol{n} \, dS = \\ &= \int_V \left(S_{\alpha_i} - \frac{\alpha_i}{\rho_i}\frac{D\rho_i}{Dt}\right) dV - \int_V \frac{1}{\rho_i} \nabla \cdot (\alpha_i \rho_i \boldsymbol{u}_{d,i}) dV \end{aligned} \tag{3.33}$$

Where $\boldsymbol{u}$ is the mixture (mass-averaged) velocity, $\boldsymbol{u}_{d,i}$ is the diffusion velocity of the i-th phase, S_{α_i} is a user-defined source term for the i-th phase and $\frac{D\rho_i}{Dt}$ is the material derivative of the density of the i-th phase.

The diffusion velocity term is non-zero only in case of slip between the phases. In our simulations, the *no slip model* was adopted, so this term can be neglected.

Furthermore, treating both phases as incompressible fluids, the term of equation (3.33) that presents the material derivative of the i-th phase density vanishes.

Next, the other general conservation equations valid with the *VOF method* are shown.

Mass Conservation Equation:

$$\frac{\partial}{\partial t}\int_V \rho dV + \oint_S \rho \boldsymbol{u} \cdot \boldsymbol{n} dS = \int_V S\, dV \tag{3.34}$$

Where S is the total source term given by:

$$S = \sum_{\boldsymbol{i=1}}^{\boldsymbol{N}} \rho_i S_{\alpha_i} \tag{3.35}$$

Momentum Conservation Equation:

$$\begin{aligned} &\frac{\partial}{\partial t}\int_V \rho \boldsymbol{u}\, dV + \oint_S \rho \boldsymbol{u} \times \boldsymbol{u} \cdot \boldsymbol{n} dS = \\ &= \oint_S p\mathbb{I} \cdot \boldsymbol{n} dS + \oint_S \boldsymbol{\mathcal{T}} \cdot \boldsymbol{n} dS + \int_V \boldsymbol{b}\, dV - \sum_{i=1}^{N} \oint_S \alpha_i \rho_i \boldsymbol{u}_{d,i} \times \boldsymbol{u}_{d,i} \cdot \boldsymbol{n} dS \end{aligned} \tag{3.36}$$

Where $\mathbb{I}$ is the identity tensor, $\boldsymbol{\mathcal{T}}$ is the stress tensor and $\boldsymbol{b}$ is the vector of body forces.

3.4 The Cavitation Model

For being solved, the equation (3.34) and (3.36) need the knowledge of the source term, that is responsible of the phase change due to cavitation and depends on the choice of the cavitation model.

STAR CCM+ provides three different cavitation models: the *Full Rayleigh-Plesset model*, the *Schnerr-Sauer model* and the *Homogeneous Relaxation model*. The main difference between these three approaches is based on how they model the bubble growth rate.

The *Full Rayleigh-Plesset model* is ruled by the same equations presented in the *Theory* section.

The *Schnerr-Sauer* model is a simplification of the *Full Rayleigh-Plesset model*: in fact, this model ignores three terms of equation (2.22), respectively the bubble growth acceleration term, the viscous term and the term that is responsible of the surface tension effects [35].

The *Homogeneous Relaxation model* is based on a finite rate equation with an empirical time scale formulation. It is also worth mentioned that, for this project, the User Guide does not recommend to adopt this approach because it is suitable for modelling phenomena which occur in thermal non-equilibrium, such as flash boiling [29].

In this project, basing on the work made by Zambon [13], only the *Schnerr-Sauer model* was considered. This assumption is also strengthened by the fact that Brennen [10], in his work, reports that in engineering application, results obtained considering the *Schnerr-Sauer model* are, in most cases, comparable with those obtained using *Full Rayleigh-Plesset model*.

All the cavitation models provided by *STAR CCM+* are homogeneous seed-based approach, i.e. a certain quantity of impurities and bubbles is already accounted into the liquid.

These are called *seeds* by the software and they act as nucleation sights of the cavitation phenomenon. This kind of models is based on the following assumptions:

- Seeds are spherical and uniformly distributed in the liquid, as characterized by the *number of seeds per unit volume of liquid* n_0, also called *seed density*
- All the seeds, at the beginning, are spherical and have the same radius R_0 (*seed radius*), that is also the smallest radius admitted for bubbles during the simulation
- The number of seeds in a control volume N is proportional to the amount of liquid. Thus, there is no necessity of following and tracking every single particle in its motion

Both two parameters n_0 and R_0 must be defined by the user. Despite this, both *seed density* and *seed radius* do not have physical meaning and they must be chosen proceeding by trial and error until good agreement with experimental data is not reached. In the end, the model must be tuned-up.

Fortunately, Literature provides some guidelines on recommended values, though they refer to cases which main phase is diesel fuel. Next, Table 3.1 reports these recommended values.

	n_0 **[1/m^3]**	R_0 **[m]**	α_0
Recommended Values	$10^{12} – 10^{14}$	$3 \cdot 10^{-7} – 2 \cdot 10^{-6}$	$5 \cdot 10^{-6} – 5 \cdot 10^{-5}$

Table 3.1 Recommended values for the initial parameters of the cavitation model suggested by Giannadakis [42]

It was taken from the PhD thesis by Giannadakis [42] and used by Andersen [12] and Zambon [13] in their Master Thesis works. Good references can also be found in work made by Yuan et al. [38].

The analysis lead by these Authors has shown that the nuclei concentration for water must be at least of the order of 10^{14} nuclei/m^3 to establish satisfying agreement with experiments. Thus, following the previous hypothesis, the amount of seeds in an arbitrary control volume are:

$$N = n_0 \alpha_L V \tag{3.37}$$

Where α_L is the liquid volume fraction. The total volume of vapor, assuming spherical bubbles, is:

$$V_V = N\left(\frac{4}{3}\pi R^3\right) \tag{3.38}$$

And the vapor fraction is:

$$\alpha_V = \frac{V_V}{V} = n_0 \alpha_L \left(\frac{4}{3}\pi R^3\right) V_V = N\left(\frac{4}{3}\pi R^3\right) \tag{3.39}$$

Knowing vapor and liquid fraction, it is possible to compute bubble radius:

$$R = \sqrt[3]{\frac{3\alpha_V}{4\pi n_0 \alpha_L}} \tag{3.40}$$

Now that the model background is completely available, let us proceed explaining how the source term is modelled. Let us consider a bubble moving in the flow.

Therefore, the rate at which the vapor quantity increase/decrease at an arbitrary time instant is approximately equal to the rate of change of the volume of the bubble content in the control volume. The rate of change in volume for a single bubble can be computed as follows:

$$\frac{dV_V}{dt} = 4\pi R^2 \frac{dR}{dt} \tag{3.41}$$

Consequently, the mass transfer rate per unit of volume (that is equal to the source term in equation (3.34)) is:

$$\dot{m} = \rho_V \frac{dV_V}{dt}\frac{1}{V} = \rho_V \frac{d}{dt}\left(\frac{4}{3}N\pi R^3\right)\frac{1}{V} = 4n_0\alpha_L\rho_V\pi R^2\frac{dR}{dt} \tag{3.42}$$

This is the point at which the cavitation model is set in, computing the bubble growth rate $\frac{dR}{dt}$ basing on the assumptions that have been made. The *Schnerr-Sauer model* estimates this growth rate starting from the *Rayleigh-Plesset model* equation (2.22) ignoring bubble growth acceleration, viscous term and the surface tension effects:

$$\left(\frac{dR}{dt}\right)^2 = \frac{2}{3}\left(\frac{p_{sat} - p_\infty}{\rho_L}\right) \tag{3.43}$$

When the surrounding pressure p_∞ is lower than the saturation pressure of the bubble, the bubble growth rate is positive and the bubble grows:

$$\frac{dR}{dt} = \sqrt{\frac{2}{3}\left(\frac{p_{sat} - p_\infty}{\rho_L}\right)} \tag{3.44}$$

On the contrary, when the pressure external to the bubble is larger than the saturation pressure, the bubble decreases its radius, experiencing a negative growth rate:

$$\frac{dR}{dt} = -\sqrt{\frac{2}{3}\left(\frac{p_\infty - p_{sat}}{\rho_L}\right)} \tag{3.45}$$

In general, the following expression is valid:

$$\frac{dR}{dt} = sign(p_{sat} - p_\infty)\sqrt{\frac{2}{3}\left(\frac{|p_{sat} - p_\infty|}{\rho_L}\right)} \tag{3.46}$$

Substituting (3.46) in (3.42), we obtain the definitive expression used by the *Schnerr-Sauer model* to estimate the source term of equation (3.34):

$$S_V = \dot{m} = 4n_0\alpha_L\rho_V\pi R^2\, sign(p_{sat} - p_\infty)\sqrt{\frac{2}{3}\left(\frac{|p_{sat} - p_\infty|}{\rho_L}\right)} \tag{3.47}$$

3.5 The Turbulence Model

So far, no mention has been made on how turbulence problem was treated in this analysis. As we will see further on, in all the simulations that were made, the Reynolds number was always larger than 2000 (laminar limit for pipe flows), reaching value of the order of magnitude of 10^5. This condition states that the nozzle flow is turbulent and so turbulence effects must be taken into account. To model the turbulence phenomena, the *Large Eddy Simulation (LES) model* was chosen.

Describing in detail LES turbulence model is not the real purpose of this Thesis. Despite this, a quick description of the model is given in the following paragraph. The author suggests referring to Sagaut [4], John [5], and Pope [6] for a more detailed analysis, mainly focusing on incompressible flows.

The *Large Eddy Simulation (LES)* is a mathematical approach for solving the CFD equations of turbulence that has the aim of resolving the largest scales (*eddies*) of motion, while ignoring the smallest ones (which transport less flow information and are the most expensive from the computational point of view).

This technique, that is made possible by low-pass filtering the Navier-Stokes equations, really removes the effects of smallest scales from the numerical solutions. However, the information of the scales that are cut-off by the filtering operations are not irrelevant and they must be modelled.

Of course, this method, with its characteristics, is less expensive than the more accurate DNS approach (*Direct Numerical Simulation*) which directly solves the Navier-Stokes equations up to the smallest scales of motion, typical of viscous dissipation and represented by the Kolmogorov's length scale η.

On the other hand, Large Eddy Simulations are more expensive, but also way more accurate than RANS simulations (*Reynolds Averaged Navier-Stokes*), that directly solves the averaged equations of fluid dynamics using models which can have relevant impact on the solution and could also be not so "universal" (every RANS model has a lot of calibration constants and it must be tuned-up according to the case).

Being the turbulence a three dimensional and unsteady problem, even a simulation that involves LES turbulence modelling must consider three dimensional geometry and non-stationary flow: this means that, also in case of symmetrical geometries, the LES approach does not permit to take advantages of the problem symmetries and requires an even larger number of cells as the Reynolds number grows.

As told previously, the LES technique is based on filtering operations, in particular low-pass filtering operations. To better understand the nature of this kind of mathematical operations, let us consider a generic velocity component $u_j(x,t)$, function of time and position. Given the filtering operator G_Δ, the correspondant filtered velocity component $\tilde{u}_j(x,t)$ is, in general, given by the following mathematical definition:

$$\tilde{u}_j(x,t) = G[u_j] = \int u_j(x-r,t)\, G_\Delta(r,t)\, dr \qquad (3.48)$$

Where Δ is the characteristic size of the filter, i.e. the reference length under which the filter cuts-off the fluctuations, x is the position in which filtered quantities must be computed and r is the distance from that point. In literature a lot of different filtering operators are available, such as Gaussian filter and box filter. Further details are available in references [4], [5] and [6] as said previously.

When Δ is explicitly defined by the user, the filtering operation is also called *explicit filtering approach*. In *STAR CCM+*, instead, the characteristic dimension of the filter is defined implicitly by the size of every single grid element that forms the mesh. This filtering method is also named *implicit filtering approach* and has the major benefit of taking full advantage of the mesh geometry.

It is important to underline that to obtain good results performing a LES, the filtering size Δ must be chosen so that it lays inside the *inertial range* of turbulence. In fact, only if this occurs, the small scales show a universal dynamic and there is the possibility of modelling the unresolved turbulent scales with a model independent from the flow.

Once the filtered velocity has been defined, it is possible to compute the *residual velocity* (or *subgrid velocity*) u'_j:

$$u'_j = u_j(x,t) - \tilde{u}_j(x,t) \qquad (3.49)$$

From the expression (3.49) follows:

$$u_j(x,t) = \tilde{u}_j(x,t) + u'_j \qquad (3.50)$$

Equation (3.50) demonstrates that velocity (and in general every other physical quantity) can be seen as the sum of a filtered term and its residual field.

This decomposition is very similar to Reynolds decomposition used by RANS approach, with two major differences:

- $\tilde{u}_j(x,t)$ is a random field that depends on the filter size
- In general, filtered residual is not null

$$\widetilde{u_j'} \neq 0 \tag{3.51}$$

Now that the new decomposition form is available, the filtered Navier-Stokes equations can be derived for in incompressible fluid. For simplicity, both equations are expressed in Einstein's notation.

Continuity Equation:

$$\frac{\partial \tilde{u}_j}{\partial x_j} = 0 \tag{3.52}$$

As for the RANS approach, the filtered field $\tilde{\boldsymbol{u}}$ is solenoidal. In can be demonstrated that also the residual field $\boldsymbol{u}'$ is solenoidal. In fact:

$$\frac{\partial \tilde{u}_j}{\partial x_j} = \frac{\partial}{\partial x_j}\left(\tilde{u}_j + u_j'\right) = \frac{\partial \tilde{u}_j}{\partial x_j} + \frac{\partial u_j'}{\partial x_j} = \frac{\partial u_j'}{\partial x_j} = 0 \tag{3.53}$$

Momentum Equation:

$$\frac{\partial \tilde{u}_i}{\partial t} + \frac{\partial}{\partial x_j}\left(\tilde{u}_i \tilde{u}_j\right) = -\frac{1}{\rho}\frac{\partial \tilde{p}}{\partial x_i} + \frac{\partial}{\partial x_j}\left(2\nu \tilde{S}_{ij}\right) - \frac{\partial \tau_{ij}^R}{\partial x_j} \tag{3.54}$$

Where $\tilde{S}_{ij}$ is the *filtered rate of strain tensor* and $\tilde{\tau}_{ij}$ is the *residual-stress tensor,* defined as:

$$\tau_{ij}^R = \widetilde{u_i u_j} - \tilde{u}_i \tilde{u}_j \tag{3.55}$$

This "additional" stress tensor has six independent components and it only counts for the not resolved scales effects. So, to close the turbulence problem associated to LES modelling, a new model for the *residual-stress tensor* τ^R is the needed.

To begin, we observe that the trace of the residual-stress tensor (is equal to twice the residual kinetic energy:

$$\tau_{ii}^{R} = \widetilde{u_i u_i} - \tilde{u}_i \tilde{u}_i = 2k_R \tag{3.56}$$

So, the *anisotropic residual-stress tensor* τ^r is:

$$\tau_{ij}{}^{r} = \tau_{ij}{}^{R} - \frac{2}{3} k_R \delta_{ij} \tag{3.57}$$

Where δ_{ij} is the *Kronecker delta*. Reversing equation (3.57), we can then obtain the residual-stress tensor as sum of the isotropic residual-stress tensor and the anisotropic residual-stress tensor:

$$\tau_{ij}{}^{R} = \frac{2}{3} k_R \delta_{ij} + \tau_{ij}^{r} \tag{3.58}$$

Substituting (3.58) into (3.54) and including isotropic residual-stress in the modified filtered pressure:

$$\tilde{P} = \tilde{p} + \frac{2}{3} k_R \tag{3.59}$$

The filtered momentum equation can be re-written in the following form:

$$\frac{\partial \tilde{u}_i}{\partial t} + \frac{\partial}{\partial x_j}\left(\tilde{u}_i \tilde{u}_j\right) = -\frac{1}{\rho}\frac{\partial \tilde{P}}{\partial x_i} + \frac{\partial}{\partial x_j}\left(2\nu \tilde{S}_{ij}\right) - \frac{\partial \tau_{ij}^{r}}{\partial x_j} \tag{3.60}$$

As for RANS approach, the turbulence problem associated with LES modelling and represented by the system of filtered Navier-Stokes equations (3.52) and (3.60) is not closed, so, a new model for the *residual-stress tensor* τ^r is necessary. Being this model associated with the scales smaller than the filter size (in explicit filtering) and than the grid size (in implicit filtering), it is named *Sub-Grid Scale model (SGS)*.

In the next paragraph, the problem concerning the Sub-Grid Scale model will be treated, analysing in detail the characteristics of the three different models provided by the CFD software *STAR CCM+*. These models are: *Smagorinsky model*, *Dynamic Smagorinsky model* and *WALE model*.

For more detailed descriptions of how these models work, the author suggests to refer to Pope [6] and the User Guide [28]. Further excellent references can be found consulting Sagaut [4] and John [5].

3.5.1 The Smagorinsky Sub-Grid Scale Model

The *Smagorinsky Sub-Grid Scale model*, introduced in 1963 by Joseph Smagorinsky [43], is the first sub-grid model proposed to close the LES problem previously described.

As all the SGS models, it is based on the concept of *eddy viscosity*, that is equivalent to the idea of *turbulent viscosity* for the RANS approach: in fact, also in this case the effect of the residual unresolved scales is taken into account increasing the viscosity.

Introducing the Boussinesq's hypothesis of direct proportionality between the *residual-stress tensor* τ^r and the *filtered rate of strain* $\tilde{S}$:

$$\tau_{ij}{}^r = -2\nu^r \tilde{\mathrm{S}}_{ij} \tag{3.61}$$

Where ν^r is called *sub-grid cinematic viscosity* or *residual cinematic viscosity* and is function of position and time ($\nu^r = \nu^r(x,t)$). Equation (3.61) also means that the *residual-stress tensor* is always parallel to the *filtered rate of strain.*

Substituting equation (3.61) into (3.60), we obtain:

$$\frac{\partial \tilde{u}_i}{\partial t} + \frac{\partial}{\partial x_j}\left(\tilde{u}_i \tilde{u}_j\right) = -\frac{1}{\rho}\frac{\partial \tilde{P}}{\partial x_i} + \frac{\partial}{\partial x_j}\left[2(\nu + \nu^r)\tilde{S}_{ij}\right] \tag{3.62}$$

Again, the system made by equations (3.52) and (3.60) is not closed because it is necessary to introduce a model for the *residual cinematic viscosity* ν^r.

This model, for sure, will depend on the physical quantities that characterize the turbulence level of the filtering cell at a filtering length equal to Δ.

If Δ lays in the inertial range of turbulence, according to Kolmogorov's theory, the whole power introduced at larger scales ($\varepsilon_{LS} = \varepsilon$) flows into inertial range up to scale Δ ($\varepsilon_{\Delta} = \varepsilon$) and then should flow to smaller scales until Kolmogorov's length scale η is reached and the viscous dissipation occurs ($\varepsilon_{\eta} = \varepsilon$). The energy flux that arrives at a length scale equal to Δ is:

$$\varepsilon = C_s{}^2 \frac{\langle |\delta u|_{\Delta} \rangle^3}{\Delta} \tag{3.63}$$

Where $\langle |\delta u|_{\Delta} \rangle$ is the average velocity increase at length scale equal to Δ.

The energy flux defined by equation (3.63), according to theory, should flow towards the smallest scales (that are smaller than the filtering size Δ) until it is dissipated, but this phenomenon cannot be described by the model because the filtering operation cuts-off all the information associated with unresolved scales. The only way to account for this phenomenon is to introduce a fictitious dissipation at the smallest simulated length scale, that is also equal to the filtering size Δ.

For K41 theory, this dissipation is equal to:

$$\varepsilon = \nu^r \frac{\langle |\delta u|_\Delta \rangle^2}{\Delta^2} \tag{3.64}$$

Combining equations (3.63) and (3.64), we obtain:

$$\nu^r = {C_s}^2 \langle |\delta u|_\Delta \rangle \, \Delta \tag{3.65}$$

To estimate $\langle |\delta u|_\Delta \rangle$, we can multiply the gradient of the filtered velocity by the filtering length Δ: this operation should seem less complicated if we consider a one-dimensional case, for which the following relation is valid:

$$\delta u = \frac{du}{dx} \Delta x \tag{3.66}$$

The *Smagorinsky model*, for a general three-dimensional case, approximates the derivative of equation (3.66) with the *characteristic filtered rate of strain* $\tilde{\mathcal{S}}$, that computes the magnitude of filtered velocity gradients near to the filtering cell:

$$\tilde{\mathcal{S}} = \sqrt{2 \tilde{\mathrm{S}}_{ij} \tilde{\mathrm{S}}_{ij}} \tag{3.67}$$

From (3.67) and (3.66) follows:

$$\langle |\delta u|_\Delta \rangle = \tilde{\mathcal{S}} \Delta \tag{3.68}$$

Proceeding to the substitution of equation (3.68) into equation (3.65), we obtain the closure equation for the *residual viscosity*, according to the *Smagorinsky model*:

$$\nu^r = (C_s\Delta)^2\tilde{S} \tag{3.69}$$

Once the calibration constant C_s is known, the LES problem is closed (because the *characteristic filtered rate of strain* $\tilde{S}$ only depends on the filtered velocities) and it can be solved numerically.

In most cases, the optimal value for the calibration constant C_s is 0.12, but in literature values in the range 0.06-0.2 are reported.

In *STAR CCM+* [28], the Smagorinsky model is available with the addition of a correcting factor to achieve better results when simulating wall-bounded flows.

Using the aforementioned software, the sub-grid scale dynamic viscosity is computed as follows:

$$\mu_{SGS} = \rho\Delta^2\tilde{S} \tag{3.70}$$

Where ρ is the density and Δ is the grid filter width, that is directly related to the cell volume V and the wall distance d and is defined by the following system:

$$\Delta = \begin{cases} f_v C_s V^{\frac{1}{3}} & \text{if length scale limit not applied} \\ f_v \min\left(\kappa d, C_s V^{\frac{1}{3}}\right) & \text{if length scale limit is applied} \end{cases} \tag{3.71}$$

Where f_v is the *Van-Driest damping function* and κ is the Von Karman constant, whose value is usually set equal to 0.41.

The *Van-Driest damping function* f_v, in *STAR CCM+*, is computed as follows:

$$f_v = \begin{cases} 1 & \text{no damping} \\ 1 - \exp\left(-\frac{y^+}{A}\right) & \text{standard} \\ \sqrt{1 - \exp\left(-\frac{y^+}{A}\right)^3} & \text{modified} \end{cases} \tag{3.72}$$

Where y^+ is the dimensionless wall distance and A is a model coefficient. In *STAR CCM+*, in standard configuration, A is set equal to 25.

As seen in this paragraph, the Smagorinsky model is the most basic among all SGS models. In fact, it is not so accurate in simulating all kind of flows, especially struggling with wall-bounded ones. Furthermore, the constant C_s is not universal and depends on local flow conditions. This fact has brought the researchers to study new solutions to the problem, proposing the two alternative SGS models described in next paragraphs.

3.5.2 The Dynamic Smagorinsky Sub-Grid Scale Model

The *Dynamic Smagorinsky SGS model* has the same form and theorical bases of the basic Smagorinsky SGS model, but instead of using a constant value for the model coefficient C_s set by the user, the model computes a local time-varying coefficient by test-filtering the flow field of the nearby cells on a length scale larger than the grid size. It was introduced for the first time by Germano et al. [44] in 1991.

This dynamic variation to the model allows to obtain more reliable results in wall-bounded flow simulations without the use of damping functions.

Starting from equation (3.70), the parameter Δ^2 is computed dynamically in the following way:

$$\Delta^2 = {C_s}^2 V^{\frac{2}{3}} \tag{3.73}$$

If $\tilde{\phi}$ is a grid-filtered LES variable in a cell, the corresponding test-filtered value $\hat{\tilde{\phi}}$ is given by:

$$\hat{\tilde{\phi}} = \frac{1}{\sum_{n=0}^{N} V_n} \sum_{n=1}^{N} \tilde{\phi}_n V_n \tag{3.74}$$

Where the subscripts denote the number of the cell: cell-0 is the current cell and cell-1, cell-2, …, cell-N are the N neighbour cell of cell-0.

Using the superscript notation to denote the test-filtered variables, the dynamic coefficient ${C_s}^2$ is computed as follows:

$${C_s}^2 = \frac{\langle L_{ij} M_{ij} \rangle}{\langle M_{ij} M_{ij} \rangle} \tag{3.75}$$

With angle brackets denoting averaging operation and where L_{ij} and M_{ij} are:

$$L_{ij} = \tilde{u}_i \hat{\tilde{u}}_j - \hat{\tilde{u}}_i \hat{\tilde{u}}_j \tag{3.76}$$

$$M_{ij} = 2\tilde{L}^2 \left(\left|\tilde{S}\right| \hat{\tilde{S}}_{ij} - \frac{\hat{L}^2}{\tilde{L}^2} \left|\hat{\tilde{S}}\right| \hat{\tilde{S}}_{ij} \right) \tag{3.77}$$

With:

- $\tilde{L}$ is the grid filter length
- $\frac{\hat{L}^2}{\tilde{L}^2}$ is the filter width ratio and is a model coefficient to be set

As can be seen from equation (3.77), M_{ij} is obtained by subtracting to the Smagorinsky subgrid stress tensor at the grid filter scale the same tensor computed at the test filter scale.

3.5.3 The WALE Sub-Grid Scale Model

The *Wall-Adapting Local-Eddy Viscosity SGS model* (WALE) is the last and most modern SGS model available in *STAR CCM+*. First introduced in 1999 by Nicoud et al. [45], it uses a novel form of computing velocity gradient tensor in its formulation and does not require any near-wall special treatment to accurately simulate the flow in near-wall zones. On the other side, it suffers the fact that in its formulation, there is the need of defining a calibration constant that is, again, non-universal. Nevertheless, validations using *STAR CCM+* have shown that WALE model is so sensitive to changes of the value of this constant [28].

The WALE SGS model provides the following formula for computing residual dynamic viscosity:

$$\mu_{SGS} = \rho \Delta^2 S_w \tag{3.78}$$

The length scale Δ is again defined in terms of the cell volume V:

$$\Delta = \begin{cases} C_w V^{\frac{1}{3}} & \text{if length scale limit not applied} \\ \min\left(\kappa d, C_w V^{\frac{1}{3}}\right) & \text{if length scale limit is applied} \end{cases} \tag{3.79}$$

C_w is the calibration constant of the model and κ is the *Von Karman's constant*.

The deformation parameter S_w is defined as follows:

$$S_w = \frac{\left(\tilde{\boldsymbol{S}}_{\boldsymbol{d}} : \tilde{\boldsymbol{S}}_{\boldsymbol{d}}\right)^{\frac{3}{2}}}{\left(\tilde{\boldsymbol{S}}_{\boldsymbol{d}} : \tilde{\boldsymbol{S}}_{\boldsymbol{d}}\right)^{\frac{5}{4}} + \left(\tilde{\boldsymbol{S}} : \tilde{\boldsymbol{S}}\right)^{\frac{5}{2}}} \tag{3.80}$$

Where:

$$\tilde{\boldsymbol{S}} = \frac{1}{2}\left(\nabla\tilde{\boldsymbol{u}} + \nabla\tilde{\boldsymbol{u}}^{\boldsymbol{T}}\right) \tag{3.81}$$

$$\tilde{\boldsymbol{S}}_{\boldsymbol{d}} = \frac{1}{2}\left[\nabla\tilde{\boldsymbol{u}} \cdot \nabla\tilde{\boldsymbol{u}} + \left(\nabla\tilde{\boldsymbol{u}} \cdot \nabla\tilde{\boldsymbol{u}}\right)^{\boldsymbol{T}}\right] - \frac{1}{3}\operatorname{tr}\left(\nabla\tilde{\boldsymbol{u}} \cdot \nabla\tilde{\boldsymbol{u}}\right)\mathbb{I} \tag{3.82}$$

The model coefficient C_w is not universal. Typical values for C_w reported in literature are usually included in the range 0.55-0.6 [4]. The standard value adopted by *STAR CCM+* is 0.544 [28].

3.6 The Synthetic Eddy Method

The definition of realistic inflow boundary and initial conditions is crucial to achieve successful results in Large Eddy Simulations and, in general, in scale-resolving simulations.

In literature few methods were proposed by researchers with the aim of introducing simple but effective methods capable to generate reliable turbulent inflow conditions for CFD simulations. An exhaustive description of these models can be found by the reader in works made by Sagaut [4] and Tabor et al. [7].

The CFD software *STAR CCM+* provides two different methods for generating turbulent conditions:

- The *Anisotropic Linear Forcing Method* (ALF), that is suitable for generating turbulent fluctuations inside a specified volume.
- The *Synthetic Eddy Method* (SEM), that treats the instantaneous velocity field as a superposition of spinning eddies, whose spin and position are defined by a normalized uniform distribution.

For all the simulations presented in this project, the *Synthetic Eddy Method* was adopted to define turbulent inflow boundary and initial conditions. A brief explanation of the SEM is presented in the following paragraph and it is based on the *STAR CCM+* User Guide [28].

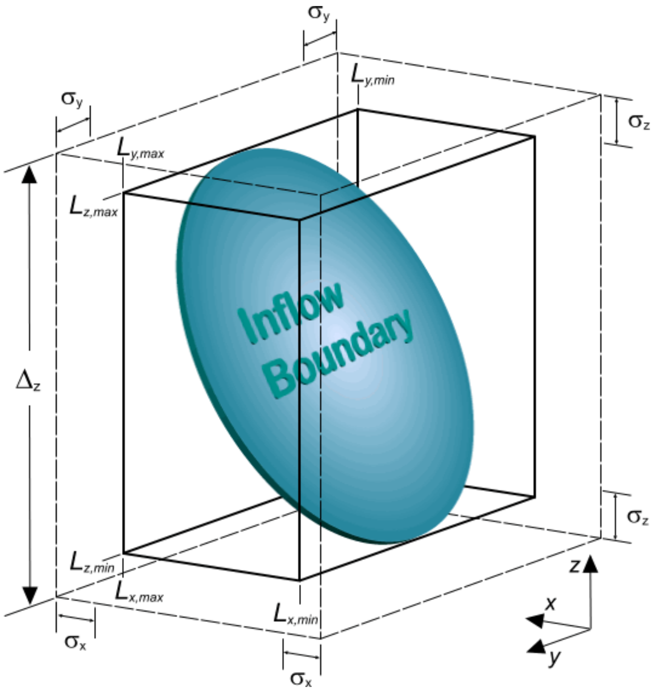

Figure 3.1 3-D visualization of SEM geometric limits defined by equations (3.83) and (3.84). Picture from the STAR CCM+ User Guide [28]

Primarily, it is important to define the geometric limits to identify the space on which the method will work. So, let us consider that the fluctuating velocity signal is generated in the interval:

$$[L_{x,min}, L_{x,max}] \times [L_{y,min}, L_{y,max}] \times [L_{z,min}, L_{z,max}] \tag{3.83}$$

This interval is based on the geometric limits of the inflow boundary. The signal also uses a shape in:

$$[-\sigma_x, \sigma_x] \times [-\sigma_y, \sigma_y] \times [-\sigma_z, \sigma_z] \tag{3.84}$$

Where σ_i defines the mean eddy length in the i-th direction. A better idea of the geometry defined by equations (3.83) and (3.84) is given by observing Figure 3.1. The shape function $\mathbf{f}(\mathbf{x})$ that characterize the eddies satisfies the following normalization property:

$$\frac{1}{\Delta_x \Delta_y \Delta_z} \int_{-\frac{\Delta_x}{2}}^{\frac{\Delta_x}{2}} \int_{-\frac{\Delta_y}{2}}^{\frac{\Delta_y}{2}} \int_{-\frac{\Delta_z}{2}}^{\frac{\Delta_z}{2}} \|\mathbf{f}(\mathbf{x})\| \, \mathrm{d}\mathbf{x} = 1 \tag{3.85}$$

Where:

$$\Delta_i = L_{x,max} - L_{x,min} + 2\sigma_i \tag{3.86}$$

Any function that satisfies equation (3.85) is suitable to be taken as shape function. *STAR CCM+*, as shape function, adopts the following expression, that represents the influence exerted by the k-th eddy at position $\mathbf{x}_k$ on a point $\mathbf{x}$ on the inflow surface:

$$\mathrm{f}(\mathrm{x}_i) = \max\left(0, 1 - \frac{|x_i - x_{i,k}|}{\sigma_{i,k}}\right) \tag{3.87}$$

Where:

- x_i is the i-th coordinate of the point $\mathbf{x}$
- $x_{i,k}$ is the i-th coordinate of the center of the k-th eddy

Of course, each eddy has its own position $\mathbf{x}_k$, its own length scale σ_k and its own spin direction, that is defined as follows:

$$\varepsilon_{i,k} = \pm 1 \tag{3.88}$$

The sign of rotation of each eddy is chosen randomly from a uniform distribution to ensure that the generated velocity signal satisfies:

$$\overline{v_i' v_j'} = \delta_{ij} \tag{3.89}$$

The overbar denotes the presence of an averaging operation, while δ_{ij} is the *Kronecker delta*.

The *eddy turbulent length scale* $\boldsymbol{\sigma}_k$ can, in principle, be function of space and can also vary according to the coordinate direction. Currently, *STAR CCM+* assumes the turbulent length scale to be *isotropic*: this means that it can vary according to position in space, maintaining the same value along all the coordinate directions. The coordinates of the various eddy centers are selected randomly inside the volume $\Delta_x \times \Delta_y \times \Delta_z$, where Δ_x, Δ_y and Δ_z are defined by (3.86). The number of eddies *N* is obtained by dividing the volume by the *average eddy volume* $\bar{\sigma}^3$, where $\bar{\sigma}$ is the *average eddy turbulent length scale*.

Assuming frozen turbulence, the position of the k-th eddy advances along each direction according to:

$$x_{i,k}^{new} = x_{i,k}^{old} + \mathrm{V}_i \Delta t \tag{3.90}$$

Where Δt is the time-step. The convective velocity V is computed as the average of the mean inflow velocity profile over the inflow area. The fluctuation velocity signal is therefore obtained as:

$$\mathrm{v}_i'(\mathbf{x}, t) = \frac{1}{\sqrt{N}} \sum_{k=1}^{N} \varepsilon_{i,k}\, \mathrm{f}_k(\boldsymbol{\sigma}_k, \mathbf{x}, t) \tag{3.91}$$

The instantaneous velocity field is computed as:

$$\mathrm{v}_i(\mathbf{x}, t) = \mathrm{V}_i(\mathbf{x}, t) + a_{ij} \mathrm{v}_i'(\mathbf{x}, t) \tag{3.92}$$

The factors a_{ij} are computed from the Cholensky decomposition of the *Reynolds stress tensor* R_{ij} as follows:

$$\begin{bmatrix} \sqrt{R_{11}} & 0 & 0 \\ \dfrac{R_{21}}{a_{11}} & \sqrt{R_{22} - a_{21}^2} & 0 \\ R_{31} - a_{11} & \dfrac{R_{32} - a_{21} a_{31}}{a_{22}} & \sqrt{R_{33} - a_{31}^2 - a_{32}^2} \end{bmatrix} \tag{3.93}$$

Where:

$$R_{ij} = \overline{\mathrm{v}_i'' \mathrm{v}_j''} \tag{3.94}$$

Given the turbulence intensity I at the inlet the and invoking the hypothesis of isotropic turbulence, the normal components of the stress tensor can be then computed using the following relations:

$$I = \sqrt{\frac{\mathrm{v}''^2}{\mathrm{V}^2}} \tag{3.95}$$

$$k = \frac{3}{2}\mathrm{v}'' \tag{3.96}$$

$$\mathrm{V}^2 = \mathrm{V}_i\mathrm{V}_i \tag{3.97}$$

$$R_{ii} = I^2\mathrm{V}^2 \tag{3.98}$$

From what we have seen in this paragraph, the *Synthetic Eddy Method* is really capable of generating fluctuating turbulent velocity fields. However, it should be underlined that the SEM produces turbulent structures which are only an approximation of real turbulence and must be allowed to develop their proper correlations.

The correlations develop naturally as the eddies are convected downstream by the flow. Hence, to allow this behaviour to occur, it is important to leave enough distance between the inlet boundary and the region of interest.

3.7 The Temporal Discretization

The analysis made in this Thesis has transient nature: this means that the *time* variable must be considered, advancing by small amount of time, called *time-steps*, during the simulations. With the aim of computing the time derivative of any physical quantity, several methods have been proposed by researchers.

In general, in engineering applications, the *Implicit Euler Scheme* is the most used: this approach, for each physical time-step, involves some number of inner iterations to bring to convergence the solution for that instant of time. The size of the time-step and the number of inner iterations are set by the user. In general, the choice of the time-step size is limited by two conditions:

- Nyquist's criterion
- Courant Friedrich Lewy (CFL) condition

The first criterion is based on the fact that, for effectively capturing the transient phenomena, the time-step must be shorter than the period. According to Nyquist's criterion, for every period, there must be at least two time-steps to achieve a good result in simulating the physics of a transient system.

The CFL condition is, in most cases, the most restrictive condition on the choice of time-step size. This condition is expressed by the following relation (with the purpose of making things less complicated, we analyse the one-dimensional case):

$$C = \frac{u\,\Delta t}{\Delta x} \tag{3.99}$$

C is called Courant Number and is a non-dimensional number. When using an implicit scheme for the temporal discretization, this number has to be at least lower than 5-10 to ensure solution stability. Usually it is recommended to choose the time-step size with the aim of achieving Courant Number values equal to 1 or smaller. In fact, Courant Number equal to 1 means that informations are propagating from one cell to the adjacent one in the given time-step without jumping over other intermediate cells.

As you can see from equation (3.99), the Courant Number doesn't just depend on the time-step size Δt, but also on the velocity of propagation of the informations (u) and on the distance betweentwo cells (Δx). This means that, with the same time-step size, solutions obtained using coarser meshes will show lower Courant Number values than solutions obtained on finer meshes.

Chosen the time-step size following the two criteria previously explained, let us analyse the possible schemes of temporal discretization usually available on commercial CFD softwares.

For this project, after the decision of using the *Implicit Unsteady* model [28] for the temporal discretization, the software *STAR CCM+* provides two schemes which differ in the degree of accuracy. The simplest one is a *first-order time discretization scheme*: it uses the solution of the current time-step t_{m+1} and of the previous time-step t_m to compute the temporal derivative. Given a generic function $\phi(t)$, its time derivative evaluated for at time-step t_{m+1} is:

$$\frac{d\phi(t_{m+1})}{dt} = \frac{\phi(t_{m+1}) - \phi(t_m)}{\Delta t} \tag{3.100}$$

Where Δt is the time-step size. In the end, adopting this scheme, only two "points" are necessary.

The most accurate scheme proposed by *STAR CCM+* is the *second-order temporal discretization scheme*: this method is more expensive because, in addition to the time-steps t_{m+1} (current) and t_m (previous), it needs the value of the function at the time-step t_{m-1} to compute the time derivative. Therefore, three "points" are necessary. Using this scheme, the time derivative is computed as follows:

$$\frac{d\phi(t_{m+1})}{dt} = \frac{\frac{3}{2}\phi(t_{m+1}) - 2\phi(t_m) + \frac{1}{2}\phi(t_{m-1})}{\Delta t} \tag{3.101}$$

Where Δt is again the time-step size. For all the simulations made for this project, a second-order accuracy scheme was chosen to achieve more accurate solutions, though the computational costs for every iteration raise. In case the reader is interested in deepening the theory behind the topic of this paragraph, the author suggests to refer to Peric et al. [31], Moulkalled et al. [32] and the User Guide [28].

Chapter 4

Physics and Computational Set-Up

As previously reported, the definition of the inflow conditions and of the initialization are of crucial importance when the LES approach is taken into account to simulate turbulence. To fulfil these requirements, a new method for the determination of the inlet boundary conditions is introduced and explained in detail, also focusing on the initialization strategy.

Inside this chapter, after the definition of the nozzle geometry and of the physical properties of water and water vapor, the mesh set-up is discussed too, paying attention to the fact that the implicit Large Eddy Simulation technique works effectively only when the sizes of all the cells is chosen in order to be internal to the turbulent inertial subrange of the energy cascade.

4.1 Geometry

Turbulence is, in general, an unsteady and 3-D phenomenon: this means that it is not possible to take advantage of the symmetries of the problem except when average flow fields are taken into account.

Its replication using turbulence models such as LES or DNS requires the reconstruction of the full 3-D geometry of the problem. So, the full 3-D geometric model of the axisymmetric converging-diverging nozzle previously shown in Paragraph 2.3.1 (see Figure 2.6) was reproduced in *STAR CCM+*.

An inlet pipe and an outlet pipe were also added respectively before and after the Venturi nozzle. The inlet section distance from the section of interest (the throat) was chosen in order to ensure the achievement of the fully developed turbulent flow conditions at the Venturi entrance. A distance equal to $10d$ was selected, following the guidelines provided by Cengel et al. [30].

Instead, the outlet section was located at a distance of 0.73 m from the throat, replicating the position of the outlet pressure transducer in Hogendoorn [22] and Jahangir et al. [46] set-ups.

A 2-D scheme of the computational set-up geometry is next provided in Figure 4.1.

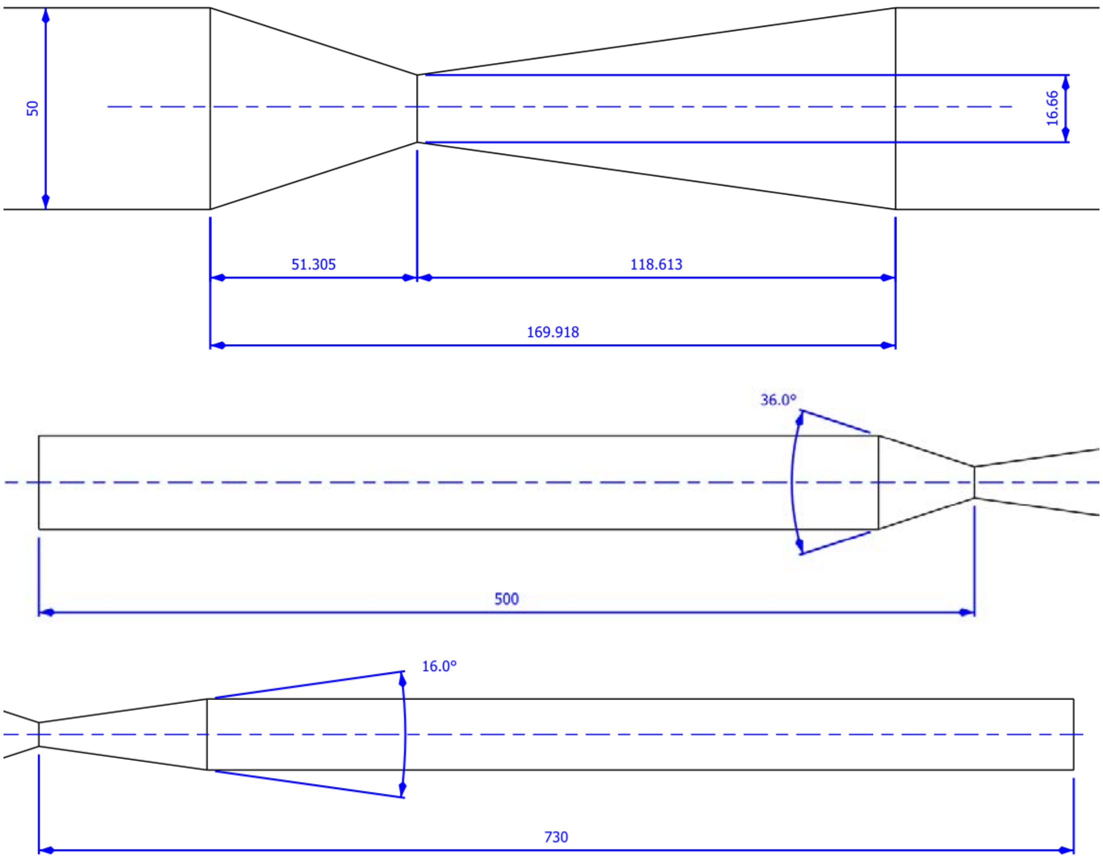

Figure 4.1 Schematic representation of the Venturi geometry showing the major parameters

4.2 Physics

To simulate the cavitating flow inside the converging-diverging nozzle described in the previous paragraph, the use of *Volume of Fluid (VOF)* method was invoked. As suggested by the User Guide [28], both phases were simulated as incompressible fluids. Considering water, the assumption of incompressibility seems to be a consistent hypothesis since the liquid velocity is far below the speed of sound. In particular, in fluid dynamics, a common rule-of-thumb states that a flow starts to be affected by compressibility effects when the Mach Number of the flow exceeds 0.3. In our case compressibility effects in the liquid can be neglected.

Since the experiments made by Hogendoorn [22] and Jahangir et al. [46] were performed at a constant temperature of 20°C, the properties of water and vapor at this temperature were taken into account and reported in Table 4.1. All the numerical values listed in this table were recovered using the software *Mini RefProp,* which provides all the thermodynamic properties of several most common fluids.

	ρ [kg/m^3]	**μ [Pa s]**	**p_{sat} [Pa]**
Water	998.2	0.001001	2339
Vapor	0.01731	$9.7272 \cdot 10^{-6}$	-

Table 4.1 Physical properties of water and water vapor at T = 20°C

Table 4.1 also reports the value of the saturation pressure because it must be defined in *STAR CCM+* when using the *Schnerr-Sauer* cavitation model. The fact that these experiments were conducted at constant temperature allowed us to ignore the energy equations too. Also the equation of state for water was not required. As regards the cavitation modelling, the *Schnerr-Sauer* model was used. To apply this model, *STAR CCM+* requires two parameters in input: the *seed density* n_0 and the *seed diameter* $d_0 = 2R_0$.

These two parameters, as previously said, must be tuned-up. Because of the long time required by every single simulation to give results, only one configuration of these two parameters was considered. The seed density and seed diameter settings are the same used by Zambon in his Master Thesis [13] for the validation test and are described in table 4.2.

To account for turbulence phenomena, the LES approach was selected. Since Literature does not provide any reference on the combined use of LES turbulence model and turbulent viscosity scaling methods (as suggested by Reboud when using k-ε turbulence model [21]), no scaling functions for the turbulent eddy viscosity were considered. It is also worth mention that *STAR CCM+* does not support the implementation of a scaling factor for the turbulent eddy viscosity when using the LES turbulence model.

As regards the sub-grid scaling model, both *Dynamic Smagorinsky SGS* and *WALE SGS* models were tested to understand which was the best one.

Seed density [1/m^3]	**Seed diameter [m]**
10^{11}	$5 \cdot 10^{-6}$

Table 4.2 Seed density and seed diameter values used for the validation test

4.3 Boundary Conditions

The numerical model requires the definition of three types of boundary conditions, one for each Venturi surface. The inflow surface was modelled as a *Velocity Inlet* boundary condition, while the *Pressure Outlet* boundary condition was applied to the outflow final section of the Venturi.

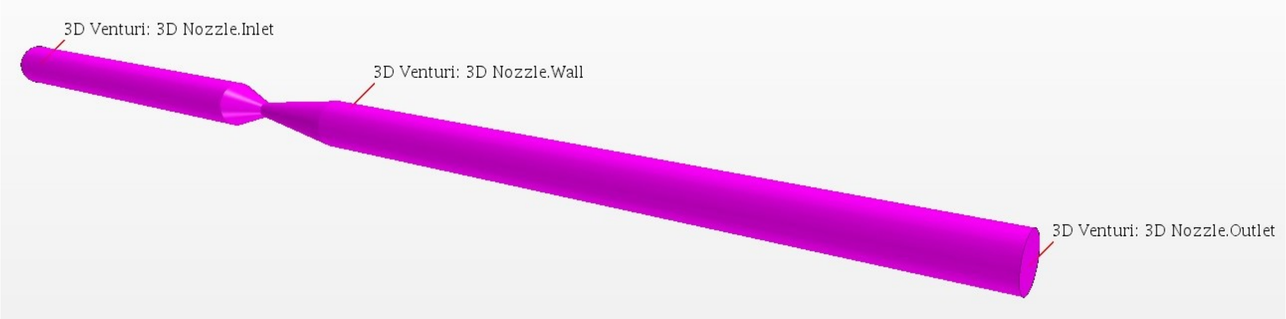

Figure 4.2 Representation of the three different Venturi surfaces where the boundary conditions were applied to: *Inlet*, *Wall* and *Outlet*

The *Wall* boundary condition was then assigned to the remaining internal surfaces of the nozzle, defining a condition of *no-slip* in correspondence of the solid walls of the Venturi. All the aforementioned boundary conditions are displayed in Figure 4.2.

The numerical value of the average inlet velocity can be computed from the outlet pressure p_{out} and the cavitation number σ. In fact, knowing these two parameters, the average throat velocity can be computed reversing equation (2.4) as follows:

$$u_0 = \sqrt{\frac{p_{out} - p_v}{\frac{1}{2}\rho\sigma}} \tag{4.1}$$

For the only validation case that we were able to investigate, the boundary conditions of $\sigma = 1$ and $p_{out} = 90kPa$ were considered. It must be underlined that, for this particular set of boundary conditions, the mechanism responsible for the partial cavitation phenomenon inside the Venturi nozzle is expected to be the *re-entrant jet mechanism*.

The average inlet velocity consequently derives from the mass conservation principle and from the assumption of incompressible flow once the area ratio is known:

$$u_0 A_0 = u_{in} A_{in} \Longrightarrow u_{in} = \frac{A_0}{A_{in}} u_0 \tag{4.2}$$

However, setting a constant velocity profile at the inlet does not fulfil the need of realistic inflow conditions that the LES turbulence model usually requires. Also the adoption of the SEM method to reproduce the random effects of turbulence on the inlet velocity field suggests to pay more attention to the inlet turbulence boundary conditions since Literature does not provide solid references on the application of such method in CFD simulations.

Thus, knowing that the flow enters the converging-diverging nozzle showing fully developed turbulent flow conditions, further CFD investigations were conducted on the fully developed turbulent flow occurring in a periodic pipe. Detailed information concerning the average velocity profile and turbulence were then obtained and applied as boundary conditions at the Venturi inlet. A brief explanation of the procedure and the results is presented in the next paragraph.

It must be underlined that *STAR CCM+* also requires the definition of an additional boundary condition for the cavitation model when the *VOF* method is applied. Thus, in the final paragraph of this section, the procedure for defining the cavitation model BCs is shortly reported.

4.3.1 Inlet Velocity and Turbulence Boundary Conditions

The reproduction of realistic turbulent inflow conditions suitable for LES is, in general, a complex problem to be solved because of the requirements that should be met by the model while generating such conditions.

According to Tabor et al. [7] the inflow boundary conditions suitable for LES should:

- Be stochastically varying
- Be set on scales that are smaller than the filter scale (spatially and temporally)
- Be compatible with the Navier-Stokes equations
- “look” like turbulence
- Allow the easy specification of turbulent properties (such as turbulence intensity and turbulent length scale)
- Be easy to implement and adjust to new inlet conditions

The CFD software *STAR CCM+* tries to fulfil most of these characteristics through the use of the *Synthetic Eddy Method (SEM).* This method, which was previously described in Section 3.6, requires the definition of three parameters to generate the turbulent velocity field: the average velocity $\bar{v}(\boldsymbol{x})$, the turbulent length scale $l_t(\boldsymbol{x})$ and the turbulence intensity $I(\boldsymbol{x})$ (the symbol $(\boldsymbol{x})$ near all the parameter symbols indicates that these parameters can also be defined as functions of the inlet coordinate).

So, to obtain information about realistic inflow conditions which must be assigned to the Venturi inlet boundary, the fully developed turbulent flow inside a periodic pipe was simulated and studied using the

LES techniques with WALE SGS model. In the following paragraphs, all the characteristics of this simulation are described in detail.

Periodic Pipe: Geometry and Mesh

Since turbulence was modelled using LES techniques, the full 3-D pipe geometry was reproduced as a cylinder of diameter D equal to 50 mm (that coincides with the diameter of the Venturi inlet pipe) and geometric ratio $L/D = 2.5$ (i.e. the pipe is 125 mm long). The pipe geometry is displayed in Figure 4.3.

The pipe unstructured mesh was generated using the *Generalized Cylinder model* with polygonal elements. To fully resolve the turbulent boundary layer in all its three regions, the *Prism Layer Mesher* was also activated. The major parameters of the mesh settings are listed in Table 4.3. The whole mesh and several details concerning the pipe outlet section and the prism layers region are displayed in Figure 4.4.

Type of mesh	Unstructured
Type of elements	Polygonal
Prism Layer Mesher	Yes
Generalized Cylinder	Yes

Base Size [mm]	1.0
Number of Prism Layers	20
Prism Layer Stretching Factor	1.3
Prism Layer Total Thickness [m]	$6.3 \cdot 10^{-4}$
Generalized Cylinder Number of Layers	63
Total number of cells	~ 357000

Table 4.3 Principal characteristics and dimensions of the periodic pipe mesh

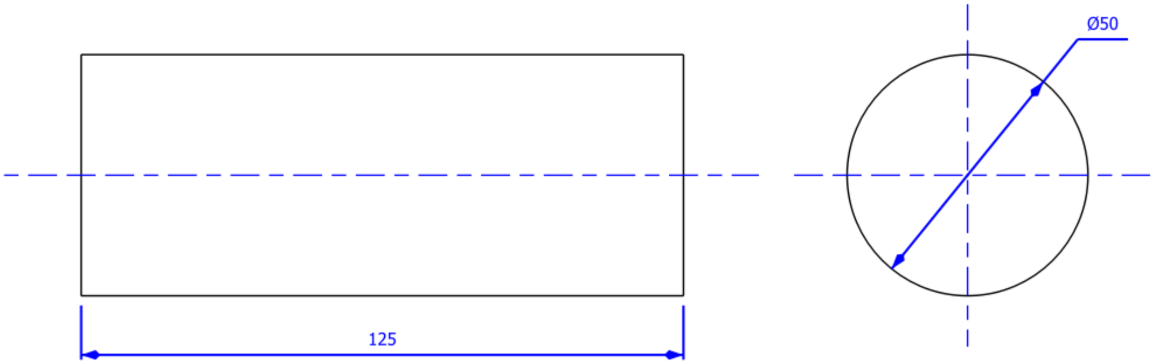

Figure 4.3 Schematic representation of periodic pipe geometry

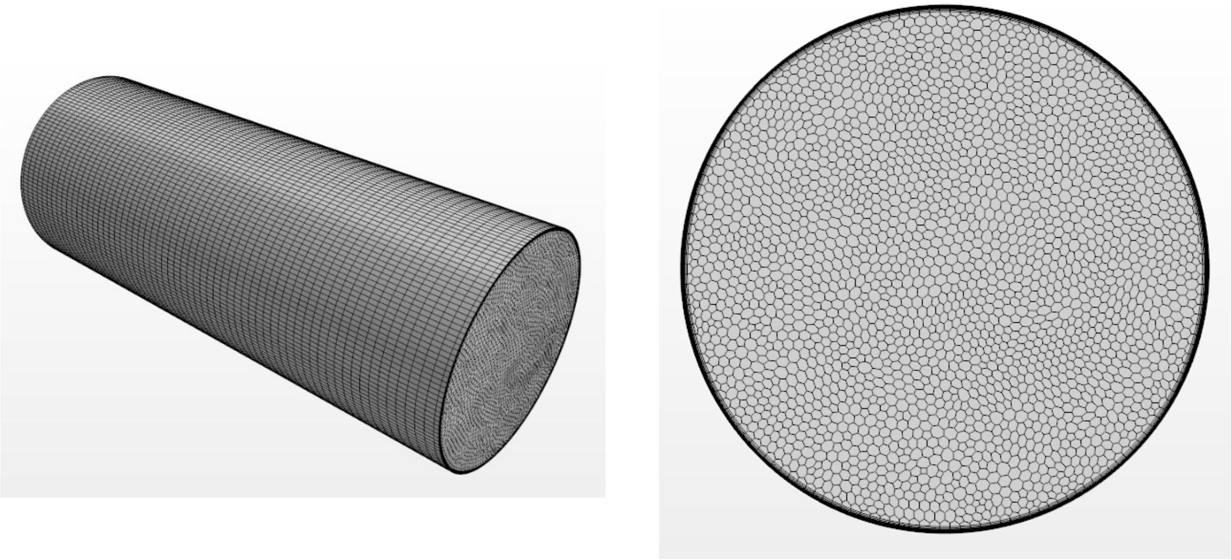

(a) Full 3-D representation of the pipe mesh. **(b)** View of the pipe mesh at the outlet section.

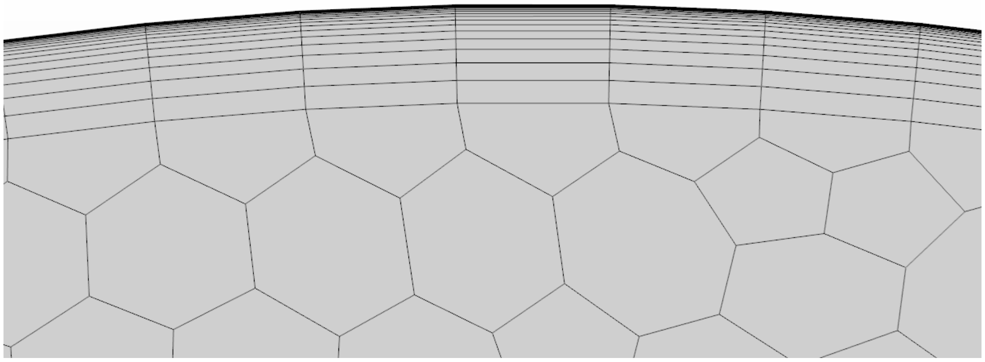

(c) Enlargement of the prism layer geometry at the outlet section of the pipe.

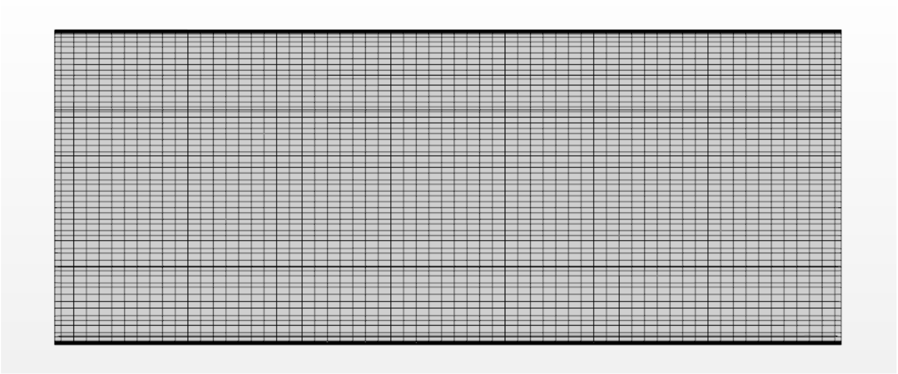

(d) Section view of the pipe mesh on the XY plane.

Figure 4.4 Picture showing several mesh views and sections

Periodic Pipe: Physics and Solver

The periodic pipe flow was simulated as a single-phase incompressible flow (selecting the *Segregated Flow* solver) and liquid water at 20°C, which properties are listed in Table 4.1, was considered. As previously said, the turbulence phenomena have been treated using the *LES* approach, applying the *WALE SGS* model. This turbulence model was chosen because it is very accurate in reproducing near-wall turbulence and allows to collect statistics of the turbulent field.

Since turbulence phenomena are unsteady, the *Implicit Unsteady* model was taken into account, using the *Eulerian Second-Order* temporal discretization scheme and setting the time-step equal to $5 \cdot 10^{-5}$ s. For each time-step, a maximum number of inner iterations equal to 5 was set. It was observed that it took nearly five flow-through times (which can be estimated using the ratio between the pipe length and the pipe average velocity) to reach fully developed turbulent flow conditions. As the simulation was running, the following physical quantities fields were monitored in correspondence of the pipe outlet section:

- *Field Means* of the three velocity components u, v and w; they will be respectively denoted by $\bar{u}(\boldsymbol{x}), \bar{v}(\boldsymbol{x})$ and $\bar{w}(\boldsymbol{x})$.
- *Field Variances* of the three velocity components u, v and w; they will be respectively denoted by $u'(\boldsymbol{x})^2, v'(\boldsymbol{x})^2$ and $w'(\boldsymbol{x})^2$, where $u'(\boldsymbol{x}), v'(\boldsymbol{x})$ and $w'(\boldsymbol{x})$ are the turbulent fluctuations of the velocity u, v and w.
- *Field Mean* of the strain rate tensor modulus S.
- *Field Mean* of the turbulent eddy viscosity μ_t.

It must be underlined that the aforementioned statistics of the flow started to be collected after a *physical time* of 2 s from the simulation start with the aim of computing some important pipe flow profiles that will be described in the final paragraph of this section. The simulation was stopped after a total physical time of 395 s, when the average velocity profile at the outlet section of the pipe was observed to be axisymmetric.

Periodic Pipe: Boundary Conditions and Initialization

To ensure the achievement of fully developed turbulent flow conditions though using a short pipe, a periodic interface between the pipe inlet section and the pipe outlet section was created, so that the flow conditions at the outlet are continuously recycled into inlet flow conditions. This method is really smart because it allows to correctly simulate fully developed turbulent flows also on short pipes, lowering the number of cells and consequently the computational costs of the simulation. Anyway, the mesh construction required the definition of three boundary conditions: *Velocity Inlet* at the pipe inlet section, *Pressure Outlet* at the pipe outlet section and *Wall* at the internal surfaces of the pipe. Once the mesh was generated, the *Mass Flow Rate* option was selected as *Fully Developed Flow Option* in order to set the mass flow rate of the pipe equal to that of the Venturi nozzle to be tested later. The value of mass flow rate of the Venturi (and therefore of the pipe) was computed considering the following Venturi validation conditions:

$$\sigma = 1 \quad ; \quad p_{out} = 90\ kPa \tag{4.3}$$

For these conditions, from equations (4.1) and (4.2), follows:

$$u_{in} = 1.46\ m/s \tag{4.4}$$

As boundary condition at the interface, the *Mass Flow Rate* option was selected and the interface mass flow rate was set equal to:

$$\dot{m} = \rho u_{in} A_{in} = 2.8615\ kg/s \tag{4.5}$$

Where A_{in} is the Venturi pipe inlet area. The pipe flow was then initialized setting the condition of horizontal constant velocity equal to 1.46 m/s (as the average inlet velocity of the Venturi nozzle) and constant pressure equal to 0 Pa. As initial conditions for turbulence intensity (I_0) and turbulent lengthscale ($l_{t,0}$), the only reference found by the author derive from the *Ansys Fluent* User Guide [55] which defines the aforementioned parameters respectively as a function of the pipe characteristic Reynolds number and the hydraulic diameter of the pipe. Being the pipe characteristic Reynolds number equal to:

$$Re_D = \frac{\rho u_{in} D}{\mu} \approx 72800 \tag{4.6}$$

Following the *Ansys Fluent* User Guide, the initial turbulence intensity and turbulent length scale were computed and set as follows:

$$I_0 = 0.16 Re_D^{-\frac{1}{8}} \approx 0.04 \tag{4.7}$$

$$l_{t,0} = 0.07D = 3.5\ mm \tag{4.8}$$

Periodic Pipe: Results

Instantaneous Velocity Field

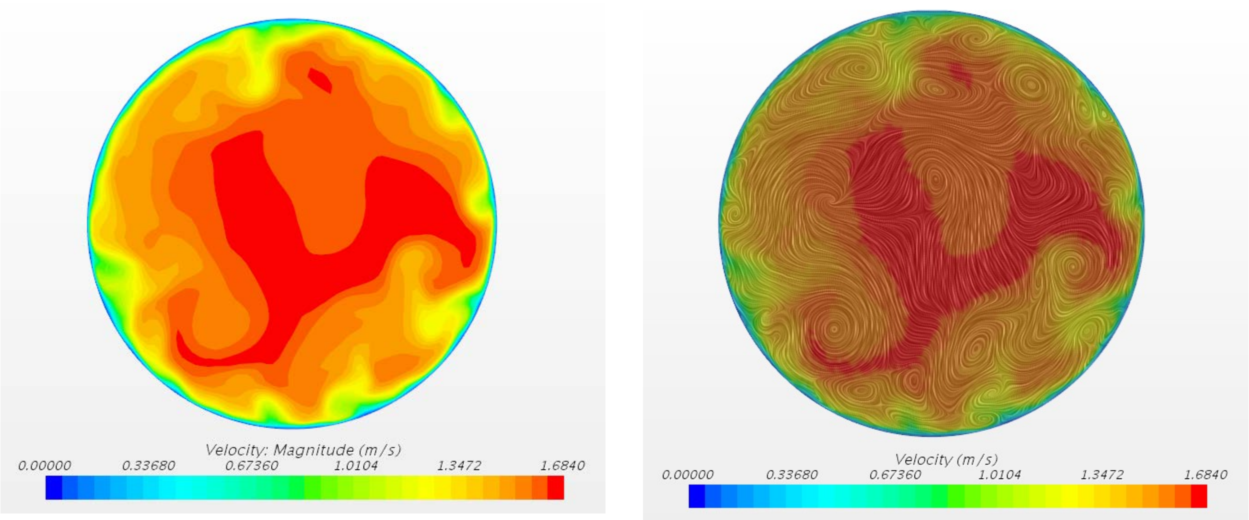

(a) Scalar scene displaying the instantaneous velocity field at the pipe outlet section

(b) Vector scene showing the integral convolution of the instantaneous velocity field at the pipe outlet section

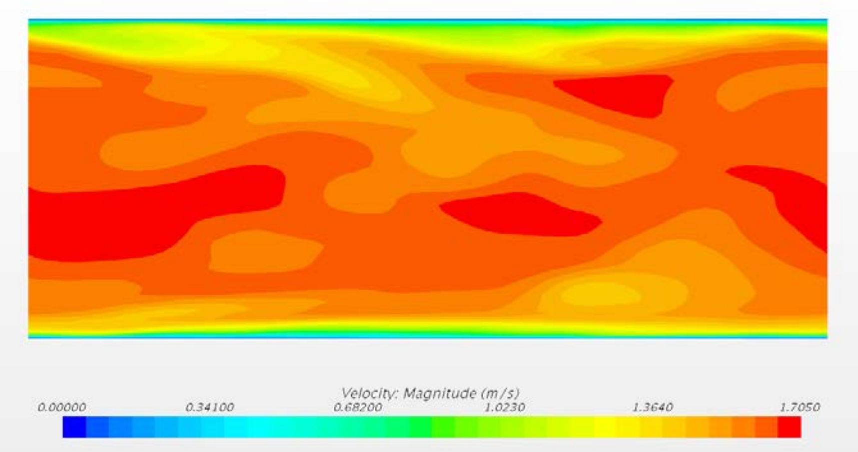

(c) Scalar scene of the instantaneous velocity field on the pipe XY plane section

Figure 4.5 Pictures showing several views of the pipe instantaneous velocity field

The instantaneous Velocity field is displayed in Figure 4.5. Observing these pictures, it is possible to notice the irregular distribution of the velocity along the pipe, which is characteristic of the fully developed turbulent flow.

Average Velocity Profile

The average profiles of the velocity components u, v and w and of the velocity magnitude U at the pipe outlet section are displayed in figure 4.6.

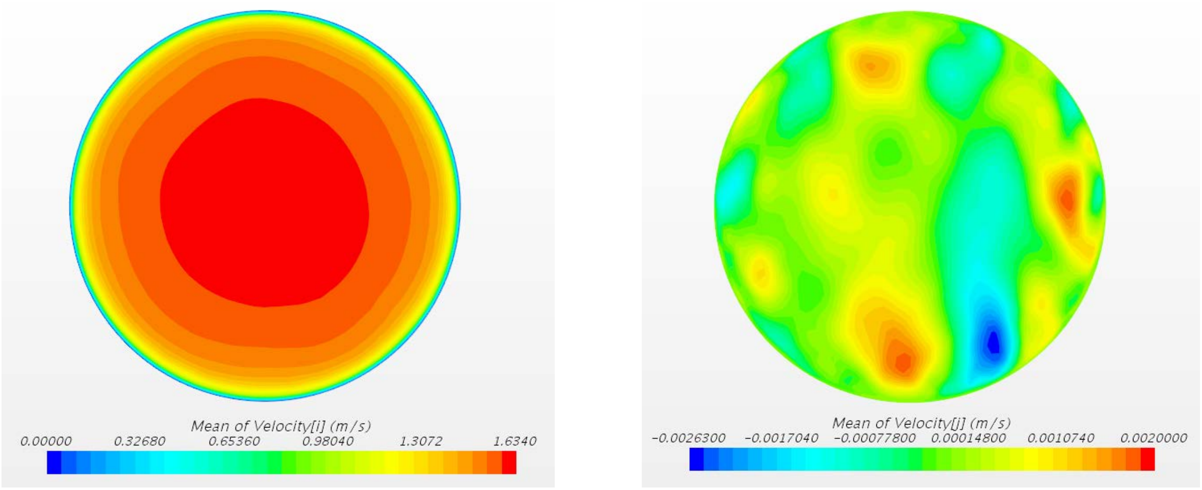

(a) Scalar scene of the average *x*-velocity profile $\bar{u}(\boldsymbol{x})$ **(b)** Scalar scene of the average *y*-velocity profile $\bar{v}(\boldsymbol{x})$

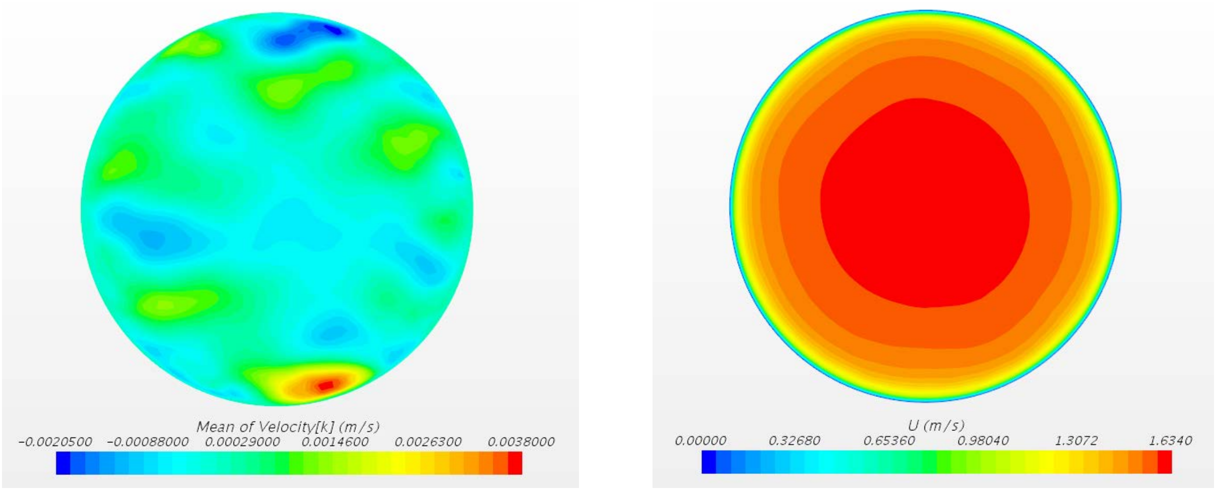

(c) Scalar scene of the average *z*-velocity profile $\bar{w}(\boldsymbol{x})$ **(d)** Scalar scene of the average velocity profile $U(\boldsymbol{x})$

Figure 4.6 Pictures displaying different average velocity profiles obtained from the periodic pipe simulation

Observing these pictures, one can notice the axisymmetric distribution of the average *x*-velocity $\bar{u}(\boldsymbol{x})$ (Figure 4.6a), while the distributions of the average *y*-velocity $\bar{v}(\boldsymbol{x})$ (Figure 4.6b) and average *z*-velocity $\bar{w}(\boldsymbol{x})$ (Figure 4.6c) seem to be more irregular. This behaviour was expected since the also the geometry has axisymmetric characteristics.

Also the distribution of the average velocity magnitude $U(\boldsymbol{x})$, that can be computed for each point using the following expression:

$$U(\boldsymbol{x}) = \sqrt{\bar{u}(\boldsymbol{x})^{\,2} + \bar{v}(\boldsymbol{x})^{\,2} + \bar{w}(\boldsymbol{x})^{\,2}} \tag{4.9}$$

Shows an axisymmetric behaviour in the whole outlet section (see Figure 4.6d) and nearly overlaps the average *x*-velocity $\bar{u}(\boldsymbol{x})$ distribution. This means that the contribution on the determination of the average velocity magnitude $U(\boldsymbol{x})$ given by both average *y*-velocity $\bar{v}(\boldsymbol{x})$ and average *z*-velocity $\bar{w}(\boldsymbol{x})$ is nearly null.

Turbulence Intensity Profile

First, to obtain the distribution of the *turbulence intensity* as a function of the space coordinate, the average velocity fluctuation $\mathrm{u}'(\boldsymbol{x})$ must be computed as the root-mean-square of the turbulent velocity fluctuations:

$$\mathrm{u}'(\boldsymbol{x}) = \sqrt{\frac{1}{3}\left[u'(\boldsymbol{x})^2 + v'(\boldsymbol{x})^2 + w'(\boldsymbol{x})^2\right]} = \sqrt{\frac{2}{3}k} \tag{4.10}$$

Therefore, the turbulence intensity $I(\boldsymbol{x})$ is defined by the ratio between the average turbulent fluctuation $\mathrm{u}'(\boldsymbol{x})$ and the average velocity $U(\boldsymbol{x})$:

$$I(\boldsymbol{x}) = \frac{\mathrm{u}'(\boldsymbol{x})}{U(\boldsymbol{x})} \tag{4.11}$$

The spatial distribution of the various average fluctuations and of the turbulence intensity obtained from the periodic pipe simulation are displayed in Figure 4.7.

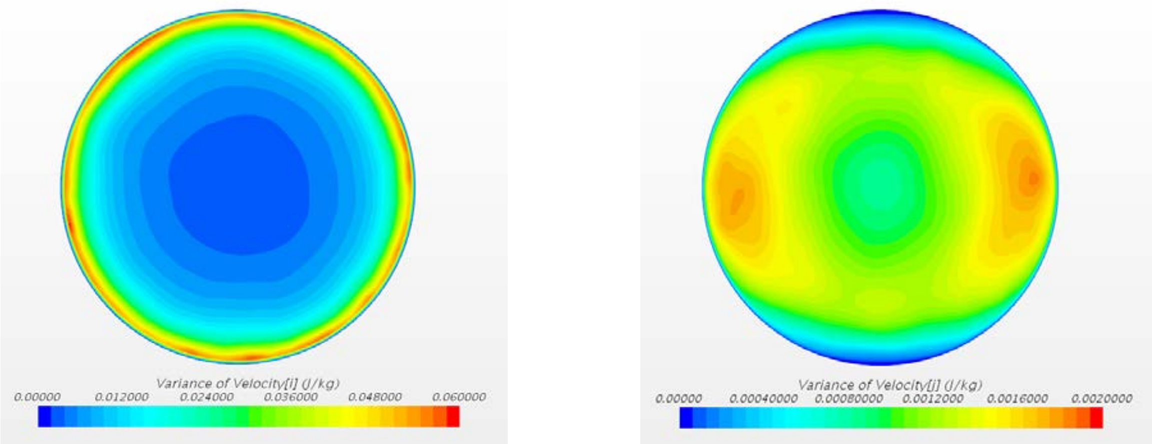

(a) Scalar scene of the *x*-velocity variance profile $u'(\boldsymbol{x})^2$ **(b)** Scalar scene of the *y*-velocity variance profile $v'(\boldsymbol{x})^2$

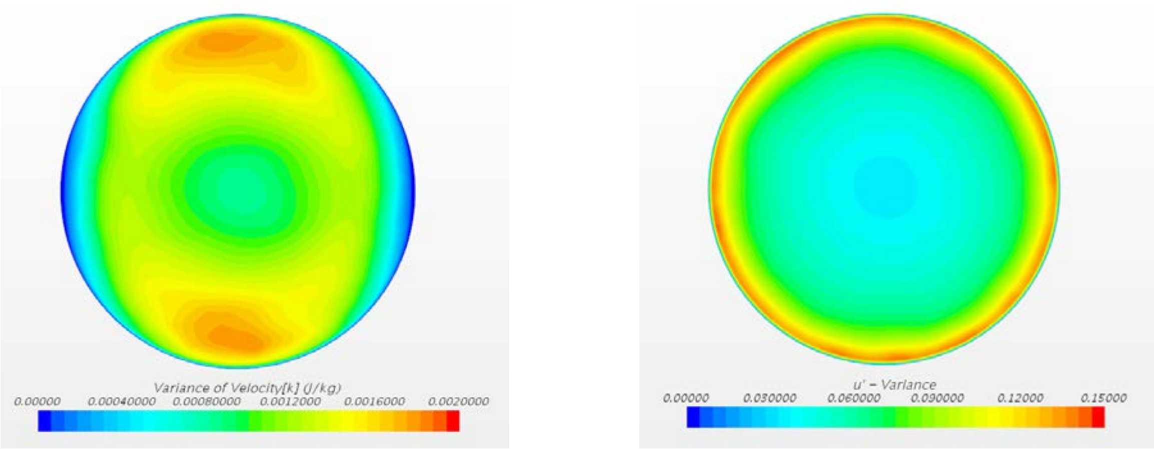

(c) Scalar scene of the *z*-velocity variance profile $w'(\boldsymbol{x})^2$ **(d)** Average turbulent velocity fluctuation profile $\mathrm{u}'(\boldsymbol{x})$

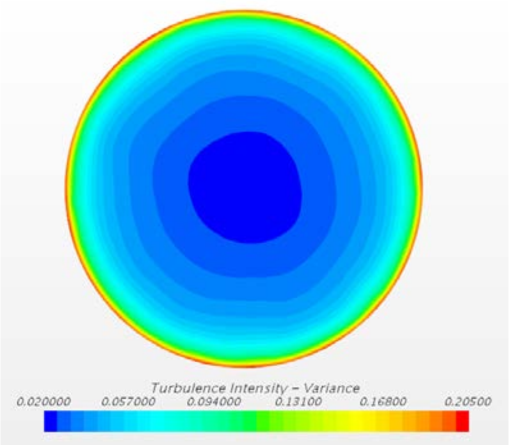

(e) Scalar scene of the turbulence intensity distribution $I(\boldsymbol{x})$

Figure 4.7 Pictures showing the different velocity variance profiles which were used to obtain the turbulence intensity distribution at the pipe outlet

As it can be observed in Figure 4.7a, the distribution of the *x*-velocity variance $u'(\boldsymbol{x})^2$ is nearly axisymmetric and has its maximum values close to the walls, where the the transition from the viscous sublayer to the turbulent layer occurs generating larger fluctuations. On the contrary, the minimum values for the *x*-velocity variance $u'(\boldsymbol{x})^2$ are located in the pipe center region, where it is known that the flow is less influenced by the wall boundaries and so turbulent fluctuations are less intense.

Instead, Figure 4.7b and 4.7c display the spatial distribution of the other two velocity variances. At first sight, we can say for sure that these distributions do not show axisymmetric properties, but on the other hand both seem to be symmetric with respect to *y*-axis and *z*-axis. Furthermore, the *y*-velocity variance distribution has its maxima on the right and left of the pipe outlet section, while its minima are located at the top and at the bottom of the pipe (see Figure 4.7b). On the contrary, the *z*-velocity variance distribution has its maxima on the pipe top and bottom and its minima are situated at the right and left of the pipe outlet surface (see Figure 4.7c).

The fact that both *y*-velocity variance and *z*-velocity variance present such distributions can be explained observing the geometry of the pipe. In fact, large velocity fluctuations in the *y*-direction are likely to occur at the top and at the bottom of the pipe, where the flow is free to move up (towards the pipe center) and down (towards the pipe wall), with the possibility of generating large *y*-velocity fluctuations. Instead, at the right and left of the pipe, the presence of the walls does not allow the flow to make large fluctuations along the *y*-direction and this involves low *y*-velocity variance values in those regions of the pipe. The same reasoning can be applied to explain why a similar inverted distribution was obtained also for the *z*-velocity variance.

Figure 4.7d displays the average velocity fluctuations distribution computed using the three monitored variances. Also from this picture, the axisymmetric shape of the field can be appreciated, with $\mathrm{u}'(\boldsymbol{x})$ increasing when moving from the pipe core towards the walls. The maximum values of this distribution are again detected in the near-wall region, where the boundary layer transition from viscous sub-layer to turbulent layer occurs.

Finally, Figure 4.7e is analysed. In this picture, the turbulence intensity distribution $I(\boldsymbol{x})$ is presented. Deriving from two axisymmetric distributions ($\mathrm{u}'(\boldsymbol{x})$ and $U(\boldsymbol{x})$), also this distribution results to be axisymmetric and presents its minimum values in the pipe core, where velocity fluctuations are low and the average velocity is maximum. On the contrary, near the walls the velocity fluctuations are maximum and the average velocity is low. This explains why the maximum values of the turbulence intensity distribution $I(\boldsymbol{x})$ are located close to the pipe walls.

Turbulent Length Scale distribution

According to *STAR CCM+* User Guide [28], the *turbulent length scale* l_t at any point can be determined using the following relation when the LES approach is applied:

$$l_t(\boldsymbol{x}) = \tau(\boldsymbol{x})\sqrt{C_t \frac{\bar{\mu}_t(\boldsymbol{x})}{\rho} \bar{S}(\boldsymbol{x})} \tag{4.12}$$

Where $\bar{\mu}_t(\boldsymbol{x})$ is the average turbulent eddy viscosity, $\bar{S}(\boldsymbol{x})$ is the *mean strain rate tensor modulus*, C_t is a model coefficient that *STAR CCM+* sets equal to 3.5 and $\tau(\boldsymbol{x})$ is the turbulent time scale, which can be computed as follows:

$$\tau(\boldsymbol{x}) = \frac{C_t}{\bar{S}(\boldsymbol{x})} \tag{4.13}$$

The spatial distribution of l_t is depicted in Figure 4.8.

From this picture, it can be observed that the largest turbulent scales are generally located at the pipe core, where, according to the previous analysis, the velocity is higher than in the rest of the pipe. On the contrary, the smallest turbulent scales are situated in the region close to the pipe walls where the velocity is nearly null.

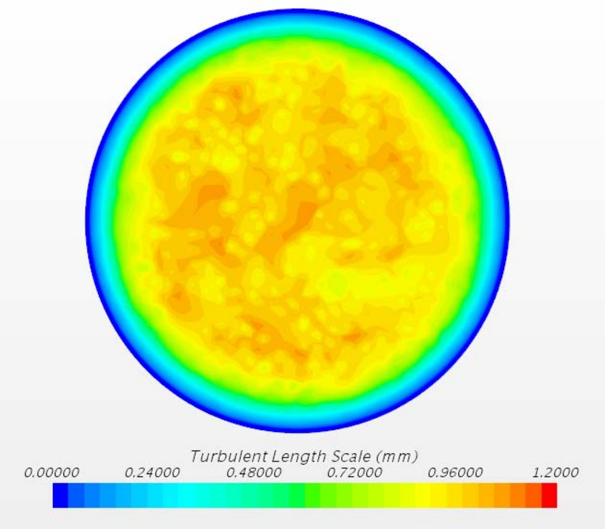

Figure 4.8 Distribution of the turbulent length scale at the pipe outlet

Conclusion

The simulation of the fully developed turbulent flow inside a periodic pipe has been conducted to obtain the velocity and turbulence average distributions which generate when fully developed turbulent flow conditions occur.

The spatial distribution of the average velocity, of the turbulence intensity and of the turbulent length scale were analysed in detail and found to be coherent with the turbulence theory.

All these three distributions will be then applied as inflow conditions at the Venturi inlet section with the aim of reproducing, through the application of the SEM, the realistic turbulent inflow conditions generally required by the LES approach.

The obtained data were exported as table data and then interpolated at the Venturi inlet using three different field functions (their implementation is reported in the *Appendix* section). These three functions were then applied at the inlet of the duct as inflow velocity and turbulence conditions.

However, it must be underlined that, though fully developed turbulent flow conditions have been already assigned to the inlet section, a long inlet pipe must be included in the Venturi geometry to allow the proper development of turbulence.

This method is quite similar to the *Precursor Simulation* method proposed by Sagaut [4] (which is depicted in Figure 4.9), but it is way less expensive than the aforementioned technique even though it seems to be also less accurate.

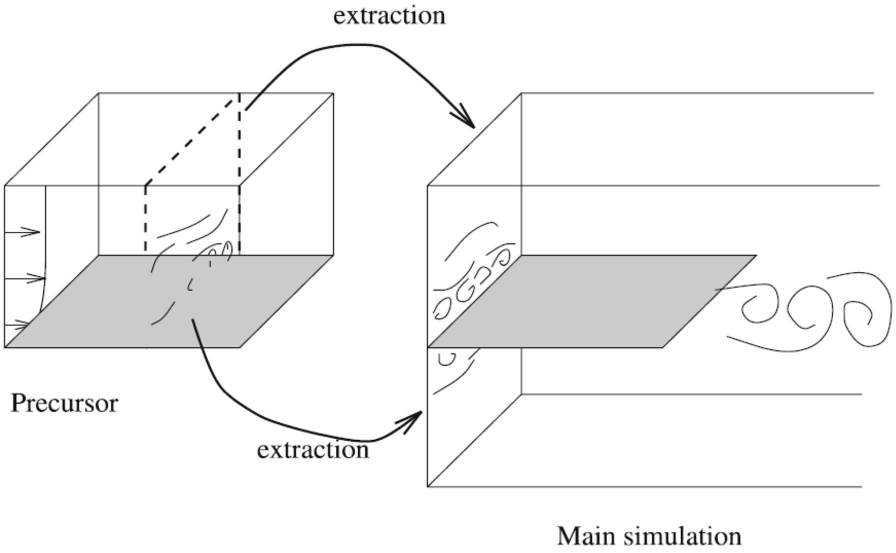

Figure 4.9 Schematic representation of the *Precursor Simulation* method. Picture from Sagaut [4]

As it can be seen observing Figure 4.9, the *Precursor Simulation* approach is based on the extraction of the inflow boundary conditions for the final simulation from a simulation of the upstream flow, called *precursor simulation*. This technique provides an accurate estimation of the inflow turbulent conditions for every time-step. On the other hand, it is really difficult to be applied because it requires the reproduction of the entire history of the flow and this, for complex geometries, requires huge computational costs. Another problem that derives from the use of this approach is that of causality: in fact, the precursor simulation computes the inflow conditions without receiving feedback information from the main simulation. This defines a one-way coupling between the two simulation, which could be problematic when inside the main simulation a signal (such as acoustic waves) is emitted.

As previously said, the method used in the current project to obtain the inflow conditions at the Venturi inlet is, at the same time, less accurate and less expensive than the *Precursor Simulation* technique. These characteristics are due to the fact that, though using a precursor simulation, this approach does not reproduce the instantaneous turbulent field of motion, but only its average velocity and turbulence profiles. This involves no need of reproducing the entire history of the inflow and consequently the computational costs of the simulations can be considerably reduced. It is also worth mention that this method is highly replicable and allows to reproduce almost realistic turbulent inflow conditions in a simple way. It must be also underlined that this new approach provides velocity and turbulence average fields, so its usage is recommended when the SEM technique is applied to generate turbulent conditions at the inlet boundaries.

Further studies can be conducted on this method, even focusing on the influence of the pipe geometric ratio L/D on the results.

4.3.2 Inlet cavitation boundary conditions

As said previously, the adoption of the *VOF* Multi-Phase model to simulate cavitation requires the definition of an additional boundary condition at the Venturi inlet. This BC fixes the amount of water and vapor that enters the simulation domain at each time-step and is defined by the *Volume Fraction* of water/vapor, which can be computed as follows once the seed density n_0 and the seed diameter $d_0 = 2R_0$ are known:

$$\alpha_L = 1 - \alpha_V \tag{4.14}$$

$$\alpha_V = \frac{\frac{4}{3}\pi n_0 \left(\frac{d_0}{2}\right)^3}{1 + \frac{4}{3}\pi n_0 \left(\frac{d_0}{2}\right)^3} \tag{4.15}$$

On the contrary, such a boundary condition is not required at the outlet section. The definition of *Volume Fraction* of water/vapor provided by equations (4.14) and (4.15) was also used to define the initial distribution of both phases along the fluid domain.

4.4 Mesh Set-Up

The mesh set-up plays a crucial role when turbulence is modelled considering scale-resolving methods such as Large Eddy Simulations. This is due to the fact that, to achieve good results when using the implicit LES approach, the grid size must be chosen in order to be included in the inertial subrange of the energy cascade.

In fact, only in this case, the chosen SGS model would be able to work effectively reproducing the effect of the smallest (and so not-resolved) scales thanks to the fact that, inside the inertial subrange, the hypothesis of isotropy and universality of small turbulent scales are valid.

Therefore, the mesh size defines the filtering length Δ, i.e. the size of the eddies that the solver will be able to detect, while eddies with smaller sizes will be modelled by the SGS model.

As seen previously, the Taylor microscale is included in the inertial subrange and so it can be taken as reference for setting-up the mesh size in the whole domain. The use of this type of length scale is also suggested by the User Guide [28] and was used as reference for LES meshing operations by several authors, including Koukouvinis et al. [16].

An estimation of the Taylor length scale can be made using equation (2.36). In fact, considering the throat diameter d as the characteristic lengthscale of the problem, the Reynolds number can be computed as follows:

$$Re_d = \frac{\rho u_0 d}{\mu} \sim 220000 \tag{4.16}$$

Where ρ and μ are respectively the density and the viscosity of the water at 20°C and u_0 is the throat velocity.

From (2.36) follows that, the Taylor microscale estimation at Venturi throat is equal to:

$$\lambda = \sqrt{10} Re_d^{\ -0,5} d = 112 \mu m \tag{4.17}$$

Further investigations were also conducted to estimate the Taylor microscale value in the rest of the fluid domain. Hence, considering the geometry described in section 4.2.1, the steady incompressible flow of water through the Venturi nozzle was simulated using the k-ω turbulence model. This simulation was made considering only the coarse mesh set-up described in Table 4.4 and visualized in Figure 4.10, since the author was only interested in gaining a general idea of the Taylor microscale distribution along the nozzle. For this quick case study, only one refinement including the converging-diverging section was considered. The refinement size was set equal to 1 mm.

Type of mesh	Unstructured
Type of elements	Polygonal
Prism Layer Mesher	Yes

Base Size [mm]	2.0
Number of Prism Layers	8
Prism Layer Stretching Factor	1.2
Prism Layer Total Thickness [m]	$2.0 \cdot 10^{-5}$
Total number of cells	~ 1.64 M

Table 4.4 Principal characteristics and dimensions of the Venturi steady RANS simulation

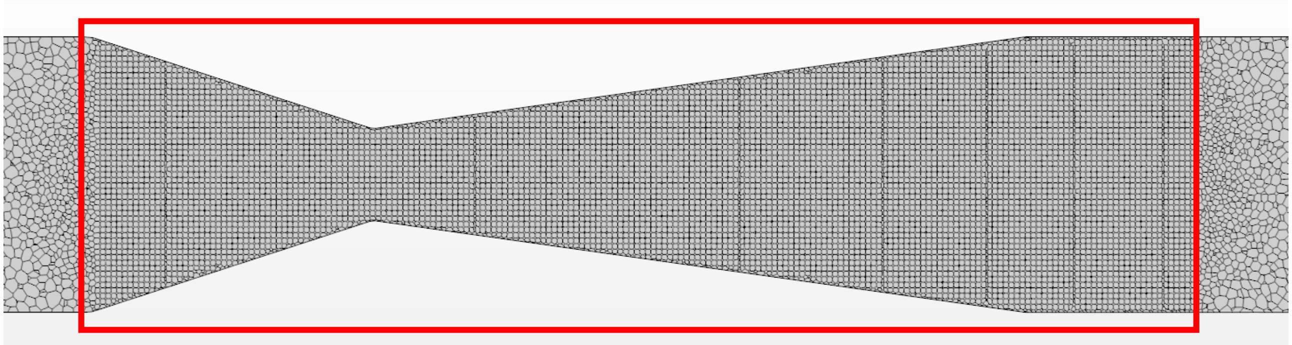

Figure 4.10 XY plane section of the mesh used in the steady RANS simulation of the Venturi. The red box highlights the volumetric refinement of 1 mm size that was set in the converging-diverging region of the duct

At the inlet the *Velocity Inlet* boundary condition was set and a constant velocity profile was imposed with a velocity magnitude of 1.46 m/s. Instead, at the outlet section, the *Pressure Outlet* boundary condition was set and a pressure of 90 kPa imposed. The *Wall* condition was then invoked as boundary condition for the internal surfaces of the nozzle. This way of proceeding is also supported by the *STAR CCM+* User Guide [28], which suggests to run a preliminary RANS (using k-ε or k-ω turbulence models) simulation on an exploratory mesh. Once convergence is reached, the distribution of the *Kolmogorov Length Scale* (the smallest length scale at which viscous dissipation occurs) and of the *Taylor Micro Scale* field functions can be observed in specific *STAR CCM+* scenes.

Then, to construct a good mesh for scale-resolving simulations, such as LES, the User should set-up the mesh in order to have size smaller than the Taylor microscale and larger than the Kolmogorov length scale. These two length scales establish respectively the upper and the lower bounds of the range in which the mesh size must be chosen to obtain good results from LES. This procedure ensures the filtering size (that in ILES coincides with the cell size) to be inside the inertial subrange for all the grid cells.

The Kolmogorov Length Scale and the Taylor Micro Scale distributions along the Venturi are shown in the following pictures (Figure 4.11 and Figure 4.13). Also enlargements in correspondence of the converging-diverging nozzle are reported for the same field functions in Figure 4.3 and 4.5.

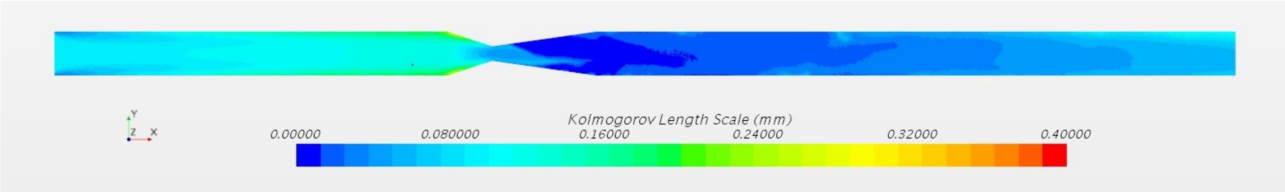

Figure 4.11 Scalar scene displaying the XY plane section of the Kolmogorov length scale distribution obtained from the steady RANS simulation

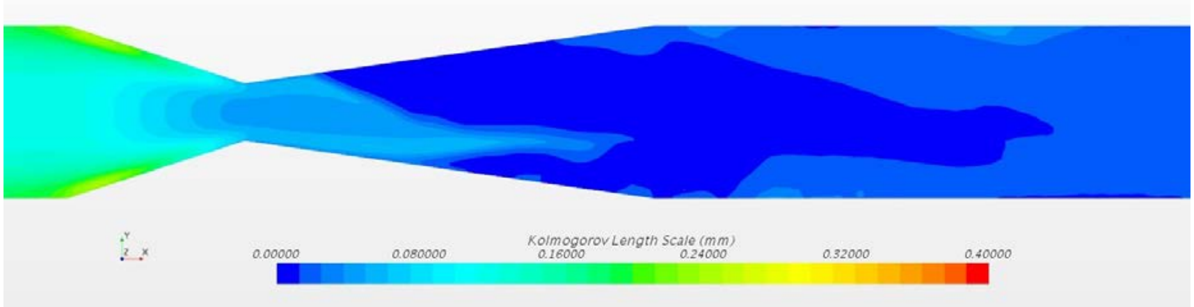

Figure 4.12 Picture showing an enlargement of the previous image (Figure 4.11) in correspondence of the converging-diverging region of the duct

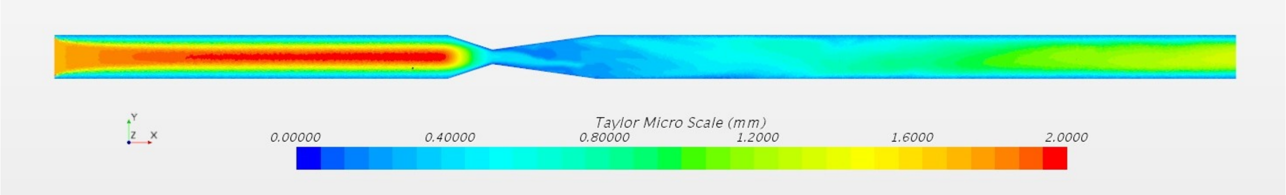

Figure 4.13 Scalar scene displaying the XY plane section of the Taylor microscale distribution obtained from the steady RANS simulation

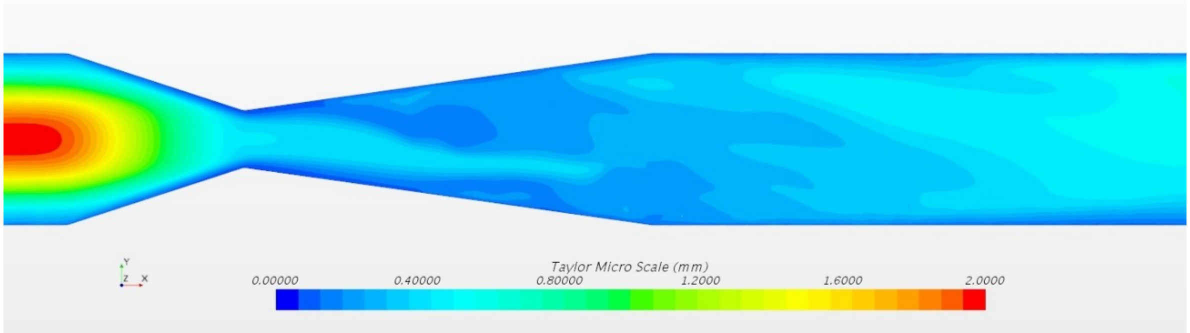

Figure 4.14 Picture showing an enlargement of the previous image (Figure 4.13) in correspondence of the converging-diverging region of the duct

As shown in Figures 4.13 and 4.14, the smallest Taylor microscale values were detected in regions where turbulence intensity is expected to be high, such as near the Venturi walls and inside the diverging nozzle. It is also worth mention that these values of Taylor microscale were found to be compatible with the previous estimation defined by equation (4.17). On the opposite side, the largest values for the Taylor microscale field function have been detected in those flow regions where turbulence intensity is expected to be low, such as in the core of the flow of both the inlet and outlet pipes.

Observing Figure 4.13, it is also possible to appreciate the presence of the *entrance region* before the development of fully developed turbulent flow conditions.

After the observation of Kolmogorov Length Scale and Taylor Micro Scale scenes obtained from the preliminary RANS simulation of the Venturi, we proceeded to the set-up of the computational grid in order to build-up a *polygonal* and *unstructured* mesh with size included between the Kolmogorov length scale and the Taylor microscale.

Pictures of the whole domain mesh set-up and enlargements in correspondence of the Venturi nozzle and the throat are shown in Figure 4.15 – 4.17.

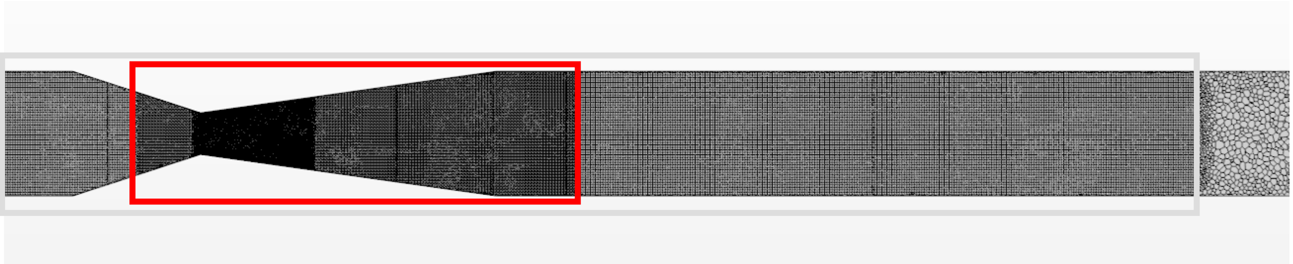

Figure 4.15 Large view of the XY plane section of the mesh used for the validation case. The blue box highlights the first volumetric refinement of 1 mm size, while the red box denotes the second volumetric refinement of 0.6 mm size

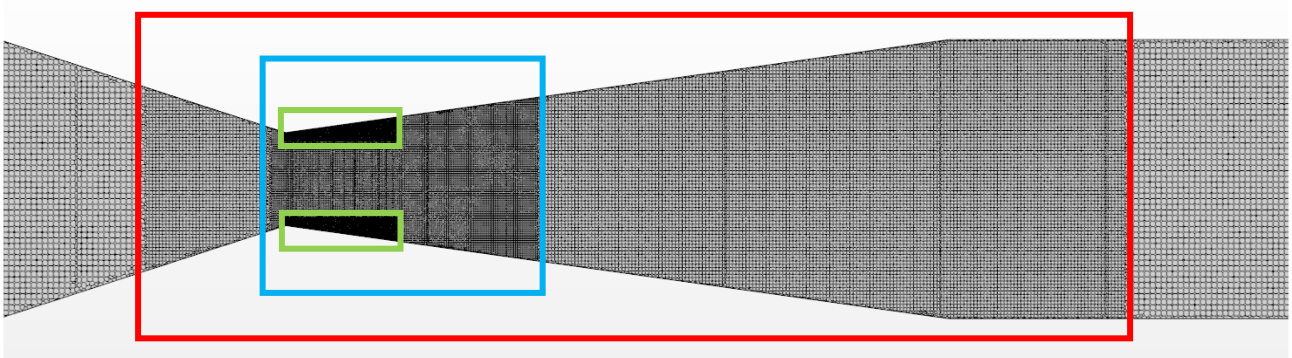

Figure 4.16 Enlargement of the previous image (Figure 4.15). In this picture three volumetric refinements are highlighted: the red box indicates the second volumetric refinement, while the light blue box and the light green box denote respectively the third volumetric refinement (size: 0.3 mm) and the fourth volumetric refinement (size: 0.1 mm)

As it can be seen from these pictures, several different volume refinements were considered in order to keep the scalar function *Volume Change* in the recommended range. This scalar function computes the volume ratio between a cell and its neighbours, giving indications on the cell volume gradients of the mesh. The User Guide [28] suggests to set-up mesh refinements in order to avoid large cell volume gradients and to maintain the Volume Change field function larger than 10^{-3} in sections of interest.

The characteristic dimensions of all the adopted volume block refinements are reported in Table 4.5.

Base Size [mm]	2.0
Total number of cells	~ 18.5 M

Volumetric Refinements	
1st Volumetric Refinement [mm]	1.0
2nd Volumetric Refinement [mm]	0.6
3rd Volumetric Refinement [mm]	0.3
4th Volumetric Refinement [mm]	0.1
5th Volumetric Refinement [mm]	0.05

Table 4.5 Principal dimensions adopted for the validation test mesh

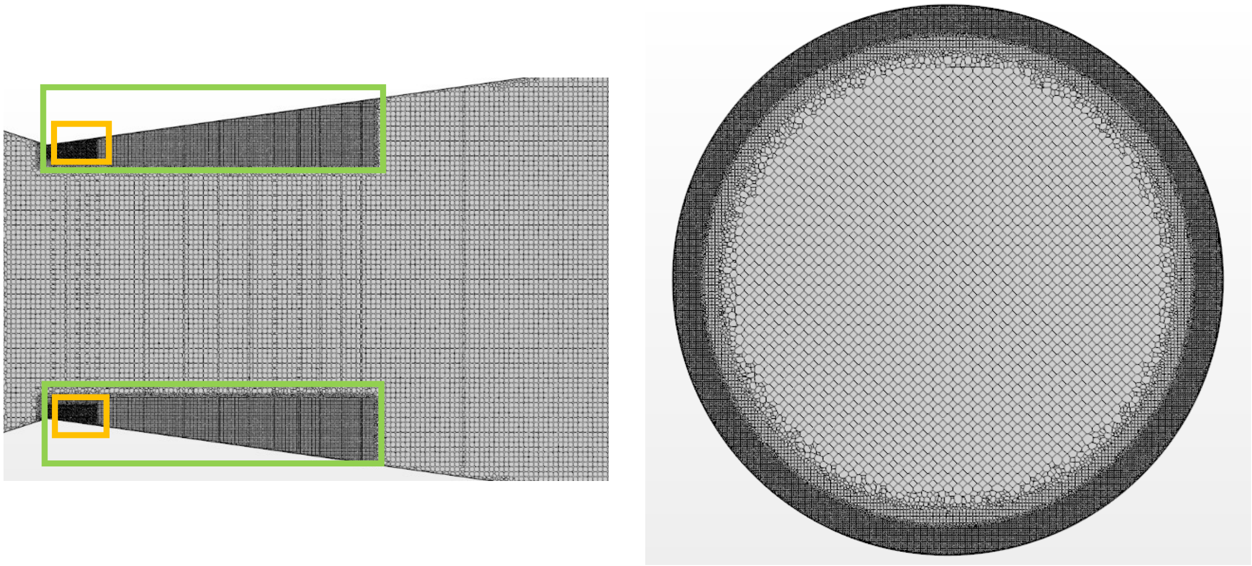

(a) Further enlargement of Figure 4.16. In this picture two different volumetric refinements can be noticed: the light green box indicates the fourth volumetric refinement, while the orange box highlights the fifth and last volumetric refinement (size: 0.05 mm)

(b) Section view of the Venturi throat mesh. Three different refinement regions can be observed, corresponding to the fifth, the fourth and the third volumetric refinements (the order in which these refinements are listed also defines the order of refinement from the duct walls to the duct core)

Figure 4.17 Pictures showing mesh details in correspondence of the converging-diverging nozzle throat

As it can be seen from the observation of this table, the final number of cells required for all the LES simulations are very high and this is due to the fact that the characteristic Reynolds number of the problem is really high too. In fact, when the Reynolds number is very large, the flow is consequently characterized by a high degree of turbulence. This brings to a wide range of turbulent scales involved in the energy cascade process and to the consequent need, for the same 3-D geometry, of finer meshes and a larger number of cells.

To effectively model the three different zones of the turbulent boundary layer (which are viscous sub-layer, buffer layer and logarithmic layer), near-wall mesh is built through the use of the *Prism Layer Mesher* model, which provide the generation of thin prismatic cells orthogonal to the wall surfaces or boundaries. An important parameter which must be considered when using this meshing model is the *non-dimensional wall distance* y^+. This parameter is computed as follows:

$$y^{+} = \frac{u^{*} y}{\nu} \tag{4.19}$$

Where y is the wall distance, ν is the cinematic viscosity and u^{*} is the so-called *friction velocity* and is computed as follows:

$$u^{*} = \sqrt{\frac{\tau_w}{\rho}} \tag{4.20}$$

Where τ_w is the *wall-shear stress* and ρ is the density.

In general, to have a good resolution of the whole turbulent boundary layer, included the viscous sub-layer, y^{+} must be nearly equal to unity ($y^{+} \approx 1$) in the region of interest.

Therefore, this condition sets a constraint on the first cell thickness and since the re-entrant jet mechanism develops exactly close to the wall, it is important to follow this rule to achieve good results.

The prism layer settings, valid for the entire Venturi domain, are briefly listed in Table 4.6, while its geometry is displayed in Figure 4.18.

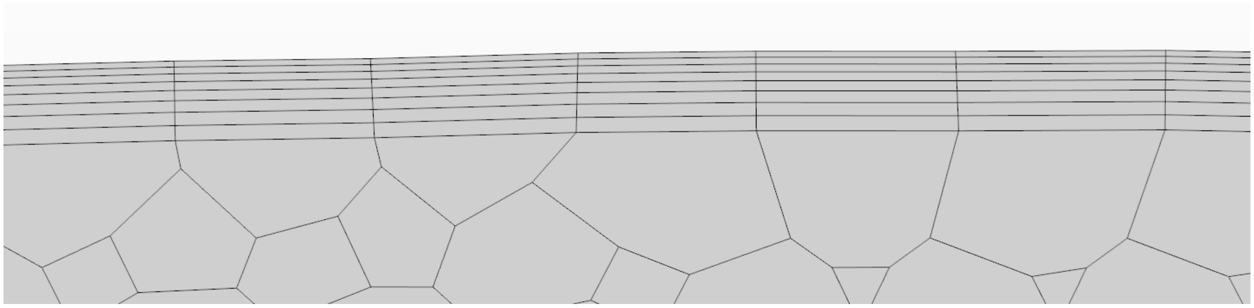

Figure 4.18 Mesh prism layer geometry close to the duct walls

Number of Prism Layers	8
Prism Layer Near-Wall Thickness [m]	$1.5 \cdot 10^{-6}$
Prism Layer Total Thickness [m]	$2.0 \cdot 10^{-5}$

Table 4.6 Principal parameters set to define the prism layer geometry

4.5 Initialization Strategy

In general, it is well known that before starting to collect statistics and data for the post-processing, scale-resolving turbulence methods (such as LES) require to spend a lot of computational time to fully develop all the flow scales.

Moreover, another large part of the computational time is required to "*wash away*" the effects of the initial conditions that were previously set to start the simulation.

So, besides the inflow boundary conditions, also the initialization operations can strongly affect the results which can be obtained from a LES. To overcome this problem, a detailed initialization strategy was implemented.

Since the two aforementioned processes (the fully development of all the turbulent scales and the elimination of the effects of the initial conditions) usually takes from 2 to 5 flow-through cycles to be completed, the *STAR CCM+* User Guide [28] suggests to apply the following points to minimize the number of cycles required before starting colleting statistics:

- Use the results of a RANS calculation to give the right mean field
- Get convergence on a coarse mesh and then interpolate the results onto a fine mesh. Following this procedure, it is possible to preserve the larger scales (which have already developed) while the smaller scales develop quickly.

According to what suggested by the User Guide, the following initialization strategy was adopted for both the simulations of the validation test case:

1) To help the solution in reaching convergence, the flow inside the Venturi nozzle was initialized on a very coarse mesh with the same velocity and pressure fields which were obtained from the steady incompressible single-phase RANS simulation described in Section 4.4. As done before, these initial velocity and pressure field were extracted as table data from the RANS simulation and then imported and interpolated in the main simulation using two new field functions (reported in *Appendix* chapter). Surprisingly, the flow resulting from this steady simulation did not show axisymmetric fields, though the Venturi geometry is axisymmetric. This odd behaviour could be due to the fact that solvers generally struggle to properly simulate flows in metastable conditions (in fact, the incompressible single-phase flow depicted above really cannot occur for the considered set of boundary conditions). Further possible explanations to these strange CFD results were also found consulting the work done

by Zhang [37]. who conducted computational investigations upon the influence of Venturi geometry on the resulting flow fields. In fact, according to this author, the geometry of the Venturi can really affect the flow inside a converging-diverging duct and the so-called *bifurcation* phenomenon occurs especially when the area ratio and the diffusion angle are small, as in our case. Some pictures of the initial velocity and pressure fields obtained from the steady RANS simulation are displayed in Figure 4.19. Going on with the description of the initialization strategy, the initial values for water and vapor fractions were computed using equations (4.14) and (4.15), with $n_0 = 10^{11}\ m^{-3}$ and $d_0 = 5\ \mu m$. Regarding the initial turbulence conditions, both turbulence intensity and turbulent length scale were specified using equations (4.7) and (4.8). For computing these two parameters, the inlet pipe diameter D and the inlet pipe Reynolds number Re_D were taken into account.

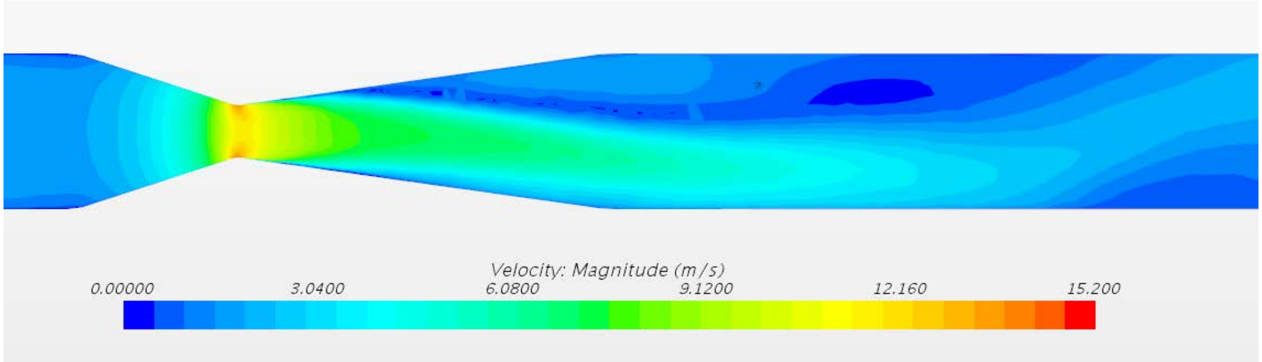

(a) Scalar scene displaying the XY plane section of the velocity flow field obtained from the steady RANS simulation. This picture does not show an axisymmetric distribution of the motion field though the Venturi geometry is axisymmetric

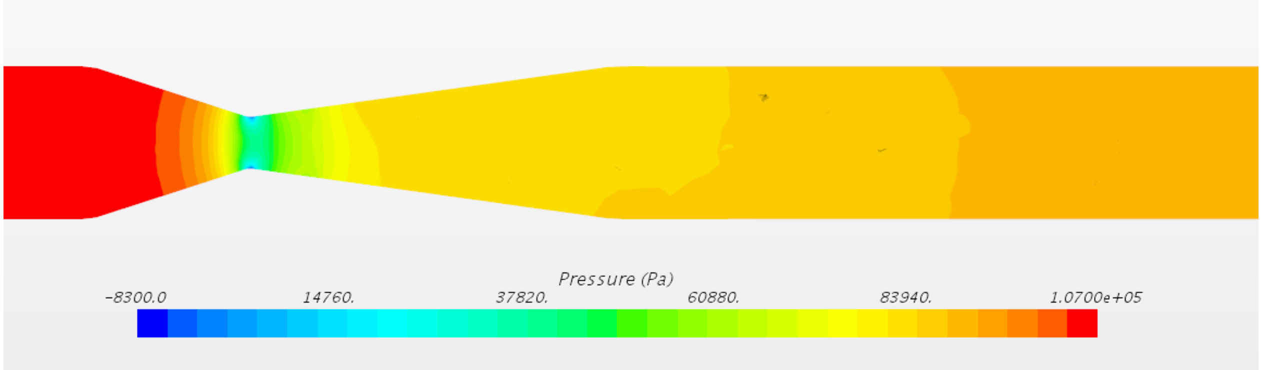

(b) Scalar scene displaying the XY plane section of the pressure field obtained from the steady RANS simulation. Also this picture shows a not-axisymmetric distribution though the geometry is axisymmetric

Figure 4.19 Velocity and pressure field distribution resulting from the steady RANS simulation

2) The simulation started to run on a very coarse mesh set-up using a *Eulerian Second Order* time discretization scheme with a 10 μs time-step. For the first 2 s of simulation, the cavitation model was disabled to further avoid divergence problems. This CFD technique was also applied in his Master Thesis work by Zambon [13] through the use of two additional *User Field Functions*.

   The first one, named *CavitationStart*, sets the value of physical time at which the cavitation model is enabled. In this project, *CavitationStart* was set equal to $\Delta t = 2\ s$ (which allows to simulate nearly two flow through cycles since the whole domain is ~ 1.4 m long and the average Venturi velocity is approximately 1.5 m/s).

   The second User Field Function, simply called *Cavitation*, resets the vapor source term of the cavitation model transport equation until the physical time does not reach the user-defined threshold value stated by *CavitationStart* function. The Field Function *Cavitation* was set as *ScalingFac+* parameter (which is a scaling factor for the source term) in the *Schnerr-Sauer* cavitation model. During this initialization stage, the flow is simulated as a two-phase flow in which the seeds cannot grow and develop into bigger cavities. Hence, the software simulates an approximately single-phase flow. It must be also underlined that *STAR CCM+* allows to use the previously described technique only when the *Schnerr-Sauer* cavitation model is adopted to simulate cavitation. Both these two field functions are reported in the Appendix A.
3) After the activation of the cavitation model, another 0.5 s are simulated using a very coarse mesh set-up and maintaining the same time-step set in the previous initialization step. This second initialization stage was inserted inside the initialization strategy with the aim of softly introducing cavitation and further developing the turbulent scales generated by such a phenomenon.
4) After a physical time of 2.5 s has been reached, the mesh was refined considering the first two volume refinements. Since the grid size was reduced in the regions of interest, also the time-step was lowered to 2.5 μs to fulfil the CFL criterion. This third stage was set to last 0.125 s.
5) After 2.625 s of simulation, the final initialization stage has been reached. The mesh was further refined enabling the three remaining volume refinements. The time-step is set to the final value of 1 μs to respect the CFL condition at the Venturi throat. During this stage, which lasted 85 ms, statistics were collected for the post-processing.

A similar initialization strategy only including successive grid refinements was adopted by Örley et al. [9] for simulating the cavitating flow inside a nozzle using the LES approach. All the four stages of the initialization strategy and their characteristic are briefly reported in Table 4.7.

	1st Stage	**2nd Stage**	**3rd Stage**	**4th Stage**
Physical Time	0 s – 2 s	2 s – 2.5 s	2.5 s – 2.625 s	2.625 s – 2.71 s
1st Volume Refinement	**-**	**-**	**O**	**O**
2nd Volume Refinement	**-**	**-**	**O**	**O**
3rd Volume Refinement	**-**	**-**	**-**	**O**
4th Volume Refinement	**-**	**-**	**-**	**O**
5th Volume Refinement	**-**	**-**	**-**	**O**
Time-step	10 µs	10 µs	2.5 µs	1 µs
Cavitation Model	Disabled	Enabled	Enabled	Enabled
Number of cells	~ 916540	~ 916540	~ 3.92 M	~ 18.5 M

Table 4.7 Brief description of the initialization strategy that was applied during the validation test

Regarding the *Solver*, as reported in the chapter *Model*, the only solver that was compatible with the *VOF* multi-phase model is the *Segregated Flow* solver. For every time-step, the maximum number of inner iterations was set to 10 as it guarantees good convergence and fairly small residuals.

Great attention was also given to the choice of the *Under-Relaxation Factors* (*URFs*) relative to the velocity and pressure fields. The final values for these two simulation parameters are listed in Table 4.8.

Such low value for the Pressure URF was chosen, after being tuned-up, in order to achieve stable solutions.

The *Eulerian Second Order* time discretization was applied in all the simulations of the Thesis Project though the time-step changed over the simulation stages. The choice of running the final simulation stage for 85 ms was made in order to collect a significant number of shedding periods and cycles. It was chosen basing on the expected Strouhal number St_d, which was experimentally found to be equal to 0.375 for $\sigma = 1$ and $p_{out} = 90\ kPa$.

Velocity URF	**Pressure URF**
0.2	0.001

Table 4.8 Under-Relaxation Factors settings used in this Master Thesis project

Chapter 5

Simulations Results

5.1 Validation Criterion

As previously said, this project aims to provide a validated numerical approach to simulate partial cavitation using *Large Eddy Simulation* technique to model turbulence phenomena. To validate the model, it has been decided to compare the shedding frequency value obtained in their experimental tests by Jahangir et al. [46] and Hogendoorn [22] with the value of shedding frequency resulting from our simulations.

To obtain the numerical results concerning the shedding frequency, four *point probes* have been placed at the cardinal points close to the walls of the Venturi throat (see Figure 5.1) and, during the last simulation stage, their vapour fraction time-evolution signal has been recorded. The coordinates of these four points are also listed in table 5.1.

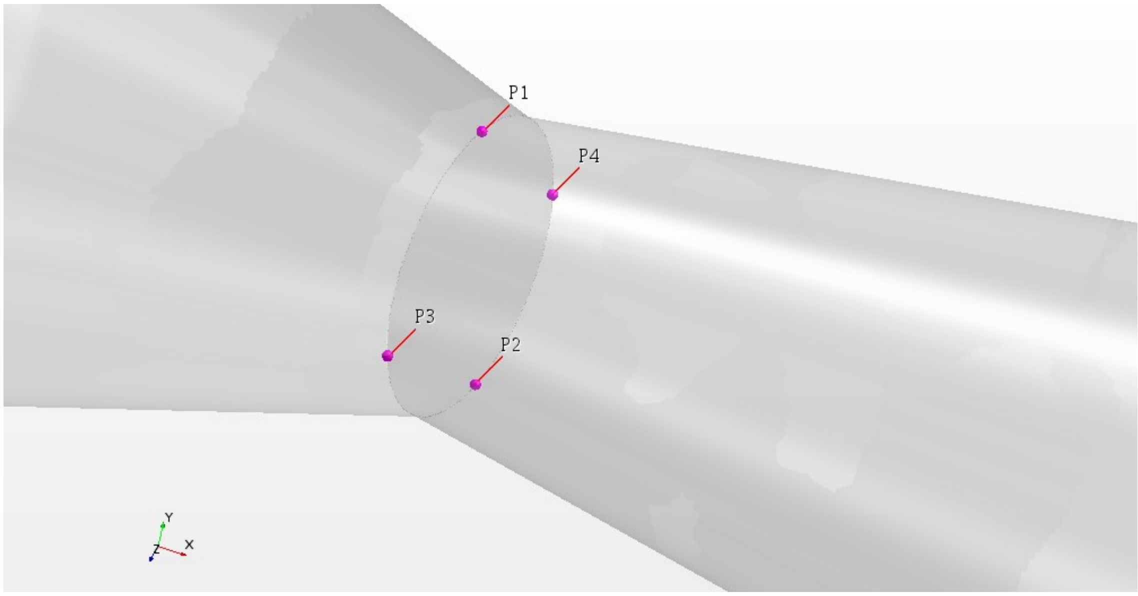

Figure 5.1 3-D picture showing the position of the four point probes

	***x* – coordinate [mm]**	***y* – coordinate [mm]**
Point 1	0	8.33
Point 2	0	-8.33
Point 3	8.33	0
Point 4	-8.33	0

Table 5.1 Coordinates of the four point probes located close to the throat walls

The decision of setting the four point probes in such positions is due to the fact that vapor cavities are expected to develop starting from the Venturi throat.

These technique should also allow to detect the re-entrant jet responsible for the cloud cavitation shedding process: in fact, when the re-entrant jet (that is basically a liquid jet flowing close to the wall in the opposite direction) reaches the throat, causing cavity detachment, a nearly null signal for the vapour fraction time-evolution is expected to be detected in correspondence to the throat.

Once obtained the vapor fraction data, a *Fast Fourier Transform* (*FFT*) operation has been performed to analyse the signal in the frequency domain and the peak frequency resulting from the FFT plot was taken as the resulting shedding frequency of the simulation.

The same method was also applied in Zambon's Master Thesis [13] by considering only one point probe, since the assumption of axisymmetric flow was made in his case.

This way of proceeding was found to be the most appropriate since it allows to effectively detect the shedding frequency of the cloud cavitation process.

To compute the shedding frequency of the cavitation cycle it is also possible to monitor the effective volume of vapor signal, but it was observed by Gorkh et al. [14] that this method is not effective because the physical phenomenon of the periodical cloud cavitation detachment is hidden by the dynamics of the vapor bubbles. In our case, the choice of setting four point probes close to the venturi neck was also made in order to verify if the flow actually was axisymmetric.

Since after performing a FFT operation every spatial information concerning the signal remains lost, also a *space-time* diagram of the vapour fraction signal along the Venturi was taken into account to analyse the cavity length at the time of detachment.

Plane	x – coordinate [mm]
1	0
2	2
3	4
4	6
5	8
6	10
7	12
8	14
9	16
10	18
11	20
12	22
13	24
14	26
15	28
16	30
17	32
18	34
19	36
20	38
21	40
22	45
23	50
24	55
25	60
26	65
27	70
28	75
29	80
30	90
31	100
32	110
33	120

Table 5.2 Coordinates of the section planes probes located close to the throat walls

At first, to re-create this type of diagram, thirty-three section planes orthogonal to the Venturi axis were created along the diverging nozzle starting from the throat (the x-coordinates of all these section planes are listed in Table 5.2) and, for each one of these sections, the maximum vapor fraction time-evolution signal was recorded during the last simulation stage.

Then, the obtained data have been elaborated using *MatLab* to re-construct the *space-time* diagram accounting for the section planes coordinates onto the x-axis (which becomes the *space* axis) and considering the time-evolution signal recorded for each section plane on the y-axis (which becomes the *time* axis).

5.2 Dynamic Smagorinsky

This section reports the results related to the simulation test in which the Dynamic Smagorinsky SGS model was applied. Due to the high computational costs required, in general, by Large Eddy Simulations, we were able to perform only one validation try considering $\sigma = 1$, $p_{out} = 90$ kPa, $n_0 = 10^{11} m^{-3}$ and $d_0 = 5\mu m$.

Once the boundary conditions are set, the average throat and inlet velocities can be computed using equations (4.1) - (4.2). For the current case study, these two parameters were found to be respectively equal to 13.25 m/s and 1.46 m/s. The characteristic Reynolds number of the system is equal to $2.2 \cdot 10^5$ and the flow is turbulent.

Below, some pictures of the Vapor Fraction signal detected by the four point probes and their corresponding FFT plots are reported (see Figures 5.2 – 5.7). Examining all these figures, it can be observed that:

- The four signals are not overlapped (see Figure 5.6): this means that the flow is not perfectly axisymmetric. In particular, P3 detects the lowest signal, while P4 detects the highest signal. This could be due to the mesh conformation or to the Venturi geometry reconstruction. In fact, all the point probes are located close to the Venturi neck, where the gradients are large and very fine mesh is required to well define the spatial distribution of every physical property. Thus, small mesh differencies can bring to large differencies between signals despite the flow is expected to be axisymmetric. Another possible explanation of the lack of axisymmetry is the presence of the turbulence, that plays a crucial role in Large Eddy Simulations and is a physical phenomenon highly non-symmetric.
- All the FFT plots present at least the same clear peak frequency $f = 62.5\ Hz$, that brings to a period of $T = 16.0\ ms$. This means that this model is able to effectively detect the periodic behaviour of the cavitation shedding process, identifying a single principal frequency. P3 signal reports a larger value for the peak frequency (at 175 Hz), but also presents a peak for frequency equal to 62.5 Hz. Therefore, in all the FFT plots, a large concentration of secondary FFT peak can be observed for frequencies nearly equal to 200 Hz (that would bring to a shedding period $T = 5\ ms$).
- Analysing the four Vapor Fraction time evolution plots, a low-frequency periodic behaviour of the partial cavitation process can be noticed, characterized by a frequency $f = 62.5\ Hz$ and by a period consequenly equal to $T = 16.0\ ms$. This low-frequency periodic signal contemporarily matches with a high-frequency signal at lower amplitude, characterized by a frequency $f = 200\ Hz$ and by a period consequenly equal to $T = 5.0\ ms$. This explains the results obtained from the FFT plots. In fact, it is clearly visible how the system periodically pulses approximately every 5 ms.
- The same results were obtained also computing the mean Vapor Fraction signal as the mean of the four point probe signals. This means that, in general, the dynamics of partial cavitation phenomenon occurring inside the Venturi is the same in all the points close to the nozzle neck.

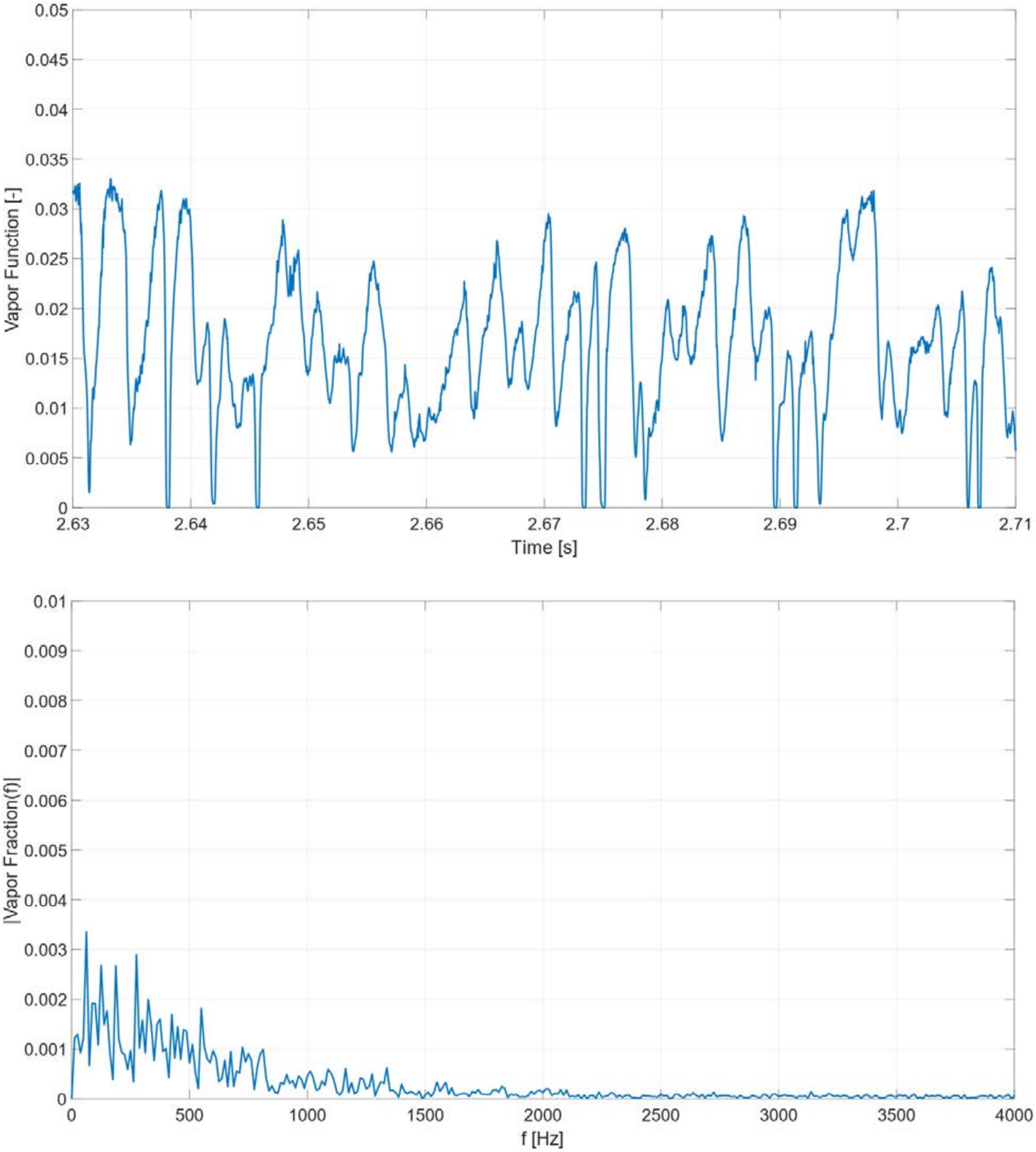

Figure 5.2 Time evolution of the volume fraction of vapor detected by the point probe P1 (*above*) and the spectral analysis (*below*). The test was conducted using the Dynamic Smagorinsky SGS LES turbulence model. The peak frequency was found to be equal to 62.5 Hz, but also a high concentration of secondary peaks can be observed for frequencies close to 200 Hz.

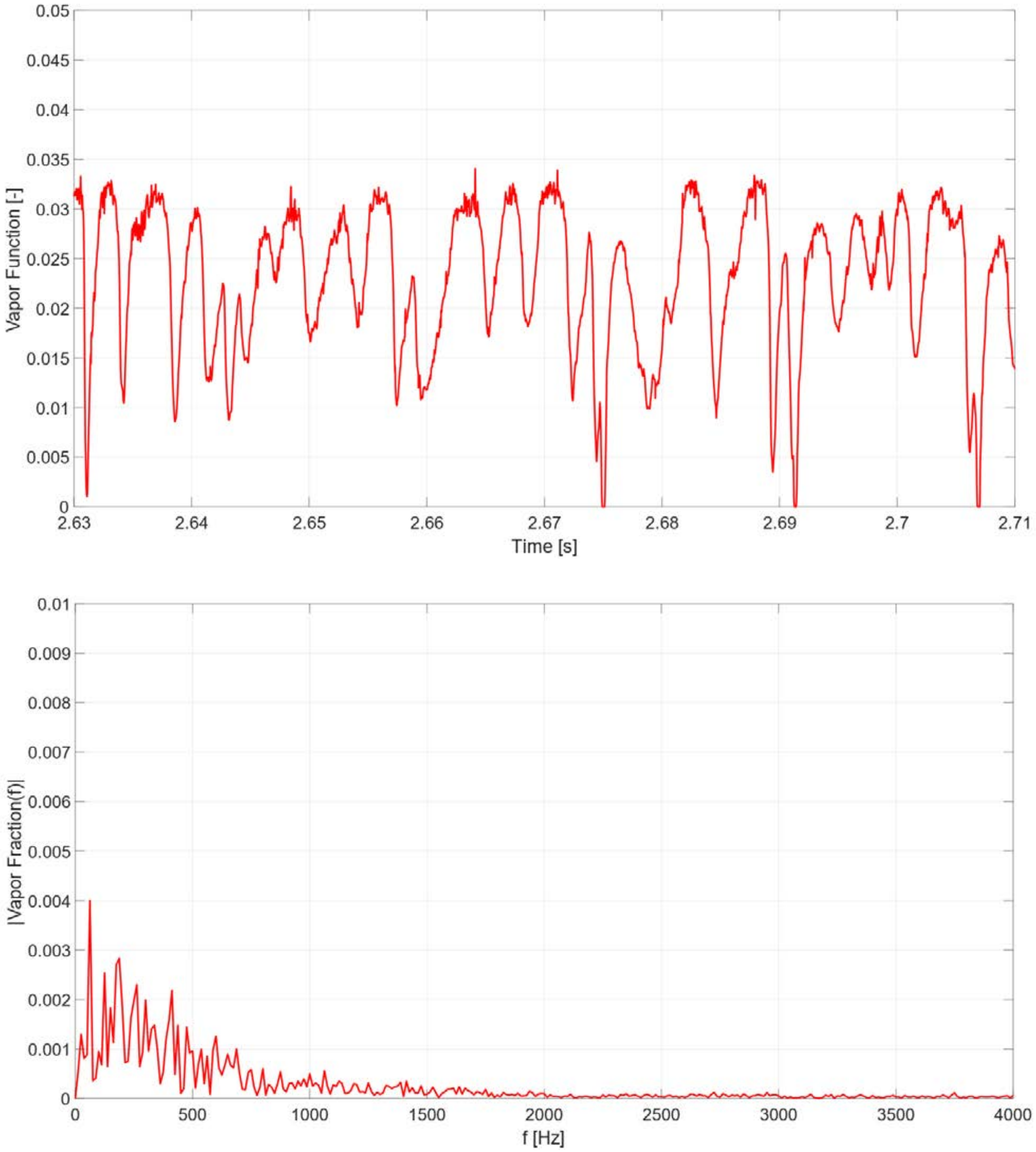

Figure 5.3 Time evolution of the volume fraction of vapor detected by the point probe P2 (*above*) and the spectral analysis (*below*). The peak frequency was found to be equal to 62.5 Hz, with also a high concentration of secondary peaks for frequencies close to 200 Hz.

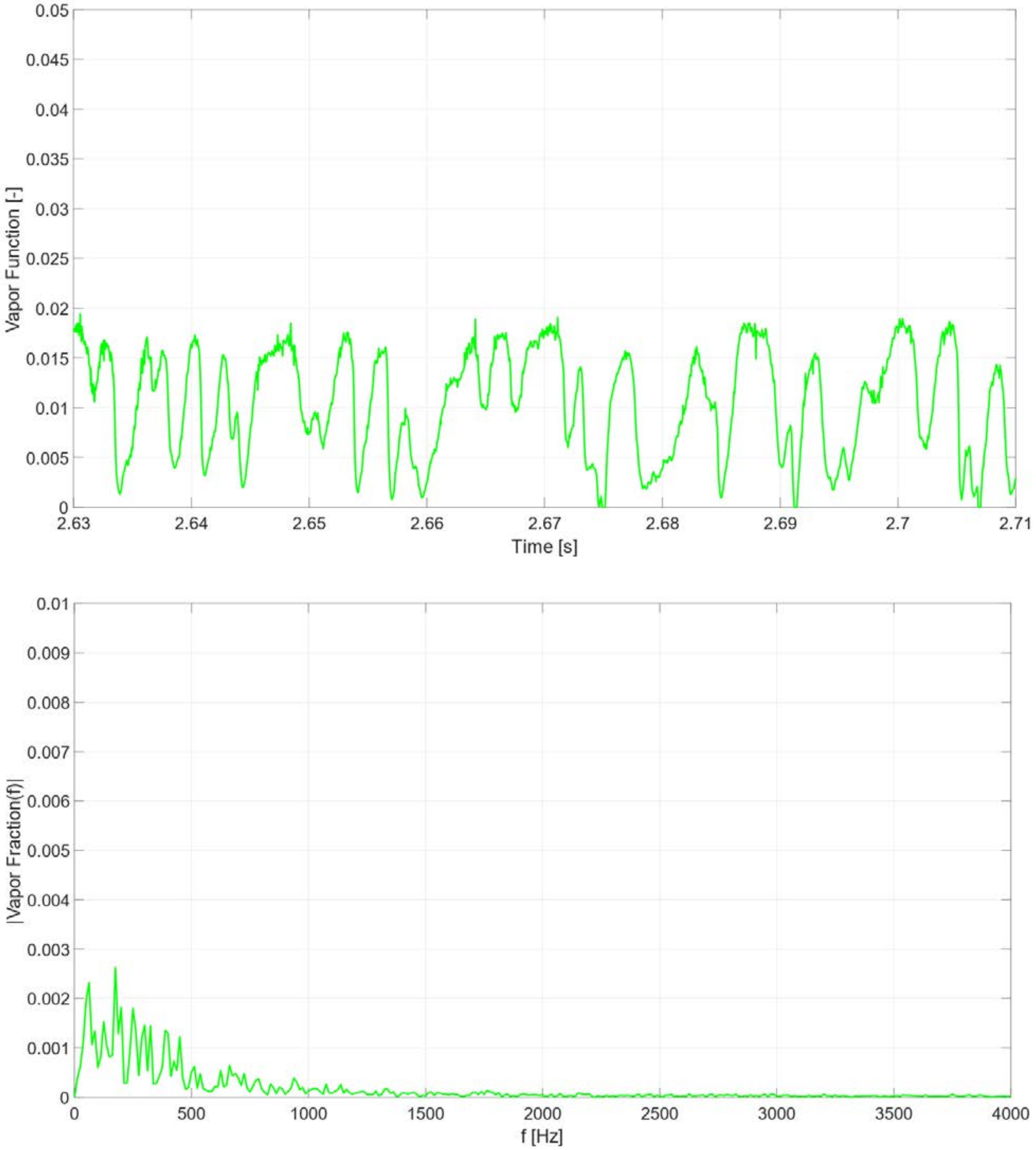

Figure 5.4 Time evolution of the volume fraction of vapor detected by the point probe P3 (*above*) and the spectral analysis (*below*). The peak frequency was found to be equal to 175 Hz, while a secondary peak was observed for a frequency of 62.5 Hz.

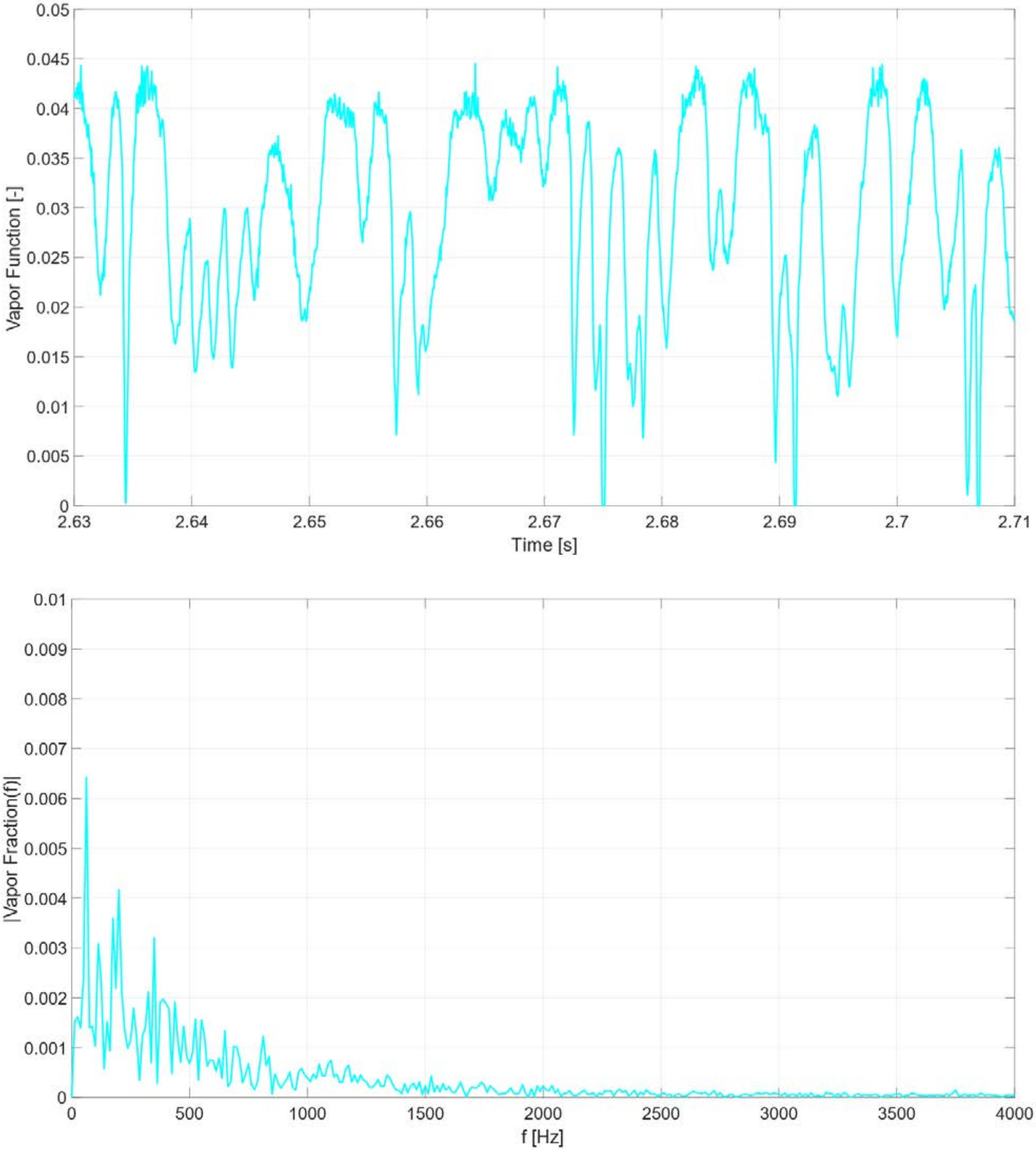

Figure 5.5 Time evolution of the volume fraction of vapor detected by the point probe P4 (*above*) and the spectral analysis (*below*). The peak frequency was found to be equal to 62.5 Hz, with a concentration of secondary peaks for frequencies close to 200 Hz.

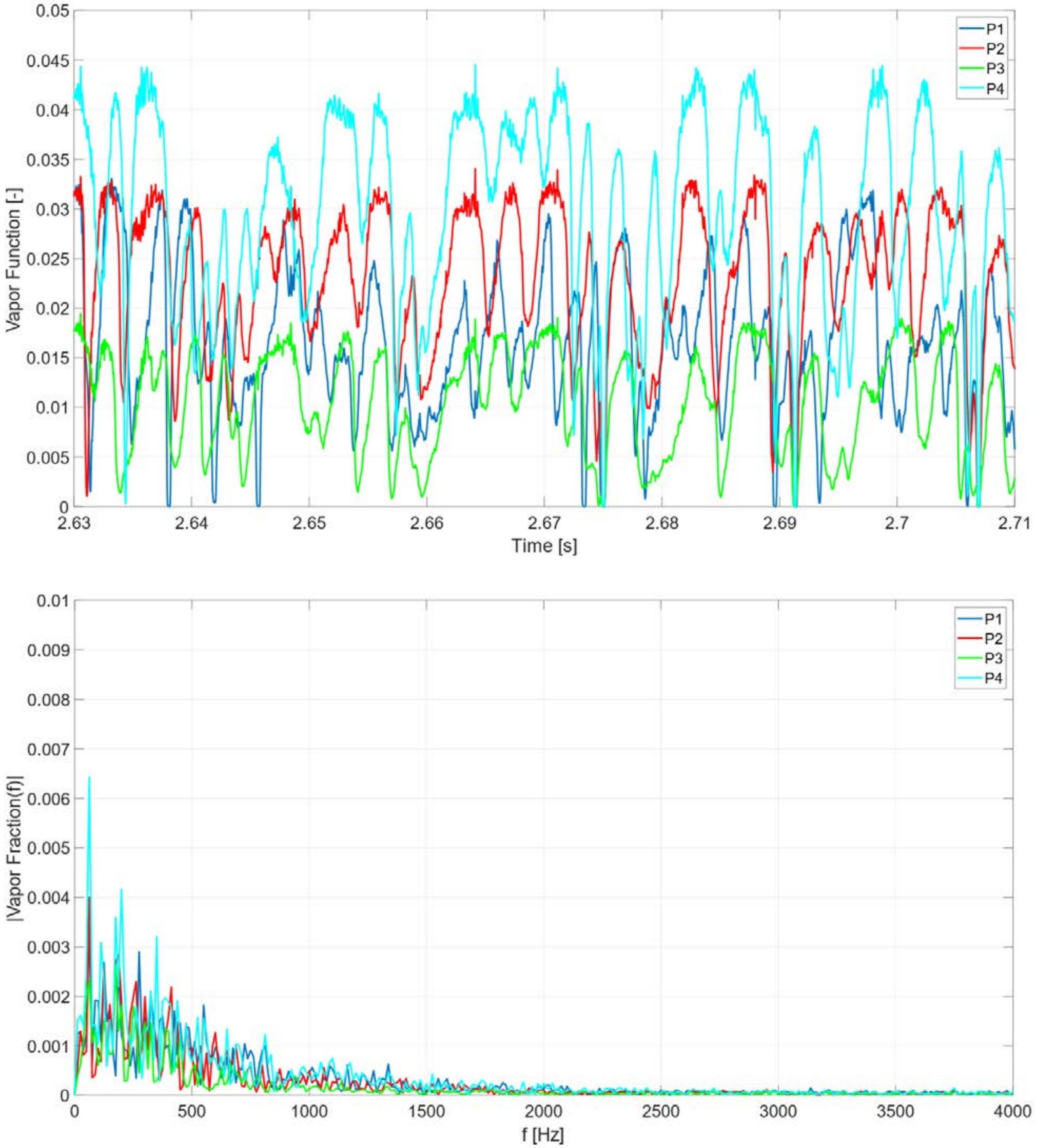

Figure 5.6 Time evolution of the volume fraction of vapor detected by all the four point probes (*above*) and the spectral analysis (*below*). The four signals are not perfectly overlapped and synchronous and this is the sign of not perfectly axisymmetric flow.

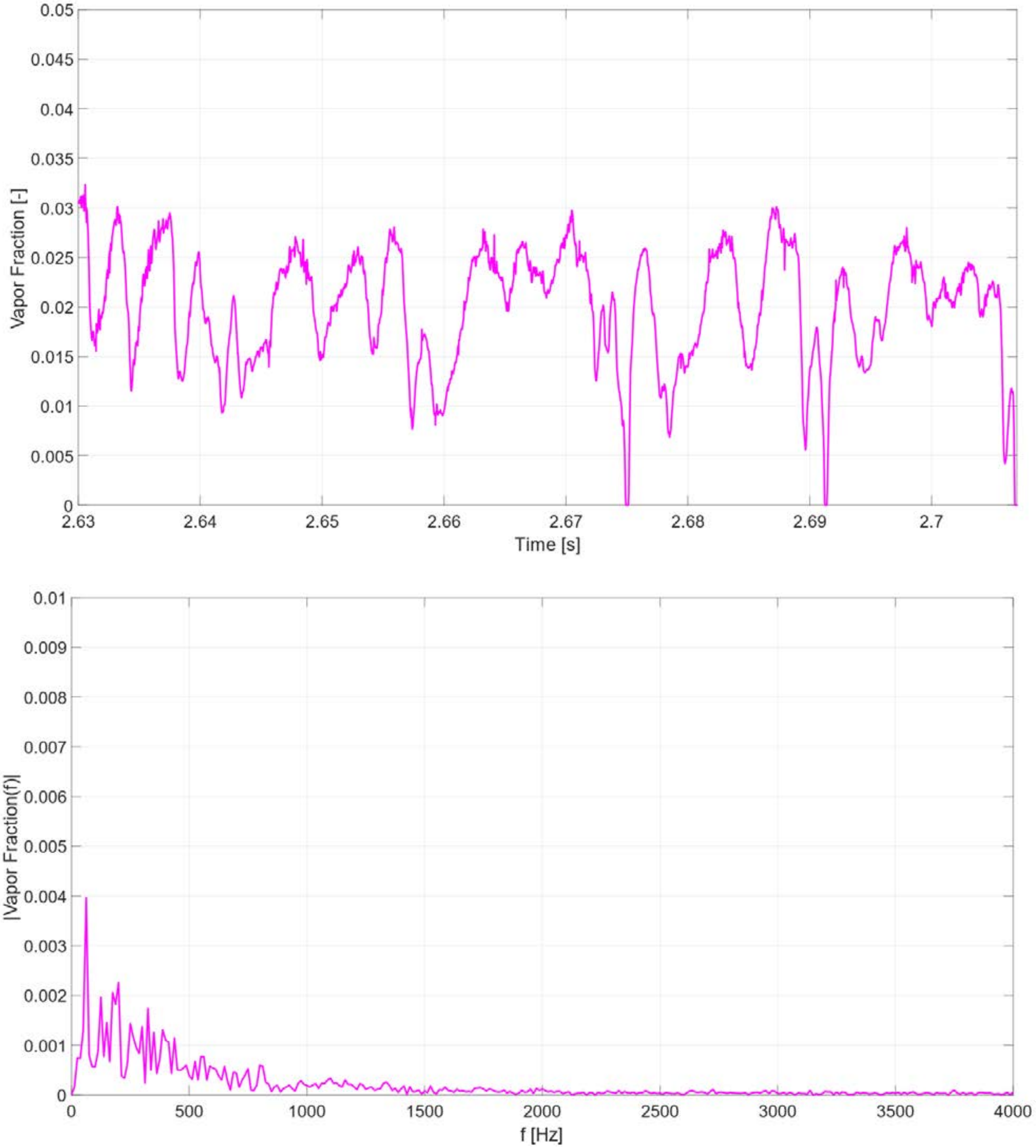

Figure 5.7 Time evolution of the vapor fraction mean signal (*above*) and the spectral analysis (*below*). A peak frequency equal to 62.5 Hz was detected. A high concentration of secondary peaks can be again observed for frequencies of the order of 200 Hz. In the vapor fraction signal plot are clearly visible two shedding cycles of period $T \approx 16\ ms$, but it is also visible how the system periodically pulses approximately every 5 ms.

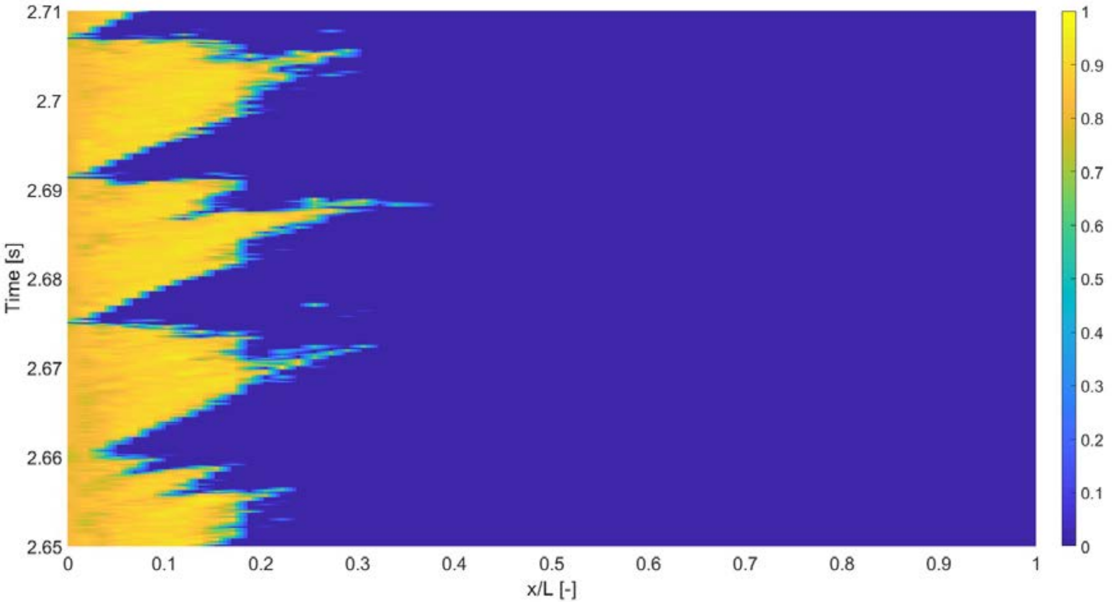

Figure 5.8 X-t diagram of the Vapor Fraction resulting from the Dynamic Smagorinsky simulation. Three different shedding cycles of period $T \approx 16\ ms$ are clearly visible. The x-axis reports the ratio x/L, where L represents the length of the divergent part of the Venturi nozzle. From this picture it can be noticed that the cavity length at the time of detachment is nearly equal to 0.1L. The bubble cloud, once detached from the Venturi throat, is advected downstream and collapses within a maximum distance 0.3L from the nozzle neck.

The peak frequency results obtained from the FFT operations on the four point probe signals are briefly listed in Table 5.3, which also reports the corresponding time period and the Strouhal number for every probe point. Inside the same table, all these parameters are also reported for the mean Vapor Fraction signal, which was computed as the mean of the four signals. Therefore, the x-t diagram, portrayed in Figure 5.8, confirms the periodic behaviour of the cavitation process, showing that cavity detachment occurs approximately every 16 ms. Observing this picture, it is also possible to notice that the cavity length at the time of detachment is nearly equal to 0.175L (where L indicates the length of the diverging part of the Venturi nozzle).

	$f^I\ [Hz]$	$f^{II}\ [Hz]$	$T^I\ [ms]$	$T^{II}\ [ms]$	St_d^I	St_d^{II}
P1	62.5	275	16.0	3.64	0.0786	0.346
P2	62.5	187.5	16.0	5.33	0.0786	0.236
P3	175	62.5	5.71	16.0	0.220	0.0786
P4	62.5	200	16.0	5.0	0.0786	0.251
Mean	62.5	200	16.0	5.0	0.0786	0.251

Table 5.3 Shedding frequencies and derivative parameters resulting from the Dynamic Smagorinsky test. f^I denotes the principal peak frequency detected in the corresponding FFT plot, while f^{II} denotes the secondary peak frequency.

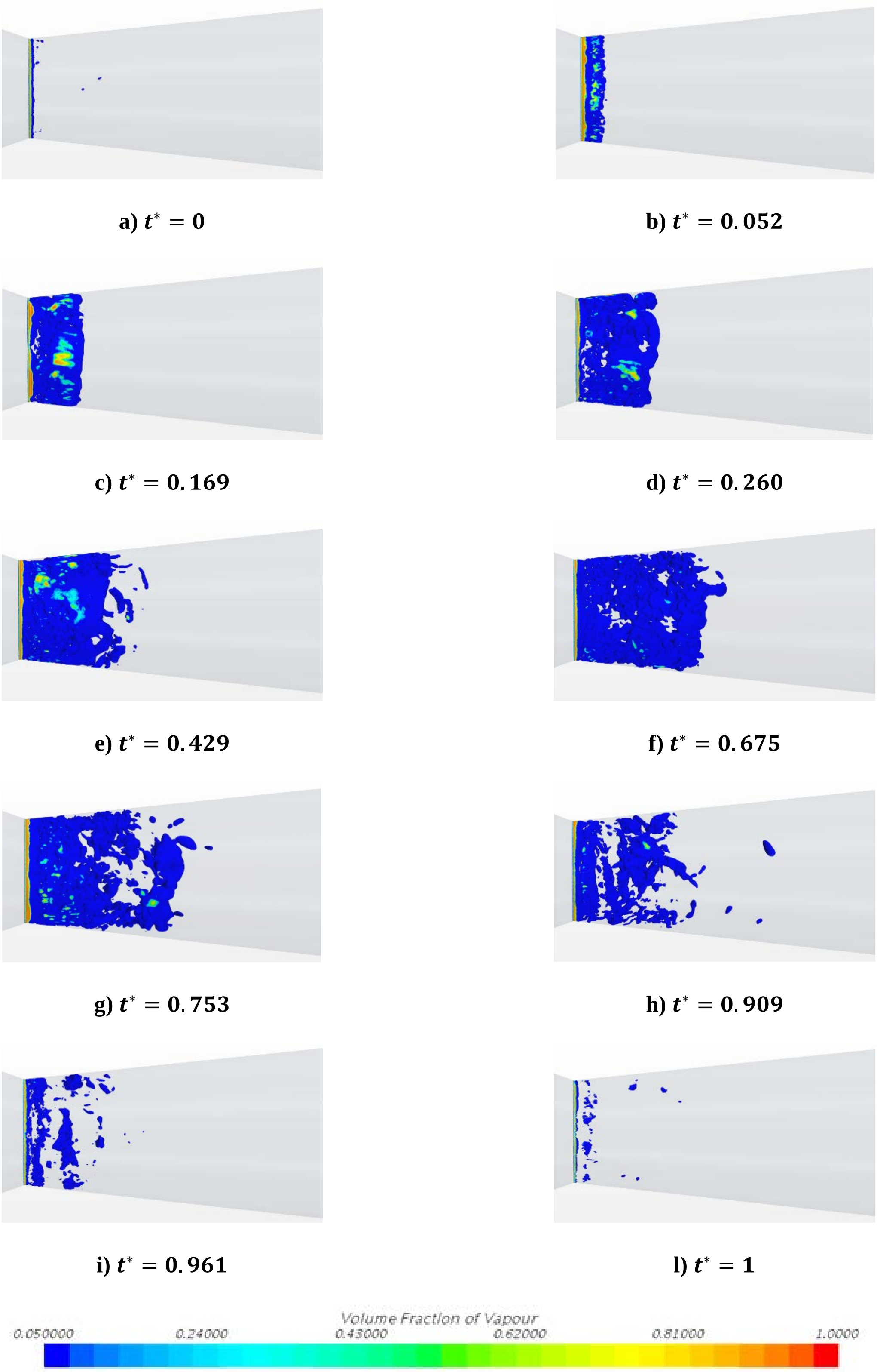

a) $t^* = 0$ **b) $t^* = 0.052$**

c) $t^* = 0.169$ **d) $t^* = 0.260$**

e) $t^* = 0.429$ **f) $t^* = 0.675$**

g) $t^* = 0.753$ **h) $t^* = 0.909$**

i) $t^* = 0.961$ **l) $t^* = 1$**

Figure 5.9 Pictures showing the shedding cavitation cycle reproduced by the Dynamic Smagorisnky simulation ($t^* = t/T$, with $T = 16.0\ ms$). In all the figures, the iso-surface for Vapor Fraction = 0.05 is reported. All the views were taken observing the system from the z-axis.

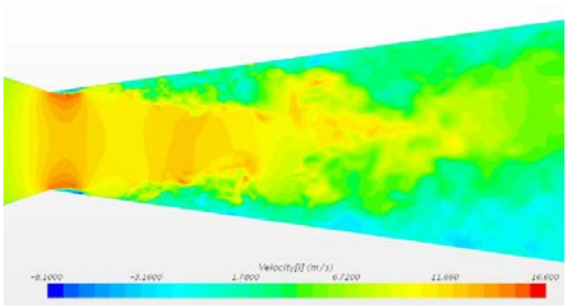

a) Scalar scene reporting the *XY* plane section of the *x*-velocity field for the Dynamic Smagorinsky simulation. It is possible to notice the presence of the re-entrant jet. It is also visually confirmed that the average throat velocity is nearly 13 m/s.

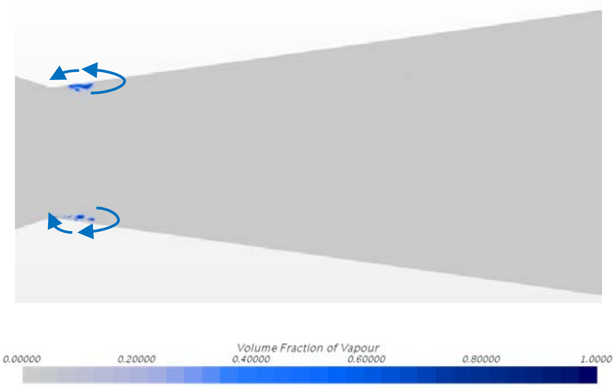

b) Scalar scene reporting the *XY* plane section of the Vapor Fraction field for the Dynamic Smagorisnky simulation. The arrows highlight the presence of the re-entrant jet.

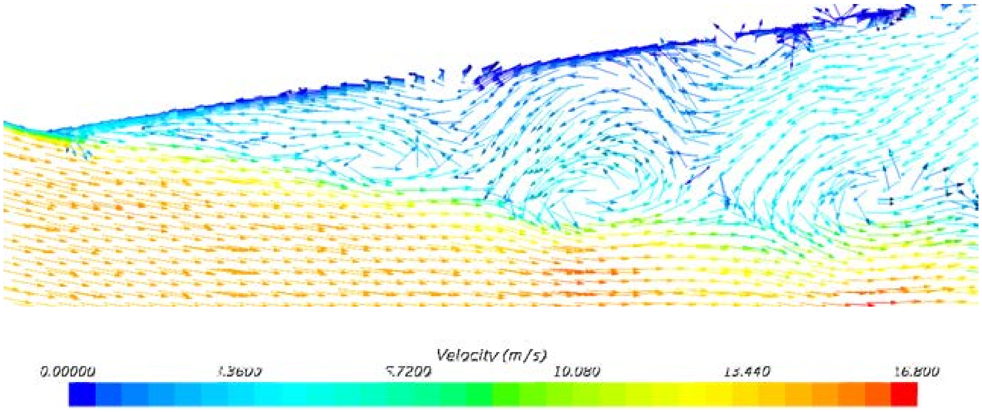

c) Vector scene reporting the *glyph* distribution of the velocity field close to the throat walls for the Dynamic Smagorisnky simulation. This view refers to the *XY* plane section of the Venturi. The magnitude of the re-entrant jet velocity is of the same order of the throat free stream velocity, as reported by Knapp [55].

Figure 5.10 Scalar and vector scenes highlighting the presence of the re-entrant jet during the Dynamic Smagorinsky simulation. All these pictures refer to *XY* plane sections of the Venturi nozzle.

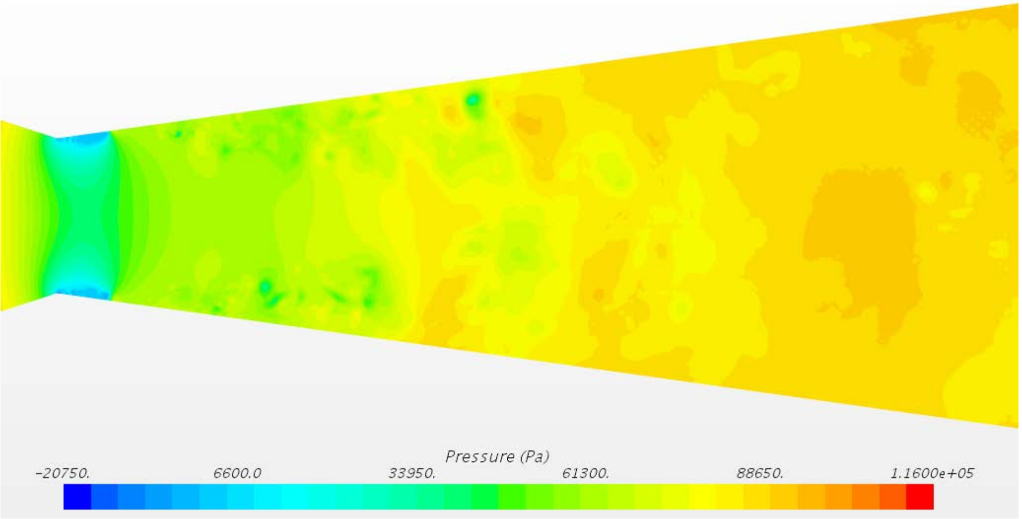

Figure 5.11 Scalar scene of the pressure *XY* plane section from the Dynamic Smagorinsky simulation.

Finally, several pictures of the Velocity and Pressure distributions along the Venturi are presented. In particular, observing Figure 5.10, it is possible to notice the presence of the re-entrant jet developing close to the Venturi walls from the cavity closure region to the nozzle throat, flowing in the opposite direction with respect to the main flow.

Examining the Pressure field depicted in Figure 5.11, the presence of negative values for the absolute pressure could sound very odd at first glance, but it can be easily explained considering the incompressibility assumption made for modelling both water and water vapor.

In fact, the hypothesis of incompressible fluid implies that Pressure appears inside the momentum conservation equation only in the form of pressure gradients and consequently, only pressure differences are important in the solution of the incompressible Navier-Stokes equations.

Therefore, the absence of an equation of state (not required for incompressible fluids) that constraints the pressure to be positive allows this physical quantity to assume also negative values. They have no significance from the physical point of view, but they allow to fulfil the pressure gradient condition stated by the governing equations of incompressible fluid dynamics.

5.3 WALE

This section reports the results related to the simulation test in which the WALE SGS model was applied. As in the case of the Dynamic Smagorinsky simulation, we were able to perform only one validation try considering $\sigma = 1$, $p_{out} = 90$ kPa, $n_0 = 10^{11} m^{-3}$ and $d_0 = 5 \mu m$.

Having set the same boundary conditions of the previously described Dynamic Smagorinsky simulation, the average throat and inlet velocities are respectively equal to 13.25 m/s and 1.46 m/s once again and the characteristic Reynolds number of the system is equal to $2.2 \cdot 10^5$: the flow is turbulent. Below, some pictures of the Vapor Fraction signal detected by the four point probes and their corresponding FFT plots are reported (see Figures 5.12 – 5.17). Analysing all these figures, it can be observed that:

- The four signals are once again not overlapped (see Figure 5.16): this means that the flow is not perfectly axisymmetric. Probe point P3 detects the lowest signal, while P4 detects the highest signal. This could be due to the same reasons that has been already described in the previous Dynamic Smagorinsky simulation results section.
- All the FFT plots present at least the same clear peak frequency (59.5 Hz). This means that this model is able to effectively detect the periodic behaviour of the cavitation shedding process, identifying a single principal frequency. P4 signal reports a larger value for the peak frequency (297.6 Hz, close to the reaults obtained by Hogendoorn [22] and Jahangir et al. [46], but also presents a peak for frequency equal to 59.5 Hz.
- In all the FFT plots, a large concentration of secondary FFT peak can be observed for frequencies nearly equal to 300 Hz, which is the shedding frequency observed in their experimental tests by Hogendoorn [22] and Jahangir et al. [46] for the same set of boundary conditions adopted in this project.
- Analysing the four Vapor Fraction time evolution plots, a low-frequency periodic behaviour of the partial cavitation process can be noticed, characterized by a frequency $f = 59.5\ Hz$ and by a period consequenly equal to $T = 16.8\ ms$. This low-frequency periodic signal contemporarily matches with a high-frequency signal at lower amplitude, characterized by a frequency $f = 300\ Hz$ and by a period consequenly equal to $T = 3.33\ ms$. This explains the results obtained from the FFT plots.
- The same results were obtained also computing the mean Vapor Fraction signal as the mean of the four point probe signals. This means that, in general, the dynamics of partial cavitation phenomenon occurring inside the Venturi is the same in all the points close to the nozzle neck.

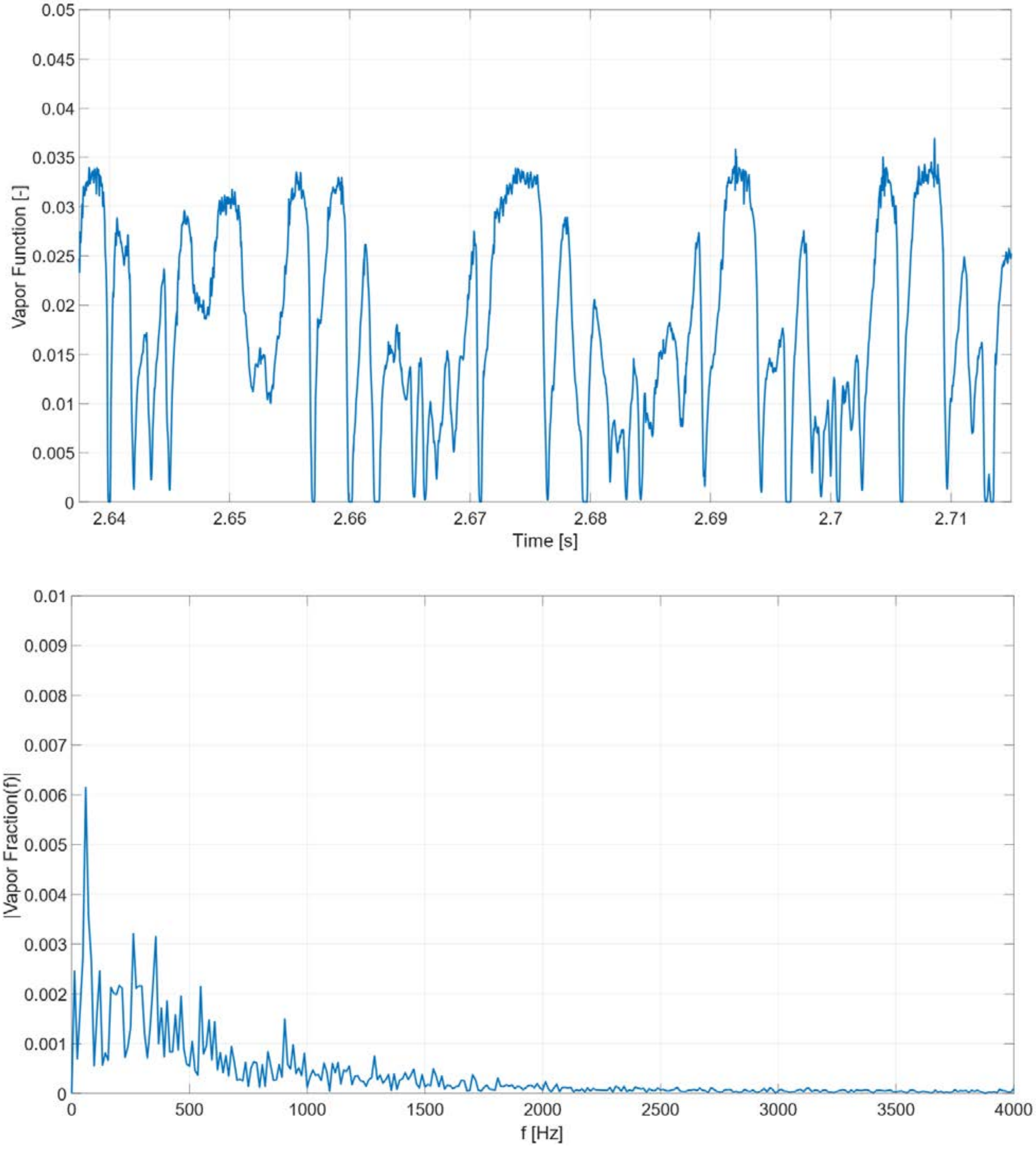

Figure 5.12 Time evolution of the volume fraction of vapor detected by the point probe P1 (*above*) and the spectral analysis (*below*). The test was conducted using the WALE SGS LES turbulence model. The peak frequency was found to be equal to 59.5 Hz, but also a high concentration of secondary peaks can be observed for frequencies close to 300 Hz.

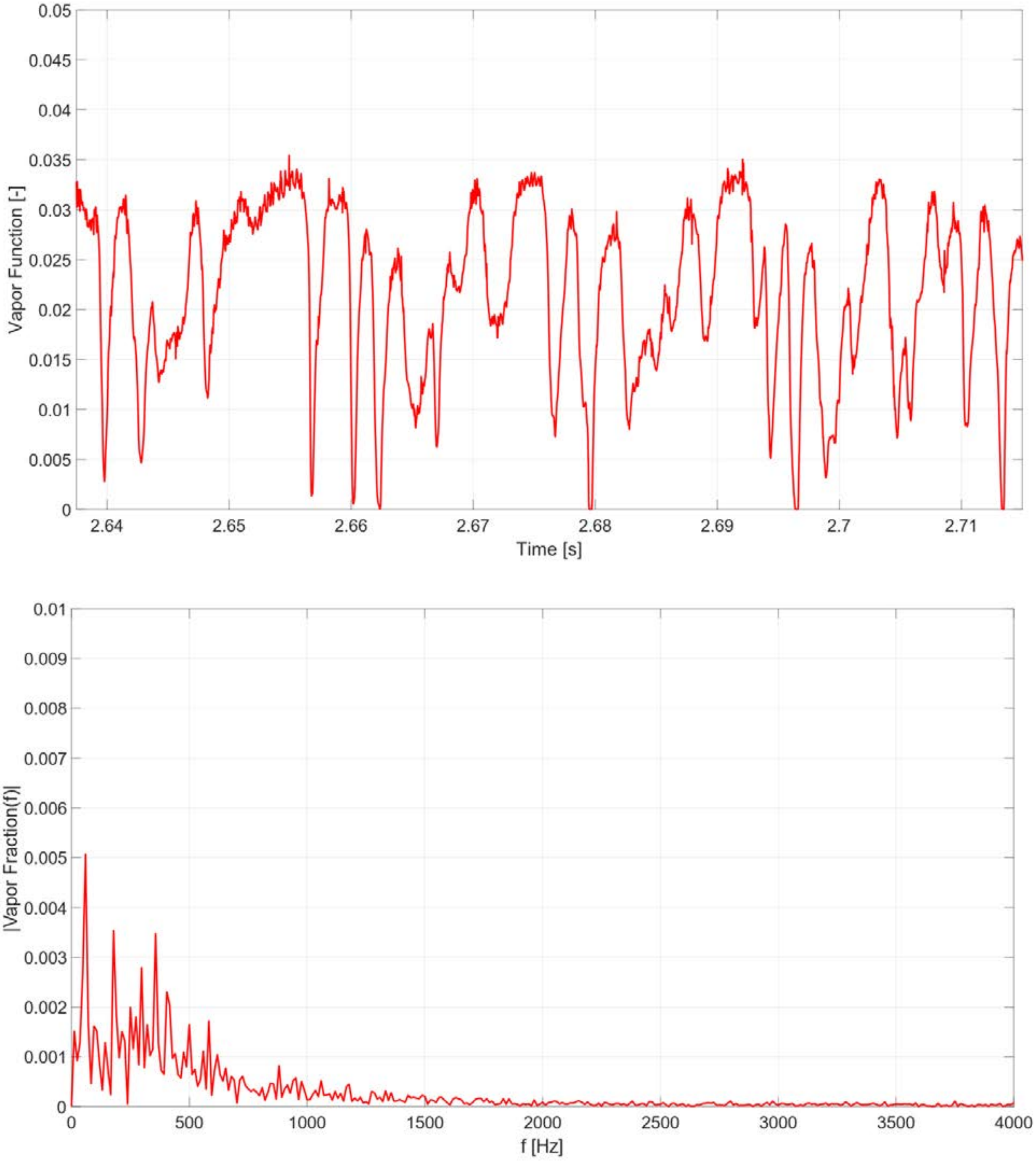

Figure 5.13 Time evolution of the volume fraction of vapor detected by the point probe P2 (*above*) and the spectral analysis (*below*). The peak frequency was found to be equal to 59.5 Hz, with also a high concentration of secondary peaks for frequencies close to 300 Hz.

Figure 5.14 Time evolution of the volume fraction of vapor detected by the point probe P3 (*above*) and the spectral analysis (*below*). The peak frequency was found to be equal to 59.5 Hz, while a secondary peak was observed for a frequency of 178.6 Hz.

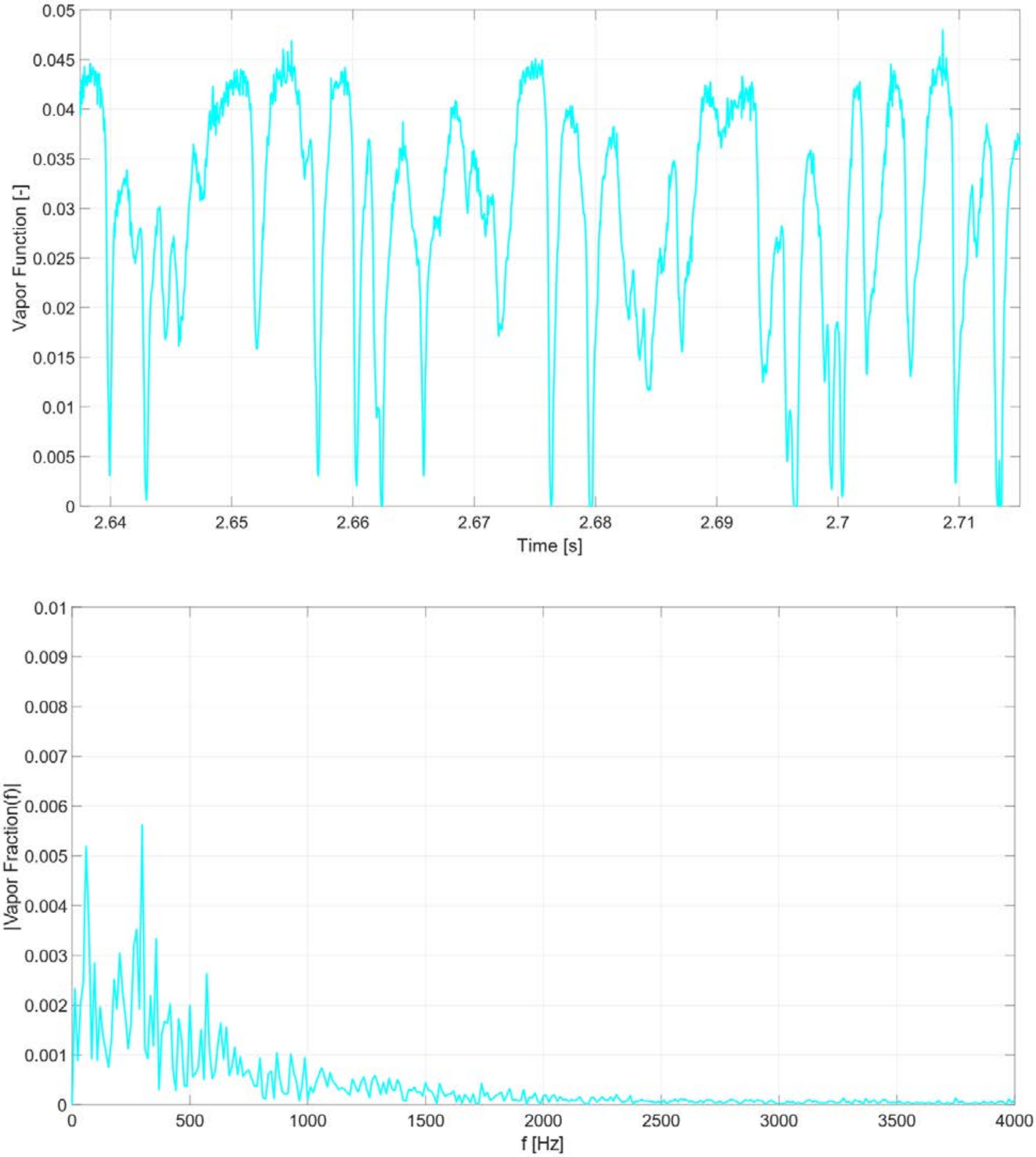

Figure 5.15 Time evolution of the volume fraction of vapor detected by the point probe P4 (*above*) and the spectral analysis (*below*). The peak frequency was found to be equal to 297.6 Hz, with a secondary peak frequency equal to 59.5 Hz.

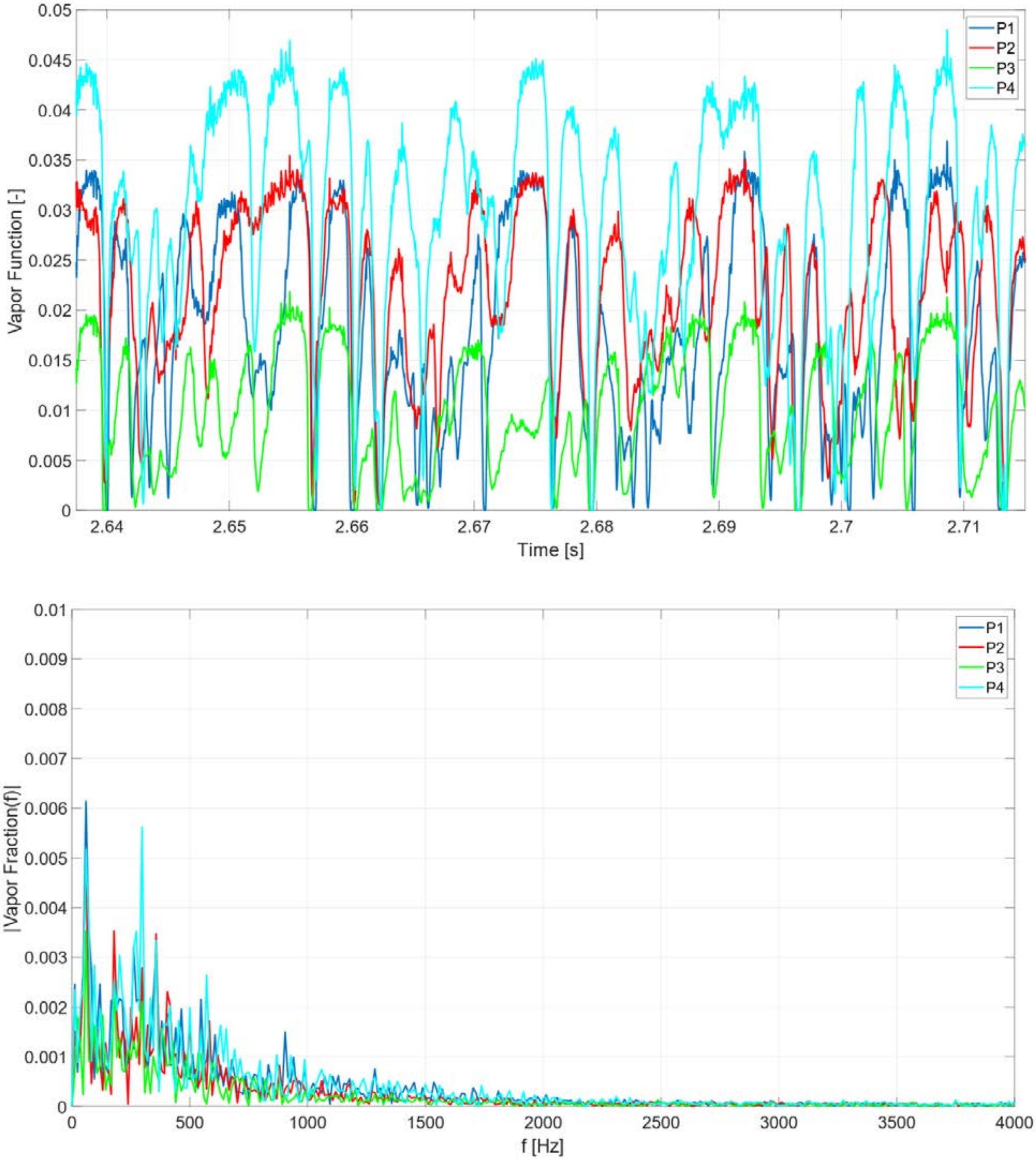

Figure 5.16 Time evolution of the volume fraction of vapor detected by all the four point probes (*above*) and the spectral analysis (*below*). The four signals are not perfectly overlapped and synchronous and this is the sign of not perfectly axisymmetric flow.

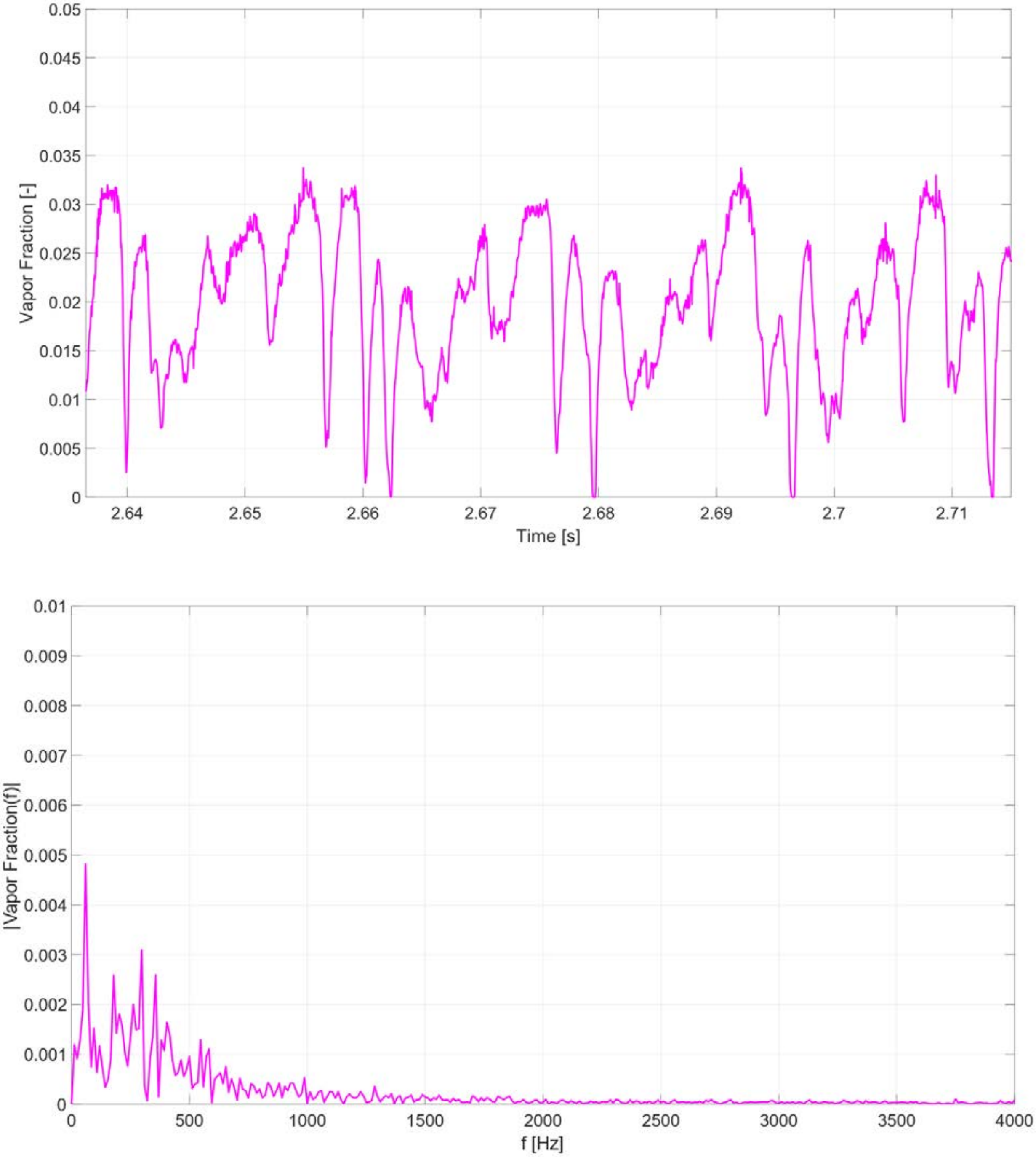

Figure 5.17 Time evolution of the vapor fraction mean signal (*above*) and the spectral analysis (*below*). A peak frequency equal to 59.5 Hz was detected. A high concentration of secondary peaks can be observed for frequency of the order of 300 Hz. In the vapor fraction signal plot are clearly visible three shedding cycles of period $T \approx 17\ ms$.

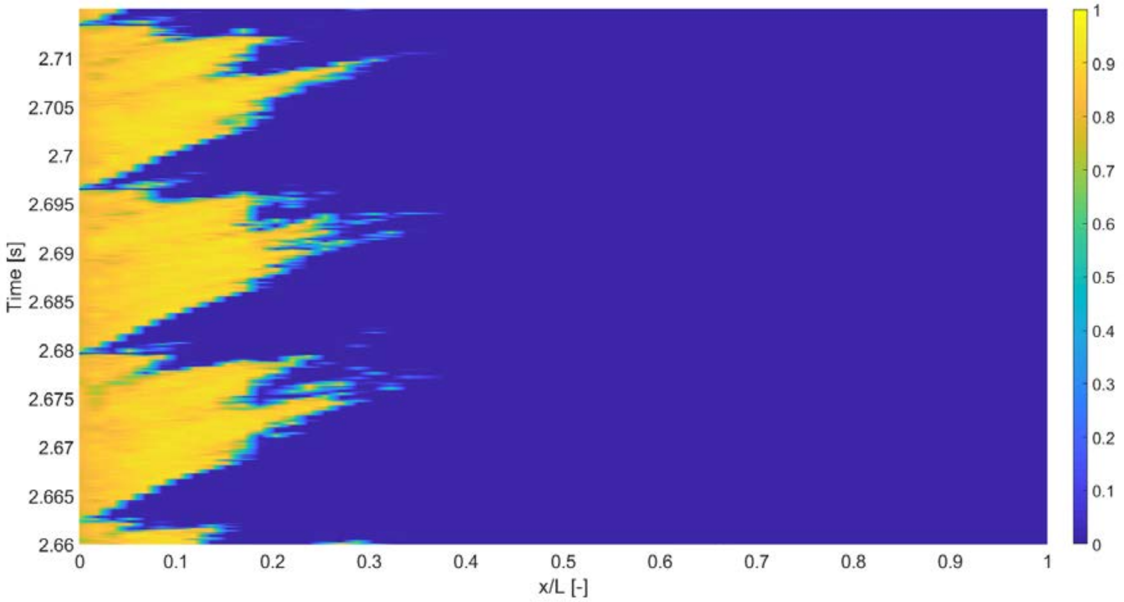

Figure 5.18 X-t diagram of the Vapor Fraction resulting from the *WALE* simulation. Three different shedding cycles of period $T \approx 17\ ms$ are clearly visible. The x-axis reports the ratio x/L, where L represents the length of the divergent part of the Venturi nozzle. From this picture it can be noticed that the cavity length at the time of detachment is nearly equal to 0.1L. The bubble cloud, once detached from the Venturi throat, is advected downstream and collapses within a maximum distance 0.3L from the nozzle neck.

The peak frequency results obtained from the FFT operations on the four point probe signals are briefly listed in Table 5.4, which also reports the corresponding time period and the Strouhal number for every probe point. Inside the same table, all these parameters are also reported for the mean Vapor Fraction signal, which was computed as the mean of the four signals. Therefore, the WALE simulation x-t diagram, portrayed in Figure 5.18, confirms the periodic behaviour of the cavitation process, showing that cavity detachment occurs approximately every 17 ms. Observing this picture, it is also possible to notice that the cavity length at the time of detachment is nearly equal to 0.1L (where L indicates the length of the diverging part of the Venturi nozzle).

	$f^I\ [Hz]$	$f^{II}\ [Hz]$	$T^I\ [ms]$	$T^{II}\ [ms]$	St_d^I	St_d^{II}
P1	59.5	261.9	16.8	3.82	0.075	0.329
P2	59.5	357.1	16.8	2.80	0.075	0.449
P3	59.5	178.6	16.8	5.60	0.075	0.225
P4	297.6	59.5	3.36	16.8	0.374	0.075
Mean	59.5	297.6	16.8	3.36	0.075	0.374

Table 5.4 Shedding frequencies and derivative parameters resulting from the WALE test. f^I denotes the principal peak frequency detected in the corresponding FFT plot, while f^{II} denotes the secondary peak frequency.

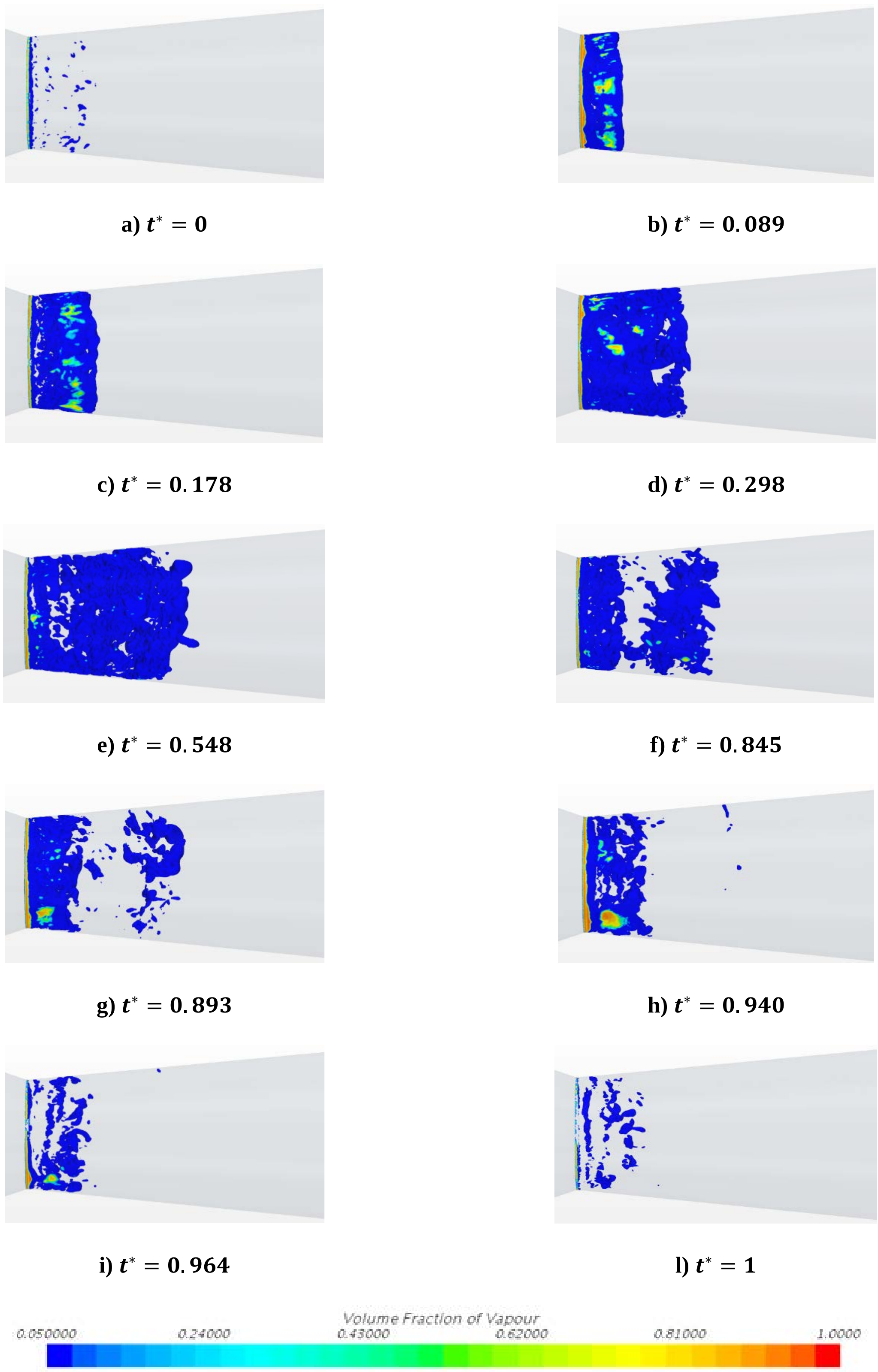
a) $t^* = 0$

b) $t^* = 0.089$

c) $t^* = 0.178$

d) $t^* = 0.298$

e) $t^* = 0.548$

f) $t^* = 0.845$

g) $t^* = 0.893$

h) $t^* = 0.940$

i) $t^* = 0.964$

l) $t^* = 1$

Figure 5.19 Pictures showing the shedding cavitation cycle reproduced by the WALE simulation ($t^* = t/T$, with $T = 16.8\ ms$). In all the figures, the iso-surface for Vapor Fraction = 0.05 is reported. All the views were taken observing the system from the *z*-axis.

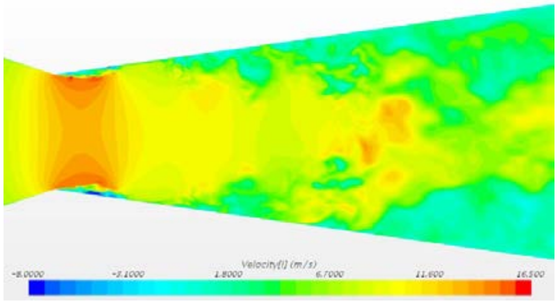

a) Scalar scene reporting the *XY* plane section of the *x*-velocity field for the *WALE* simulation. It is possible to notice the presence of the re-entrant jet. It is also visually confirmed that the average throat velocity is nearly 13 m/s.

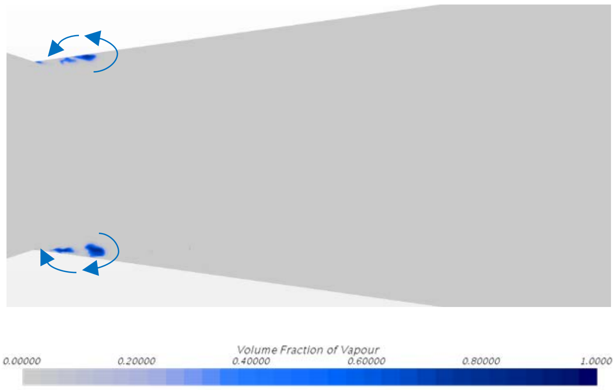

b) Scalar scene reporting the *XY* plane section of the Vapor Fraction field for the *WALE* simulation. The arrows highlight the presence of the re-entrant jet.

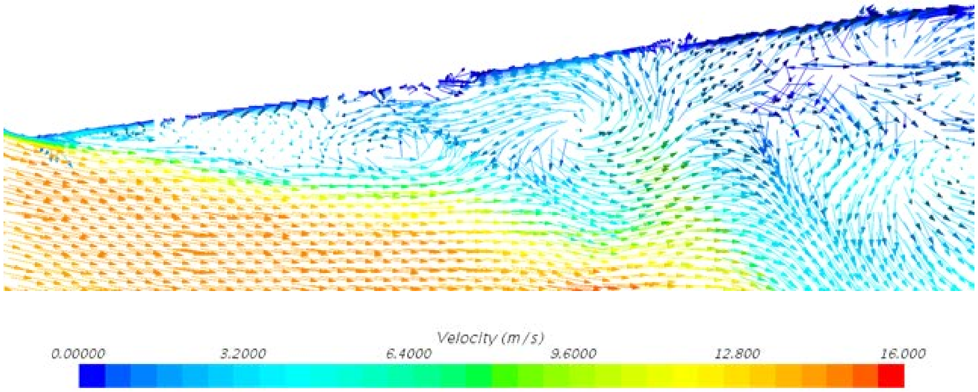

c) Vector scene reporting the *glyph* distribution of the velocity field close to the throat walls for the *WALE* simulation. This view refers to the xy plane section of the Venturi. The magnitude of the re-entrant jet velocity is of the same order of the throat free stream velocity, as reported by Knapp [55].

Figure 5.20 Scalar and vector scenes highlighting the presence of the re-entrant jet during the WALE simulation. All these pictures refer to *XY* plane sections of the Venturi nozzle.

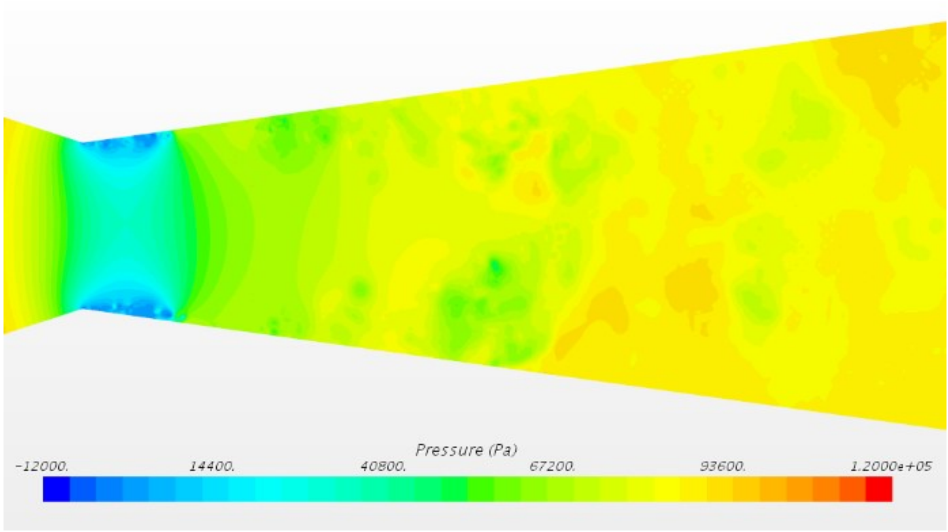

Figure 5.21 Scalar scene of the pressure *XY* plane section from the WALE simulation.

Finally, several pictures of the Velocity and Pressure distributions along the Venturi are presented also for this simulation. In particular, observing Figure 5.20, it is possible, once again, to notice the presence of the re-entrant jet developing close to the Venturi walls from the cavity closure region to the nozzle throat.

Examining the Pressure field depicted in Figure 5.21, also in the WALE case the presence of negative values for the absolute pressure can be observed. The reasons which lead to such negative values for the absolute pressure have been already explained in the previous section.

5.4 Discussion of the Results

Before discussing in detail the numerical results, the Author suggests the reader to take a look to Table 5.5, which summarizes the results obtained from both simulation tests. It must be again underlined that such results were obtained applying the Schnerr-Sauer cavitation model, with *seed density* and *seed diameter* respectively set equal to 10^{11} m^{-3} and 5 μm. No corrections (such as Reboud correction) were used to modify the turbulent viscosity. All the simulations were conducted considering $\sigma = 1$ and $p_{out} = 90\ kPa$ as boundary conditions.

As observed inside the previous two sections, both models were able to effectively capture the physics of the problem: in fact, examining several scalar and vector scene of the velocity field it was possible to detect the presence of the re-entrant jet mechanism, which is responsible for the cloud cavitation shedding process.

	f^{I} $[Hz]$	f^{II} $[Hz]$	f_{exp} **[Hz]**	$St_{d,exp}$	**Relative Error (f^{I} – exp.)**	**Relative Error (f^{II} – exp.)**
Dynamic Smagorinsky	62.5	200	298.2	0.375	79%	32.9%
WALE	59.5	297.6	298.2	0.375	80%	0.20%

Table 5.5 Results obtained from the two simulation tests. The reported results are relative to the average signal (computed as the average of the four probe point signals).

Furthermore, both Dynamic Smagorinsky and WALE SGS models were found to be able to effectively reproduce the periodic behaviour of such phenomenon: in fact, the signals detected by the four probe points set close to the throat walls of the Venturi nozzle clearly show that the cloud cavitation shedding cycle repeats equal to itself at a distance of a characteristic period.

To identify at which frequency the partial cavitation cycle occurs, a spectral analysis was conducted, examining the Vapor Fraction temporal signal detected by the probe points through the use of the FFT technique. All the FFT plots displayed several clear frequency peaks, showing that both models are able to reproduce the periodic shedding cycle and detect a principal frequency at which it occurs.

Both Dynamic Smagorinsky and WALE SGS models detected a peak frequency way lower than the experimental frequency provided by Hogendoorn [22] and Jahangir et al. [46] for the same set of boundary conditions. The relative error, computed as follows:

$$e = \frac{|f_{exp} - f_{sim}|}{f_{exp}} \tag{5.1}$$

Is approximately equal to 80% for both the models. Without further investigations, this fact would inevitably bring to discard both models, as one could say that both are not able to reproduce the shedding process with its proper characteristic frequency. However, it is also important to consider the way in which the peak frequency values were obtained, i.e. using FFT technique to conduct the spectral analysis.

In general, FFTs require lots of data to work efficiently and return accurate results. In this case, due to the high computational costs that both simulations required, it was not possible to store large amounts of data, so it is possible that the FFTs quality is not as high as wished.

This means that results coming from FFT operations are not always fully reliable. So, there is the need to contemporarily examine the signal plot and its relative FFT plot together to understand if the results returned by the FFT are acceptable or not.

From the vision of the temporal signal plots obtained from both simulations, it clearly results that the system pulses also at another frequency, higher than the peak frequency detected considering the FFT results alone and with lower amplitude.

These frequencies are more compatible with the experimental data, bringing to relative errors of 32.9% for the Dynamic Smagorinsky simulation and 0.20% for the WALE simulation. Such frequencies were also detected inside the FFT plots as plot regions presenting high concentration of secondary frequency peaks. This means that both models are effectively able to detect frequencies of the order of the experimental results.

In particular, the WALE model seems to be more capable of reproducing the right frequency at which the partial cavitation phenomena occurs for the chosen set of boundary conditions, returning a very low relative error.

The fact that both simulations were not able to immediately detect peak frequencies of the order of the experimental results is probably due to the mesh: indeed, it is possible that the near walls grid was not so fine as needed to effectively capture the correct temporal behaviour of the re-entrant jet mechanism.

In fact, from the vision of the probe point temporal signals, it seems that the re-entrant jet effectively fluctuates towards the Venturi neck at a high frequency, but it struggles to reach the throat and to cause cavity detachment, succeeding into it only after a longer time lapse. This would explain the detection, through the use of FFT techniques, of low shedding frequencies. Perhaps, further grid refinements would bring to higher pressure differences between the cavity closure region and the Venturi neck, giving the re-entrant jet the boost to reach the throat and complete the cavitation cycle in less time and so, with higher frequencies. Further investigations should be conducted additionally refining the mesh near the walls of the Venturi diverging nozzle to verify if, with a finer mesh, the problem vanishes.

Again, examining the probe point signal plots obtained from the two simulations, it was also possible to observe that the flow was not perfectly axisymmetric. In fact, the signals monitored by the four different probe points were found to be slightly different and not overlapping each other.

It must also be underlined that, analysing the results of the two simulation tests, the choice of the turbulence model (in particular, of the Sub-Grid Scaling model) remains of crucial importance when a simulation concerning cavitation problems is to be faced.

As previously said, the WALE SGS model results to be more accurate than the Dynamic Smagorinsky one and this is probably due to the fact that the WALE SGS model is generally more suitable in reproducing near wall flows than Dynamic Smagorinsky model. Since the re-entrant jet mechanism develops right close to the Venturi walls, such computational behaviour was expected from the beginning of this analysis.

In general, the approach proposed in this Master Thesis project to define both the boundary conditions and the initialization strategy seems to work in the right direction, bringing to results that are in agreement with the experimental data. This approach will be declared fully validated only once the mesh independence conditions will be reached. In any case, this study provides solid bases from which to take advantage of for the future set-up of simulations involving cavitation phenomena and the application of LES techniques to reproduce the turbulence effects.

A few words should also be said concerning the application of the Schnerr-Sauer cavitation model: in both the simulation tests showed to be effective in reproducing the cavitation dynamics, though it does not take into account the effects of the viscosity and of the surface tension on the bubble dynamics. This confirms once again that, in most cases of interest, these two contributions could be considered negligible

Finally, due to the high computational costs required by the two simulations, it was not possible to conduct further studies to investigate the influence of seed density and seed diameter parameters on the test results. The current study could also establish a good base from which to start for such an investigation. It is also possible that these parameters influence the cavity length at time of detachment. However, the results obtained in this project concerning the cavity length at time of detachment were found to be in agreement with the experimental ones.

Chapter 6

Conclusion and Future Prospects

The study of this Master Thesis aimed to validate and, thus, provide a solid approach for the numerical simulation of the partial cavitation dynamics when LES techniques are applied to reproduce the effects of the turbulence phenomena.

Using the commercial software *STAR CCM+*, the two-phase (water – water vapor) cavitating flow was simulated considering both fluids as incompressible and using the *Volume of Fluid* (VOF) as multi-phase model since a clear surface separation between water and water vapor was expected. To account for the interaction between the two phases and for the cavity dynamics, the Schnerr-Sauer cavitation model was selected, assuming both viscosity and surface tension effects on bubble dynamics to be negligible.

Finally, it was decided to use the LES approach to reproduce the turbulence phenomena, and, in particular, two different Sub-Grid Scaling models were tested: the Dynamic Smagorinsky and the WALE SGS models.

The validation tests were conducted considering the same 3-D Venturi geometry used by Hogendoorn [22] and Jahangir et al. [46] in their experiments concerning partial cavitation phenomena in axisymmetric converging-diverging nozzles. From the same references were also extracted the experimental data on which the validation based.

Particular attention was initially given to the definition of the Venturi inflow conditions, which are known to really affect the final solution when turbulence is modelled through LES techniques.

To reproduce realistic turbulent inflow conditions to be applied to the inlet section of the Venturi duct, a new approach was proposed: knowing that the flow entering the nozzle was turbulent fully developed, the same incoming flow was simulated only considering a shorter pipe with periodic interfaces and several statistics concerning the average velocity profile and the average turbulence profile were collected at the outlet interface.

This method allowed to simply reproduce the average properties of the Venturi incoming flow and were set as parameters for the definition of the inlet velocity and turbulence conditions. Furthermore, to account for the random behaviour of turbulence at the inlet section, the Synthetic Eddy Method was applied to both the simulation tests.

After having solved the inflow conditions problem, the focus was shifted on the initialization strategy, which establishes another point of crucial importance for the success of Large Eddy Simulations. Both Dynamic Smagorinsky and WALE SGS models were tested applying the same initialization strategy, formed by four different steps which included several subsequent mesh refinements and time-step reductions. The adoption, in the first part of the simulation, of larger time-steps and of a coarser grid made it possible to reduce the computational costs of both the simulations, also reducing the time needed to obtain the final results.

Despite these assumptions, once the simulations started to run, it took a very long time to achieve results and this confirms that Large Eddy Simulations are still very expensive simulations to deal with, especially when the characteristic Reynolds number is really high and the flow results to be turbulent.

The vapor fraction temporal signal detected by four probe points located close to the Venturi throat walls has been monitored and then analysed to identify the shedding frequency of the partial cavitation process. Both tests showed to be able to simulate the correct physics of the problem: in fact, from the observation of the velocity field, it was possible to detect the presence of the re-entrant jet mechanism, while examining the point probe Vapor Fraction time evolution plots a clear periodic behaviour resulted for the cavitation process.

Once verified that the cavitation process was periodic, a spectral analysis was conducted with the aim of defining the characteristic frequency at which the cloud cavitation cycle occurs. So, the FFTs of the Vapor Fraction temporal signals have been computed and analysed, first identifying as the system characteristic frequencies the peak frequencies returned by the FFT plots.

Only accounting for the FFTs results, both models resulted to be unsuitable for cavitation modelling because they both detected peak frequencies that were way lower than the experimental data. However, in these cases, it is generally not recommended to put full confidence in FFT results as they may not be completely reliable. In fact, it is well known that FFTs need lots of data to work efficiently and return accurate results.

Hence, the FFT results have been analysed contemporarily examining also the corresponding Vapor Fraction time evolution plots to eventually identify further characteristic frequencies at which the system pulses. These further investigations clearly showed that, for both Dynamic Smagorinsky and WALE simulations, the cavitating system also pulses at higher frequencies, which are more compatible with the experimental results provided by Hogendoorn [22] and Jahangir et a [46]. So, it is also possible to say that both models are effectively able to detect frequencies of the order of the experimental ones.

These higher frequencies were found to be visible also inside all the FFT plots as regions of the FFT plot where the concentration of secondary frequency peaks was higher. This fact means that both models are able to effectively reproduce the partial cavitation phenomenon detecting shedding frequency of the order of the experimental data. Basically, the results were found to be really good, but the FFT tools used to elaborate them were not as reliable as desired because the appropriate amount of data was not collected.

In particular, the WALE simulation also detected a shedding frequency very close to the experimental one, returning a relative error equal to 0.2%, while the Dynamic Smagorinsky simulation returned a relative error equal to approximately 33%. This fact also highlights once again the importance of the choice of the turbulence model when numerical problem involving cavitation must be faced.

The higher accuracy of the WALE model with respect to the Dynamic Smagorinsky model is due to the fact that the first SGS model is more suitable for simulating near walls flows. Since the re-entrant jet exactly develops close to the walls of the diverging nozzle, this computational behaviour was expected from the start of the current analysis.

Hence, the numerical approach proposed inside this Master Thesis project gives solid bases for the implementation of simulations involving cavitation, focusing on providing several useful guidelines concerning Large Eddy Simulations techniques and the correct set-up of inflow conditions and initialization strategies on which rely on when such turbulence model is applied.

The fact that both models were not immediately able to detect (inside the respective FFT plots) peak frequencies of the order of the experimental results is probably due to the mesh: in fact, it seems that the re-entrant jet effectively fluctuates towards the throat at higher frequencies, but it struggles in reaching the Venturi neck and consequently causing cavity detachment. Hence, the cavitation cycle is well reproduced, but it takes a longer time to be completed. Further mesh refinement close to the Venturi walls and at the nozzle throat are expected to produce larger pressure differences between the cavity closure region and the Venturi neck, giving to the re-entrant jet the right boost to reach the throat and cause cavity detachment within a shorter time and, so, with higher frequencies.

The huge computational time required to achieve such results did not make possible to run other simulations with further mesh refinements. Therefore, further investigations should be conducted in future, refining the mesh until mesh independence conditions will not be reached.

Once these conditions have been reached, it would be of huge importance to analyse the results obtained for other boundary conditions and compare them to the experimental results provided by Hogendoorn [22] and Jahangir et al. [46].

It would be also interesting, in future, to study the influence of the seed diameter and seed density, which are the cavitation model parameters. Running simulations setting different values for these two parameters could be useful to definitely tune-up the model in order to have results in complete agreement with the other experimental data.

The application of the current approach for simulating cavitating flows of engineering interest will be also possible and could help in obtaining information about phenomena that are difficult to test experimentally.

Bibliography

[1] M. Dular, R. Bachert, B. Stoffel, B. Širok. Experimental evaluation of numerical simulation of cavitating flow around hydrofoil. *European Journal of Mechanics B/Fluids*, 24 (2005) 522538.

[2] Y. Wei, C. Tseng, G. Wang. Turbulence and cavitation models for time-dependent turbulent cavitating flows. *Acta Mech. Sin.*, 27(4):473–487, 2011.

[3] C. Hu, G. Chen, L. Yang, G. Wang. Large Eddy Simulation of Turbulent Attached Cavitating Flows around Different Twisted Hydrofoils. *Energies 2018*, 11, 2768.

[4] P. Sagaut, *Large Eddy Simulation for Incompressible Flows*. Springer, 2001.

[5] V. John, *Large Eddy Simulation of Turbulent Incompressible Flows*. Springer, 2004.

[6] S. B. Pope. *Turbulent Flows*. Cambridge University Press, 2000.

[7] G. R. Tabor, M. H. Baba-Ahmadi, Inlet conditions for Large Eddy Simulation: A review, *Computers & Fluids*, 39:553–567, 2010.

[8] M. Gavaises, F. Villa, P. Koukouvinis, M. Marengo, J-P. Franc. Visualisation and LES simulation of cavitation cloud formation and collapse in an axisymmetric geometry. *International Journal of Multiphase Flow*, 68, pp. 14-26, 2015.

[9] F. Örley, T. Trummler, S. Hickel, M. S. Mihatsch, S. J. Schmidt, N. A. Adams. Large-Eddy Simulation of cavitating nozzle flow and primary jet break-up. *Physics of Fluids*, 27, 086101, 2015.

[10] C. E. Brennen. *Cavitation and Bubble Dynamics*. Oxford University Press, 1995.

[11] J-P. Franc, J-M. Michel. *Fundamentals of Cavitatio*n, Kluwer Academic Publishers. 2004.

[12] F. H. Andersen. Numerical simulation of flow in fuel nozzles for two stroke diesel engines. 2011.

[13] L. Zambon. Numerical simulation of the in-nozzle flow during the opening and closing of the fuel valve for two-stroke diesel engines. 2019.

[14] P. Gorkh, S. J. Schmidt, N. A. Adams. Numerical investigation of cavitation-regimes in a converging-diverging nozzle. *Proceedings of the 10th International Symposium on Cavitation*, 2018.

[15] B. Cointe. CFD Analysis of Cavitation Dynamics in a Converging-Diverging Nozzle. 2018.

[16] P. K. Koukouvinis, M. Gavaises, H. Naseri. Performance of turbulence and cavitation models in prediction of incipient and developed cavitation. *International Journal of Engine Research 18(4)*, 2016.

[17] N. Dittakavi, A. Chunekar, S. Frankel. Large Eddy Simulation of Turbulent-Cavitation Interactions in a Venturi Nozzle. *Journal of Fluids Engineering 132(12)*, 2010.

[18] O. Coutier-Delgosha, J. L. Reboud, Y. Delannoy. Numerical simulation of the unsteady behaviour of cavitating flows. *International Journal for Numerical Methods in Fluids*, 42:527–548, 2003.

[19] O. Coutier-Delgosha, R. Fortes-Patella, J. L. Reboud. Evaluation of the Turbulence Model Influence on the Numerical Simulations of Unsteady Cavitation. *Journal of Fluids Engineering 125(1)*, 2001.

[20] O. Coutier-Delgosha, R. Fortes-Patella, J. L. Reboud. Simulation of unsteady cavitation with a two-equation turbulence model including compressibility effects. *Journal of Turbulence 3(3)*, 2002.

[21] J-L. Reboud, B. Stutz, O. Coutier. Two-phase flow structure of cavitation: experiment and modelling of unsteady effects. *Third International Symposium on Cavitation*, 1998.

[22] W. Hogendoorn, Experimental investigation of cavitation regimes in a converging-diverging nozzle. 2017.

[23] M. Callenaere, J-P. Franc, J-M. Michel, M. Riondet. The cavitation instability induced by the development of a re-entrant jet. *J. Fluid Mech.* (2001), vol. 444, pp. 223:256.

[24] P. Rudolf, M. Hudec, M. Griger, D. Štefan. Characterization of the cavitating flow in converging-diverging nozzle based on experimental investigations. *EPJ Web of Conferences*, 67, 02101, 2014.

[25] B. Stutz, J. L. Reboud. Experiments on unsteady cavitation. *Experiments in Fluids*. 22 (1997) 191:198.

[26] B. Charrière, J. Decaix, E. Goncalvès. A comparative study of cavitation models in a Venturi flow. *European Journal of Mechanics B/Fluids 49* (2015) 287–297.

[27] B. Charrière, E. Goncalves. Numerical investigation of periodic cavitation shedding in a Venturi. *International Journal of Heat and Fluid Flow 64* (2017) 41–54.

[28] Siemens, *Simcenter STAR-CCM+ Documentation*. Siemens PLM Software, 2018.

[29] K.Kundu, I.M.Cohen, D.Dowling. *Fluid Mechanics*. Elsevier, 2012.

[30] Y. Cengel, J. Cimbala. *Fluid Mechanics: Fundamentals and Applications*, Mc Graw Hill Education, 2018.

[31] J. H. Ferziger, M. Perić. *Computational Methods for Fluid Dynamics.* Springer, 2002.

[32] F. Moukalled, L. Mangani, M. Darwish. The Finite Volume Method in Computational Fluid Dynamics. Springer, 2016.

[33] L. Y. Wang, B. Ji, H. Y. Cheng, et al. One-dimensional/three-dimensional analysis of transient cavitating flow in a venturi tube with special emphasis on cavitation excited pressure fluctuation prediction. *Science China Technological Sciences*, volume 63, pp. 223–233, 2020.

[34] G. H. Schnerr, J. Sauer. Physical and Numerical Modeling of Unsteady Cavitation Dynamics. *4th International Conference on Multiphase Flow*, 2001.

[35] C. Stanley, T. Barber, G. Rosengarten. Re-entrant jet mechanism for periodic cavitation shedding in a cylindrical orifice. *International Journal of Heat and Fluid Flow 50* (2014) 169–176.

[36] P. Druault, S. Lardeau, J.-P. Bonnet, F. Coiffet, J. Delville, E. Lamballais, J. F. Largeau, L. Perret. Generation of Three-Dimensional Turbulent Inlet Conditions for Large-Eddy Simulation. *AIAA JOURNAL Vol. 42*, No. 3, 2004.

[37] J. X. Zhang. Analysis on the effect of Venturi tube structural parameters on fluid flow. *AIP ADVANCES 7*, 065315, 2017.

[38] W. Yuan, J. Sauer, G. H. Schnerr. Modeling and computation of unsteady cavitation flows in injection nozzles. *Mec. Ind.* (2001) *2*, 383–394.

[39] O. Lord Rayleigh VIII. On the Pressure Developed in a Liquid during the Collapse of a spherical cavity. *The London, Edinburgh and Dublin Philosophical Magazine and Journal of Science*, 34(200):94–98, 1917.

[40] M. S. Plesset. The dynamics of cavitation bubbles. *Journal of Applied Mechanics*, 16:277–282, 1949.

[41] S. Patankar, D. Spalding. A Calculation Procedure for Heat, Mass and Momentum Transfer in Three-Dimensional Parabolic Flows. *International Journal of Heat and Mass Transfer*, 15:1787–1806, 1972.

[42] E. Giannadakis. *Modeling of cavitation in Automotive Fuel Injector Nozzles*. PhD Thesis, Imperial College London. Department of Mechanical Engineering. University of London, 2005.

[43] J. Smagorinsky. General Circulation Experiments with the Primitive Equations. Part I - The Basic Experiment. *Monthly Weather Review*, Vol. 91, No. 3, 1963, pp. 99-164.

[44] M. Germano, U. Piomelli, P. Moin, W. H. Cabot, A Dynamic Subgrid-Scale Eddy Viscosity Model, *Physics of Fluids A*, 3(7), pp. 1760-1765, 1991.

[45] F. Nicoud, F. Ducros. Subgrid-Scale Stress Modelling Based on the Square of the Velocity Gradient Tensor. *Flow, Turbulence and Combustion, 62*, pages 183–200 (1999).

[46] S. Jahangir, W. Hogendoorn, C. Poelma. Dynamics of partial cavitation in an axisymmetric converging-diverging nozzle. *International Journal of Multiphase Flow 106*, (2018), 34–45.

[47] J. Hult, P. Simmank, S. Matlok, S. Mayer, Z. Falgout, M. Linne. Interior flow and near-nozzle spray development in a marine-engine diesel fuel injector. *Exp. Fluids 57*, 2016.

[48] P. P. Gohil, R. P. Saini. Numerical Study of Cavitation in Francis Turbine of a Small Hydro Power Plant. *Journal of Applied Fluid Mechanics*, Vol. 9, No. 1, pp. 357-365, 2016.

[49] J. Bosschers. Propeller Tip-Vortex Cavitation and its Broadband Noise. 2018.

[50] J-P. Franc, J-M. Michel. Attached cavitation and the boundary layer: experimental investigation and numerical treatment. *Journal of Fluid Mechanics*, 154:63–90, 1985.

[51] P. Tomov, K. Croci, S. Khelladi, F. Ravelet, A. Danlos, F. Bakir, C. Sarraf. Experimental and numerical investigation of two physical mechanisms influencing the cloud cavitation shedding dynamics. In *HAL Id: hal-01284006*, 2016.

[52] R. T. Knapp. Recent investigation of the mechanics of cavitation and cavitation damage. *ASME*, 1955.

[53] H. Ganesh, S. A. Mäkiharju, S. L. Ceccio. Bubbly shock propagation as a mechanism for sheet-to-cloud transition of partial cavities. *J. Fluid Mech.* (2016), *vol. 802*, pp. 37-78, 2016.

[54] R. R. Prasad and K. R. Sreenivasan, Measurement and interpretation of fractal dimension of the scalar interface in turbulent flows, *Phys. Fluids A*, 2:792–807, 1990.

[55] ANSYS. *ANSYS Fluent User's Guide, Release 19.0.* 2018.

Appendix

7.1.1 Field Functions in *STAR CCM+*

Average Velocity Variance Profile

```
u' = sqrt(1/3*(${Velocity[i]VarianceMonitor}+${Velocity[j]VarianceMonitor}+
+${Velocity[k]VarianceMonitor}))
```

Average Velocity Profile

```
U = sqrt(pow(${MeanVelocity[i]Monitor},2)+pow(${MeanVelocity[j]Monitor},2)+
+pow(${MeanVelocity[k]Monitor},2))
```

Turbulence Intensity

```
${u'}/${U}
```

Time Scale

```
3.5/${MeanStrainRateTensorModulusMonitor}
```

Turbulent Length Scale

```
${TimeScale}*sqrt(3.5*${MeanTurbulentViscosityMonitor}/${Density}*
*${MeanStrainRateTensorModulusMonitor})
```

Activation of the Schnerr-Sauer source term

```
Cavitation = (Time<StartCavitation)?0:1
```

Physical time value of activation of the Schnerr-Sauer cavitation model

```
StartCavitation = 2
```

Vector Field function for the interpolation of Average Velocity Profile table data at the duct inlet

```
interpolatePositionTable(@Table("Mean Velocity Profile"),
"Mean of Velocity[i]", "Mean of Velocity[j]", "Mean of Velocity[k]")
```

Scalar Field function for the interpolation of Turbulent Length Scale table data at the duct inlet

```
interpolatePositionTable(@Table("Turbulent Length Scale"),
"Turbulent Length Scale")
```

Scalar Field function for the interpolation of Turbulence Intensity table data at the duct inlet

```
interpolatePositionTable(@Table("Turbulence Intensity"),
                    "Turbulence Intensity")
```

Scalar Field function for the interpolation of Pressure table data for the duct flow initialization

```
interpolatePositionTable(@Table("Pressure Initialization"), "Pressure")
```

Vector Field function for the interpolation of Velocity table data for the duct flow initialization

```
interpolatePositionTable(@Table("Velocity Initialization"),
       "Velocity[i]", "Velocity[j]", "Velocity[k]")
```